ABSTRACT

**EFFECTS OF OPERATING AND GEOMETRIC VARIABLES ON
HYDRODYNAMICS AND TABLET DISSOLUTION IN STANDARD AND
MODIFIED DISSOLUTION TESTING APPARATUSES 2**

**by
Yimin Wang**

Dissolution testing is routinely conducted in the pharmaceutical industry to provide critical *in vitro* drug release information for quality control purposes, and especially to assess batch-to-batch consistency of solid oral dosage forms such as tablets. Among the different types of apparatuses listed in the United States Pharmacopoeia (USP), the most commonly used dissolution system for solid dosage forms is the USP Dissolution Testing Apparatus 2, consisting of an unbaffled, hemispherical-bottomed vessel equipped with a 2-blade radial impeller.

Despite its extensive use in industry and a large body of work, some key aspects of the hydrodynamics of Apparatus 2 have received very little attention, such as the determination of its power dissipation requirements (which controls solid-liquid mass transfer processes) and the velocity distribution under the different agitation conditions at which this system is routinely operated. In addition, the tablet dissolution performance of Apparatus 2 has been shown to be highly sensitive to a number of small geometric factors, such as the exact locations of the impeller and the dissolving tablet.

Therefore, in this study, computation and experimental work was conducted to (a) quantify the roles of some key hydrodynamic variables of importance for the standard Apparatus 2 system and determine their impact on the dissolution profiles of solid dosage forms, and (b) design and test a modified Apparatus 2 that can overcome the major

limitations of the standard system, and especially those related to the sensitivity of the current apparatus to tablet location.

Accordingly, the hydrodynamics in the standard USP Apparatus 2 vessel was experimentally quantified using Laser-Doppler Velocimetry (LDV) and Particle Image Velocimetry (PIV). Complete experimental mapping of the velocity distribution inside the standard Apparatus 2 was obtained at three agitation intensities, i.e., 50 rpm (N_{Re}=4939), 75 rpm (N_{Re}=7409) and 100 rpm (N_{Re}=9878). The velocity distributions from both LDV and PIV were typically found to be very similar. It was found that the overall flow pattern throughout the whole vessel was dominated by the tangential component of the velocity at all agitation speeds, whereas the magnitudes of the axial and radial velocity components were typically much smaller. In the bottom zone of the vessel, two regions were observed, i.e., a central, low-velocity inner core region, and an outer recirculation loop below the impeller, rotating around the central inner core region. This core region typically persisted, irrespective of the impeller agitation speed. Computation Fluid Dynamics (CFD) was additionally used to predict velocity profiles. Typically, the CFD predictions matched well the experimental results.

The power dissipated by the impeller in Apparatus 2 was experimentally measured using a frictionless system coupled with torque measurement. CFD was additionally used to predict the power consumption, using two different approaches, one based on the integration of the local value of the energy dissipation rate, and the other based on the prediction of the pressure distribution on the impeller blade, from which the torque and the power required to rotate the impeller were predicted. The agreement between the experimental data and both types of numerical predictions was found to be

quite satisfactory in most cases. The results were expressed in terms of the non-dimensional Power number, *Po*, which was typically found to be on the order of ~0.3. The power number was observed to decrease very gradually with increasing agitation speeds.

The results of this work and of previous work with the standard USP Apparatus 2 confirm that this apparatus is very sensitive to the location of the tablet, which is typically not controlled in a typical test since the tablet is dropped into the vessel at the beginning of the test and it may rest at random locations on the vessel bottom. Therefore, in this work a modified USP Dissolution Testing Apparatus 2, in which the impeller was placed 8-mm off-center in the vessel, was designed and tested. This design eliminates the poorly mixed inner core region below the impeller observed in the standard Apparatus 2 vessel. Dissolution tests were conducted with the Modified Apparatus for different tablet locations using both disintegrating calibrator tablets (Prednisone) and non-disintegrating calibrator tablets (Salicylic Acid). The experimental data clearly showed that all dissolution profiles in the Modified Apparatus were not affected by the tablet location at the bottom of the vessel. This design can effectively eliminate artifacts generated by having the tablet settle randomly at different locations on the vessel bottom after dropping it at the beginning of a dissolution testing experiment.

The hydrodynamic and mixing characteristics of the modified Apparatus 2 were studied in some detail by experimentally measuring and computationally predicting the velocity distribution, power dissipation, and mixing time in the modified system. The velocity profiles near the bottom of the vessel were found to be significantly more uniform than in the standard Apparatus 2, because of the elimination of the poorly mixed

zone below the impeller. The power dissipation in the modified Apparatus 2 was typically higher than in the standard system, as expected for an non-symmetrical system, and the corresponding Power number, *Po*, was less dependent on Reynolds number than *Po* in the standard system. Finally, the mixing time in the modified system, as experimentally measured by using a decolorization method and computationally predicted through CFD simulation, was found to be shorter in the modified Apparatus 2 by 7.7 %-12.9 % as compared to Apparatus 2.

It can be concluded that the modified Apparatus 2 is a more robust testing apparatus, which is capable of producing dissolution profiles that are less sensitive to small geometric factors that play a major role in the standard USP Apparatus 2.

**EFFECTS OF OPERATING AND GEOMETRIC VARIABLES ON
HYDRODYNAMICS AND TABLET DISSOLUTION IN STANDARD AND
MODIFIED DISSOLUTION TESTING APPARATUSES 2**

**by
Yimin Wang**

**A Dissertation
Submitted to the Faculty of
New Jersey Institute of Technology
in Partial Fulfillment of the Requirements for the Degree of
Doctor of Philosophy in Chemical Engineering**

**Otto H. York Department of
Chemical, Biological and Pharmaceutical Engineering**

August 2011

APPROVAL PAGE

EFFECTS OF OPERATING AND GEOMETRIC VARIABLES ON HYDRODYNAMICS AND TABLET DISSOLUTION IN STANDARD AND MODIFIED DISSOLUTION TESTING APPARATUSES 2

Yimin Wang

Dr. Piero M Armenante, Dissertation Advisor	Date
Distinguished Professor of Chemical Engineering, NJIT	

Dr. Norman Loney, Committee Member	Date
Professor, Chair of Chemical Engineering, NJIT	

Dr. Laurent Simon, Committee Member	Date
Associate Professor of Chemical Engineering, NJIT	

Dr. Ecevit A Bilgili, Committee Member	Date
Assistant Professor of Chemical Engineering, NJIT	

Dr. Zongming Gao, Committee Member	Date
Research Chemist, U. S. Food and Drug Administration, Missouri	

Ms. Vivian Gray, Committee Member	Date
President, V. A. Gray Consulting, Inc, Delaware	

BIOGRAPHICAL SKETCH

Author: Yimin Wang

Degree: Doctor of Philosophy

Date: August 2011

Undergraduate and Graduate Education:

- Doctor of Philosophy in Chemical Engineering,
  New Jersey Institute of Technology, Newark, NJ, 2011

- Bachelor of Science in Material Science and Engineering,
  East China University of Science and Technology, Shanghai, China, 2006

Major: Chemical Engineering

Presentations and Publications:

Bai, G., Wang, Y., Armenante. P. M. (2010). Velocity Distribution and Shear Rate Variability Resulting from Changes in the Agitation Speed in the USP Apparatus 2. *International Journal of Pharmaceutics*, 403 (1-2): 1-14.

Wang, Y., Armenante, P. M. (2010). Toward a More Reliable USP Dissolution Testing Apparatus 2. *AICHE Annual Meeting*, Salt Palace Convention Center, Salt Lake City, Utah.

Wang,Y., Armenante, P. M. (2010). Toward a more reliable USP Apparatus 2, *ISPE Student Poster Competition*, Rutgers University, New Jersey.

Wang, Y., Armenante, P. M. (2010). Experimental PIV Determination and Numerical CFD Prediction of Fluid Flow in USP Apparatus 2. *Dana Knox Research Showcase*, NJIT, New Jersey.

Wang, Y., Armenante, P. M. (2009). Velocity Distribution and Shear Rate Variability Resulting From Changes in the Agitation Speed in the USP Dissolution Testing Apparatus 2. *AICHE Annual Meeting*, Nashville, Tennessee.

Wang, Y., Armenante, P. M. (2009). Fluid Flow under Different Agitation Speeds in USP Apparatus 2. *ISPE Student Poster Competition*, NJIT, Newark, New Jersey.

Shen, F., Wang, Y., Yuan X., Guo W., Wu, C. Interfacial Coordination Reaction in CuSO$_4$ Filled SAN Copolymer. *Journal of Macromolecular Science. B: Physics*, 2008, 47, 76.

TABLE OF CONTENTS

TABLE OF CONTENTS
(Continued)

TABLE OF CONTENTS
(Continued)

Chapter   **Page**

LIST OF TABLES

LIST OF TABLES
(Continued)

LIST OF FIGURES

LIST OF FIGURES
(Continued)

LIST OF SYMBOLS

A	Surface area
B	Thickness of impeller blade
C *(Chapter 2)*	Clearance of the bottom
C *(Chapter 3, Chapter 6)*	Concentration
$C_{1\varepsilon}$, $C_{2\varepsilon}$, $C_{3\varepsilon}$, C_μ	Standard k - ε model constants
C^*	Concentration at infinite time
d_p	Particle size
D	Shaft diameter
D_{AB}	Mass diffusivity
$D_{i,m}$	Diffusion coefficient of species i
D_t	Turbulent diffusivity
D_1	Length of top edge of impeller blade
D_2	Length of bottom edge of impeller blade
f_1	Difference factor
f_2	Similarity factor
F	Force
Fr	Froude number
g	Gravitational acceleration
G_b	Generation of turbulence kinetic energy due to buoyancy
G_k	Generation of turbulence kinetic energy due to mean velocity gradients

H (Chapter 2)	Height of vessel
H (Chapter 5, Chapter 6)	Height of liquid
H_l	Height of impeller blade
$\vec{J}_i$	Diffusion flux of species i
k	Turbulent kinetic energy
k_{SL}	Solid-liquid mass transfer coefficient
L	Length
M	Mixing efficiency
n	Number of time point
n_i	Number of impeller
N	Agitation speed
p	Static pressure
P	Power
Po	Impeller Power number
r	Radial distance from center of vessel
Re	Reynolds number
R_i	Net rate of production of species i
R_t	Dissolution value of reference at time t
Sc	Schmidt number
Sh	Sherwood number

S_i	Rate of creation by addition from dispersed phase and any user-defined sources
S_k , S_ε	User-defined source terms
$t_{95\%}$	95% mixing time
T	Vessel diameter
T_t	Dissolution value of test location at time t
u	Velocity
$\overline{U}_{axial}$	Mean velocity of axial component
$\overline{U}_{radial}$	Mean velocity of radial component
$\overline{U}_{\tan gential}$	Mean velocity of tangential component
U'_{axial}	Fluctuation velocity of axial component
U'_{radial}	Fluctuation velocity of radial component
$U'_{\tan gential}$	Fluctuation velocity of tangential component
U_{tip}	Tip velocity of impeller
V	Volume
x	x- coordinate
y	y- coordinate
Y_i	Local mass fraction of species i
Y_M	Contribution of fluctuation dilation in compressible turbulence to the overall dissipation rate

z	Height of iso-surface
ε	Turbulent energy dissipation rate
θ	Non-dimensional mixing time
μ	Dynamic viscosity
μ_t	Turbulent viscosity
v	Kinematic viscosity
ρ	Density
σ_k	Turbulent Prandtl number of k
σ_ε	Turbulent Prandtl number of ε
τ	Torque
ω	Angular velocity

CHAPTER 1

INTRODUCTION

1.1   Background

In the pharmaceutical industry, dissolution testing is a critical step in quality control of manufactured final products and it is one of the standard methods for assessing batch-to-batch consistency of solid oral drug delivery systems, such as tablets and capsules. One of the most widely used dissolution test devices is the United State Pharmacopeia (USP) Apparatus 2 (paddle). Apparatus 2 and the method associated with it are useful in the pharmaceutical and biotechnology industry to formulate solid drug dosage forms and to develop quality control specifications for its manufacturing process.

Drug dissolution can be defined as a process by which the drug substance dissolves into solution. Although dissolution appears to be a simple process, developing a suitable dissolution test for the drug content of solid dosage forms requires careful considerations of operation variables such as the agitation speed, temperature control, dissolution medium, dosage form design and other important variables.

Currently there are seven dissolution testing apparatuses specified by USP [1]. Different types of drug dosage forms have specific dissolution apparatuses and operation conditions for dissolution testing, such as dissolution medium, medium volume, agitation speed, detecting UV wavelength, and others.

USP Apparatus 1, the rotating basket dissolution apparatus was developed in 1960s. This system consists of a 1 L cylindrical, hemispherical bottom, unbaffled vessel and a meshed basket. This device is appropriate for dosage forms such as capsules, beads

and suppositories. The design of the basket can prevent light drugs from floating around during the dissolution tests.

The rotating paddle apparatus, USP Apparatus 2, was developed shortly after Apparatus 1. It consists of a paddle agitator and the same vessel as USP Apparatus 1. This system is helpful for heavier drugs such as tablets, which can rapidly sink when dropped in the dissolution medium. For light drugs, a sinker would be used to help sinking the tablet. USP Apparatus 2 is used for both immediate release and modified release drug delivery systems. In general, three dissolution volumes are used, i.e., 500 mL, 900 mL and 1000 mL. This system is routinely used to test oral dosage tablets and capsules.

In 1995, USP introduced the reciprocating cylinder apparatus as an alternative to the basket and paddle apparatuses for drug release testing. The reciprocating cylinder apparatus has six inner tubes moving vertically. There is a screen at each end, containing the drug delivery system. This apparatus has been successfully used for tablets, capsules and some extended-release dosage. When small testing volumes (200-300 mL) are required, reciprocating cylinder is a good choice.

The flow-through cell was originally developed to simulate gastrointestinal conditions by exposing extended-release and poorly soluble dosage forms to media of varying pH. It was designed for non-disintegrating drugs. This apparatus consists of six cells, which can be of various sizes depending on the drug delivery system. The apparatus has been used for capsules, powders, tablets, implants, and suppositories and has been used with a wide range of media volume.

USP Apparatuses 5 and 6 are employed for testing transdermal patches, and the official vessels are the same as in Apparatuses 1 and 2, i.e., a 1 L unbaffled hemispherical-bottom glass vessel. Apparatuses 5 and 6 were originally introduced as supplements to USP Apparatus 1 and 2. USP Apparatus 5 is also called paddle over disk. This device is simply a modified version of USP Apparatus 2. The vessel and agitator are the same as in USP Apparatus 2. The only difference is there is the presence of horizontal disk whose purpose of the disk is to act as a sinker to hold the transdermal patch during dissolution tests. USP Apparatus 6 is usually referred to as rotating cylinder. The device uses the same vessel of Apparatus 1 where the basket is replaced with a hollow stainless steel cylinder. The transdermal patch is pasted on the cylinder with the drug release side placed outwards.

Apparatus 7, incorporating a reciprocating holder was originally introduced as a small volume option for small transdermal patches. Currently, Apparatus 7 can accommodate a dissolution environment as low as 5 mL.

Drug absorption from a solid dosage form after oral administration depends on the release of the drug substance from the drug product, the dissolution or solubilization of the drug under physiological conditions, and the permeability across the gastrointestinal tract. Because of the critical nature of the first two of these steps, *in vitro* dissolution may be relevant to the prediction of *in vivo* performance. Based on this general consideration, *in vitro* dissolution tests for immediate release solid oral dosage forms, such as tablets and capsules, are used to (1) assess the lot-to-lot quality of a drug product; (2) guide development of new formulations; and (3) ensure continuing product quality

and performance after certain changes, such as changes in formulation, manufacturing process, site of manufacture, and scale-up of the manufacturing process.[2]

Most solid oral dosage forms are required to undergo dissolution testing, and it is not uncommon to have a drug recall due to a failed dissolution test [3]. In an effort to ensure that drug products can be manufactured consistently, pharmaceutical scientists have utilized *in vitro* dissolution testing as a quality control tool for formulation development, manufacturing process assessment and the prediction of a drug's bioequivalence. The batch-to-batch quality of a product is often determined by conducting dissolution tests based on with procedures specified by USP.

The criterion for accepting or failing a batch is often referred to as the 'Q' value. The 'Q' value is the amount of dissolved active ingredient at a specific time point. The acceptance criteria of USP dissolution tests for immediate-release oral dosages are summarized in Table 1.1 [1]. A product can be subjected to a total of three stages of testing depending upon the results in stage 1 and stage 2 during a dissolution test. If a product passes the acceptance criteria at a given stage, there is no need to go to the next stage of testing.

Table 1.1 Acceptance Criteria of USP Dissolution Test Intended for Immediate-release Products

Stage	Number tested	Acceptance criteria
S1	6	Each unit is not less than Q+5%
S2	6	Average of 12 units (S1+S2) is equal to or greater than Q, and no unit is less than Q-15%
S3	12	Average of 24 units (S1+S2+S3) is equal to or greater than Q, not more than 2 units are less than Q-15%, and no unit is less than Q-25%

Source: [1].

The value of dissolution as a quality control tool for predicting *in vivo* performance of a drug product is significantly enhanced if an *in vitro-in vivo* relationship is established. The *in vitro* test serves as a tool to distinguish between acceptable and unacceptable drug products. Acceptable products are bioequivalent, in terms of *in vivo* performance, whereas unacceptable products are not. If the batches show differences in *in vivo* performance, then *in vitro* test conditions can be modified to correspond with the *in vivo* data to achieve an *in vitro-in vivo* correlation. If no difference is found in the *in vivo* performance of the batches and if the *in vitro* performance is different, it may be possible to modify test conditions to achieve the same dissolution performance of the batches studied *in vivo*. Very often, the *in vitro* dissolution test is found to be more sensitive and discriminating than the *in vivo* test. From a quality assurance point of view, a more discriminative dissolution method is preferred, because the test will indicate possible changes in the quality of the product before *in vivo* performance is affected.[2]

Dissolution testing is sensitive to a number of parameters. The challenges generally are divided into two classes, i.e., variability and bio-relevancy [3]. Variability in dissolution testing is an area that has received a great deal of attention. Many studies demonstrated the source and extent of test variability [4, 5, 6, 7]. Even to this day, dissolution testing remains susceptible to significant error and test failures.

A review of the literature shows that there have been numerous reports describing high variability of test results, even for dissolution apparatus calibrator tablets [8, 9, 10]. Even more significantly, the hydrodynamics of USP Apparatus 2 vessel appears to play a major role in the poor reproducibility of dissolution testing data and the inconsistency of dissolution results. This is not surprising considering that Apparatus 2 vessel is a small, unbaffled vessel with a hemispherical bottom provided with a slowly rotating paddle, in which a tablet (or another dosage form) is dropped. As it has been known for decades to reaction engineers, such complex hydrodynamics in such a small vessel would have a direct impact on mass transfer rates and, consequently, on dissolution rates. Furthermore, the tablet dissolution process is intrinsically complex since it involves solid-liquid mass transfer, particle erosion, possible disintegration, particle suspension and particle-liquid interactions. This process is further complicated by the interactions of the complex three-dimensional flow with the dissolving tablet and its fragmented particles, the highly variable velocity, energy and shear stress distribution as a function of tablet location within the vessel, and the uncertainty in the location of the tablet upon its release inside the apparatus. Literature reports confirm these observations and the potentially important role of hydrodynamics on the dissolution process and the inconsistency of dissolution test results [4, 5, 11, 12, 13, 14, 15, 16, 17, 18]. It is believed that the poorly reproducible

and inconsistent data of dissolution data is stemming from the complex hydrodynamics in the Apparatus 2 vessel.

Despite its widely use in pharmaceutical industry, relatively little information was available until recently on the hydrodynamics of Apparatus 2 vessel and the effects of operation conditions and geometric variables on the velocity distribution in the system. Such information is critical to advance the fundamental understanding of the dissolution rate process, enhance the reliability of dissolution testing and eliminate artifacts associated with test methods, especially since dissolution measurements have often been reported to be inconsistent and poorly reproducible. In fact, failed dissolution tests resulted in 47 products recalls in 2000-2002, representing 16% of non-manufacturing recalls for oral solid dosage forms [19, 20, 21]. Failed dissolution tests can result in product recalls, costly investigations, and potential production delays, all of them having substantial financial impact to the pharmaceutical industry. The examples listed in Table 1.2 show some recent drug recalls due to a failed dissolution test. These inconsistencies present even greater challenges when trying to implement Quality by Design, which defines the future state of dissolution, its value, method design, and links to the design space.

Table 1.2 Drugs Recalled from FDA Enforcement Reports

Recalled date	Drug	Manufacturer	Recalled reason
Feb 17, 2010	Demser	Merck & Company, Inc., West Point, PA	Samples have failed to meet dissolution specifications
Jan 15, 2010	Prempro	Wyeth Pharmaceuticals, Philadelphia, PA	Lots do not conform to the dissolution specifications
Nov 18, 2009	Zmax	Pfizer Inc., New York, NY	Failed USP dissolution test requirements

Source: [22].

1.2 Motivation and Objectives of This Work

In previous research work by this research group [4, 5, 17, 18], it was shown that the hydrodynamics plays an important factor in the performance of dissolution testing in Apparatus 2 vessel. The effects of a number of variables on the hydrodynamics were quantified first, and then their impact on dissolution rates was experimentally and computationally determined.

In the present study, further work was conducted on the effect of operating variables on the existing USP Apparatus 2 vessel and the determination of key mixing characteristics of the system. In addition, one of the key objectives of the work described here has been to develop a slightly modified variation of Apparatus 2, capable of improving the performance of the existing system while adding robustness to it as far as dissolution testing reproducibility is concerned. Therefore, in this study, computation and experimental work was conducted to (a) quantify the roles of some key hydrodynamic variables of importance for the standard Apparatus 2 system and

determine their impact on the dissolution profiles of solid dosage forms, and (b) design and test a modified Apparatus 2 that can overcome the major limitations of the standard system, and especially those related to the sensitivity of the current apparatus to tablet location.

The hydrodynamics in the standard USP Apparatus 2 vessel was first experimentally quantified using Laser-Doppler Velocimetry (LDV) and Particle Image Velocimetry (PIV) for different agitation speeds. Computation Fluid Dynamics (CFD) was additionally used to predict velocity profiles.

Secondly, the power dissipated by the impeller in Apparatus 2, a key parameter for the quantification of the mixing performance of the system, was experimentally measured using a frictionless system coupled with torque measurement. CFD was additionally used to predict the power consumption, using two different approaches, one based on the integration of the local value of the energy dissipation rate, and the other based on the prediction of the pressure distribution on the impeller blade, from which the torque and the power required to rotate the impeller were predicted.

Once this work on the standard Apparatus 2 was completed, the attention shifted to possible modifications of the existing apparatus that would retain some of its key features while reducing its shortcomings. It was found that a modified USP Dissolution Testing Apparatus 2 in which the impeller was placed 8-mm off-center in the vessel could be an appropriate approach. Therefore, a prototype modified Apparatus 2 was designed and tested. It was found that this design eliminates the poorly mixed inner core region below the impeller observed in the standard Apparatus 2 vessel. Dissolution tests were conducted with the modified Apparatus 2 for different tablet locations using both

disintegrating calibrator tablets (Prednisone) and non-disintegrating calibrator tablets (Salicylic Acid) tablets. These results indicated that the modified apparatus was much less sensitive to the tablet location than the Standard Apparatus 2. The positive results of this experimentation then prompted a more in-depth analysis and experimental work on the hydrodynamics of the Modified Apparatus 2.

Therefore, the hydrodynamic and mixing characteristics of the modified Apparatus 2 were studied in some detail by experimentally measuring (through LDV) and computationally predicting (through CFD) the velocity distribution in this system. In addition, the power dissipation, and mixing time in the Modified Apparatus 2 were experimentally measured and computationally predicted, and these results were compared with those obtained for the Standard Apparatus 2.

In conclusion, in this work the characteristics of both the standard Apparatus 2 and a modified Apparatus 2 were studied in detail. From this work it can be concluded that the modified Apparatus 2 is a more robust testing apparatus, which is capable of producing dissolution profiles that are less sensitive to small geometric factors that play a major role in the standard USP Apparatus 2.

CHAPTER 2

**EFFECT OF AGITATION SPEED ON THE VELOCITY DISTRIBUTION IN
THE STANDARD USP APPARATUS 2**

2.1   Background

Apparatus 2 has been used in the pharmaceutical industry for decades since it was first officially introduced almost 40 years ago [23].   However, dissolution testing using Apparatus 2 remains susceptible to significant error and test failures. Several reports in the literature have suggested that there is considerable variability, unpredictability and randomness in dissolution profiles using Apparatus 2 [8, 9, 10, 11, 12, 13, 14, 15], even when dissolution apparatus calibrator tablets are used [8, 9, 10, 24, 25]. Earlier studies [25, 26, 27, 28] including publications by Armenante's group [4, 5, 17] have indicated that the complex hydrodynamics that can be observed in Apparatus 2 can contribute to the poor reproducibility and data inconsistencies that can be obtained with Apparatus 2.

Under the typical operation conditions used in this test, the fluid flow in Apparatus 2 vessel is highly heterogeneous. Hence this system can be expected to be associated with a complex hydrodynamics, resulting in fluid velocities whose directions and intensities are highly dependent on the location within the vessel, especially at the bottom of the vessel where the tablet is located during dissolution testing.

A literature review shows that only a limited number of hydrodynamic studies have been conducted on Apparatus 2 over the past 30 years. The first Laser Doppler Anemometry (LDA) measurements of the velocities in Apparatus 2 vessel were reported by Bocanegra et al. [14]. However, the data they obtained were only generated in very limited regions of the vessel. More recently, qualitative flow patterns were obtained using Particle Image Velocimetry (PIV) and Laser-Induced Fluorescence (LIF).   The

flow patterns were compared to the velocity flow field simulated using Computational Fluid Dynamics (CFD) [24]. Other researchers also made efforts to determine the flow field inside Apparatus 2 vessel through CFD [10, 27].

However, the CFD simulations mentioned above were only qualitatively validated against experimental data. McCarthy et al. [26, 28] predicted the flow field with CFD and compared the CFD predictions with the limited experimental results from previous research [14]. In previous work by Armenante's group [17], the velocity field throughout the Apparatus 2 vessel was quantified via Laser Doppler Velocimetry (LDV), and CFD simulations were used to predict the three-dimensional flow in Apparatus 2 vessel in order to validate the simulation predictions against the experimental LDV data. In addition, this validated CFD model was applied to study the mixing time in Apparatus 2 [18]. Further studies have additionally shown that small changes in the geometry of the system can produce large effects on the system hydrodynamic and the dissolution profiles. For example, the velocity flow field and the shear strain rate near the vessel bottom were dramatically impacted by small misalignments of the impeller location [4]. Similarly, the exact location of the tablet during the dissolution process can result in very different dissolution profiles which may result in failure to pass the acceptance criteria established by the USP [5].

The impeller agitation speed is a key variable in *in vitro* dissolution testing with Apparatus 2 vessel since it affects the velocity in the vicinity of the tablets and hence the tablet-liquid mass transfer rate, the rate of drug release, and the dissolution curve. If disintegrating tablets are used, the agitation speed additionally controls whether the tablet fragments accumulate under the impeller ("coning" effect) or become suspended in the

liquid [10, 17, 29, 30]. The impeller agitation speed generally recommended for Apparatus 2 is 50, 75 rpm [2, 31]. However, in the industrial practice, agitation speeds ranging from 50 to100 rpm are commonly used, with 25 rpm and 150 rpm also been employed, although more rarely, depending on the tablet and the drug product being tested [13, 15, 32, 33]. Although there is now quantitative information to understand the hydrodynamics in dissolution vessels stirred at 50 rpm, much more limited information is available on the hydrodynamics of Apparatus 2 when the impeller agitation speed is higher than 50 rpm. Bocanegra et al. [14] applied LDA to measure velocities in Apparatus 2 vessel in selected regions for an agitation speed of 60 rpm, which is a rarely used agitation speed in practice. Kukura et al. [27] simulated the flow field in Apparatus 2 vessel with CFD and predicted the shear strain rate at an agitation speed of 100 rpm, although their modeling results were not compared with experimental results in a quantitative fashion. Moreover, McCarthy et al. [28] studied the hydrodynamics in Apparatus 2 vessel at 25, 100 and 150 rpm with a partially validated CFD model [26]. Hence, there is a need for experimentally quantifying and computationally predicting the hydrodynamics of Apparatus 2 vessel at agitations speed higher than 50 rpm. Therefore, in this portion of the work, LDV and PIV velocity measurements were collected inside the Apparatus 2 vessel at agitation speeds of 50, 75 and 100 rpm.

2.2   Experimental Apparatus and Method

2.2.1 Experimental Apparatus

2.2.1.1 Laser Doppler Velocimetry. A Dantec 55X series Laser Doppler Velocimetry (LDV) apparatus (Dantec Measurement Technology USA, Mahwah, NJ, USA), was used to determine the velocity flow field and turbulence intensity inside the vessel. A schematic of the LDV apparatus is given in Figure 2.1. The LDV system contained a 750 mW argon-ion laser (Ion Laser Technology, Inc.) producing a single multicolored laser beam passing through an optical filter to generate a monochromatic green beam (wavelength: 512 nm). The resulting beam passed through a beam splitter from which two beams emerged, one of which is passed through a Bragg cell to lower the frequency by 40 MHz and distinguish between positive and negative velocity measurements. The beams then passed through a beam expander system and a final focusing lens with a focal length of 330 mm. This lens made the beams converge so that they intersected each other to form a small control volume in the interrogation region where the velocity was to be measured. The scattered light from the seeding particles moving through the control volume was collected by a receiver located inside the probe, and the Doppler shift (directly proportional to the particle velocity) was measured with a photomultiplier assembly. A data acquisition system connected to a computer converted the Doppler shifts into velocity values, and produced on-line measurements of average and fluctuating velocities.
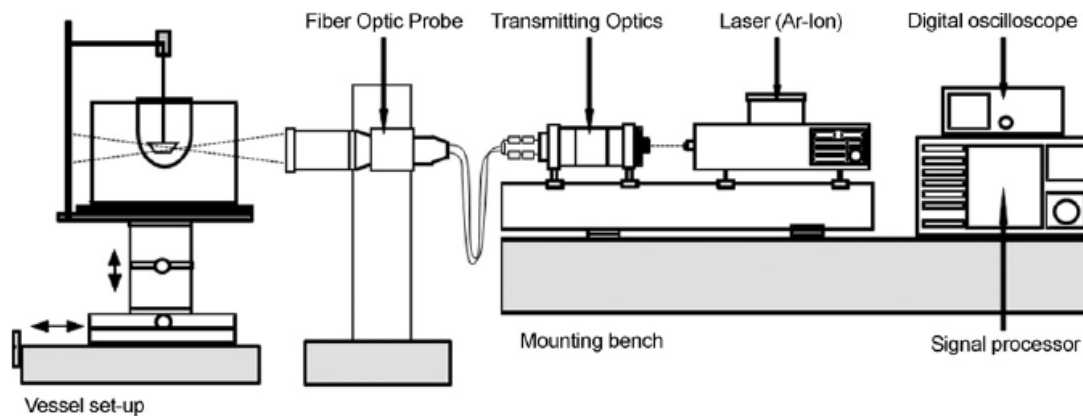
Figure 2.1 Schematic diagram of laboratory LDV experimental set-up.

In an actual measurement, the beams were made to converge inside Apparatus 2 vessel. The water in Apparatus 2 vessel was seeded with neutrally buoyant 10 μm silver coated particles (Dantec Measurement Technology USA, Mahwah, NJ, USA) that could follow the fluid flow pattern very closely. Apparatus 2 vessel was mounted on an *x-y-z* traversing system that could position the vessel at any desired location in front of the LDV probe. The beams were made to converge inside the vessel, thus enabling the fluid velocity to be measured at any desired location in the dissolution vessel. The time interval for each measurement was typically 60 seconds. In most cases, some 600 to 2500 instantaneous velocity data points were collected at any location and for the selected velocity component, from which the local average velocity could be calculated. Appropriate rotation of the fiber optic probe and translation of the dissolution testing system assembly yielded the velocity components in all three directions at any location where a measurement is taken. Triplicate experiments were conducted for each velocity component at each location. The standard deviation was typically 0.001 m/s. In order to fully quantify the fluid flow in the dissolution system, eight horizontal surfaces (iso-surfaces) were selected inside the vessel, as shown in Figure 2.2. The bottom of the

vessel was defined as z=0 mm. Two of the iso-surfaces were located above the impeller (z=75 mm, z=50 mm), three were in the impeller region (z=44 mm, z=35 mm, z=25 mm), and the other three were below the impeller (z=19 mm, z=13 mm, z=7 mm). On each iso-surface, LDV velocity measurements were taken at a number of radial positions, starting at the vessel vertical centerline (or the impeller shaft) and progressing toward the vessel wall. For the iso-surfaces in the impeller region, velocity measurements could only be obtained in the gap between the tip of the passing blade and the vessel wall. Additionally, it was not always possible to take LDV data when the measurement location was too close to the shaft (since the shaft reflected the light and make accurate measurements impossible), or when the curvature of the vessel made it too difficult to collect radial velocities very close to the vessel wall. In such cases, no experimental LDV measurements could be taken.
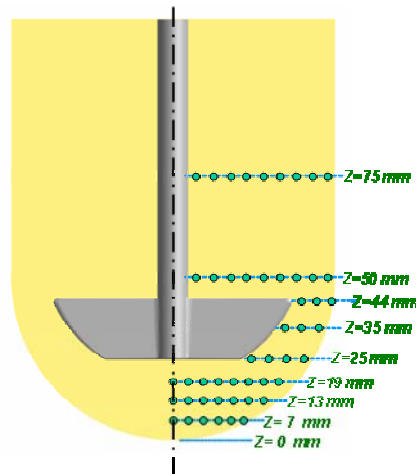
Figure 2.2 Points on eight iso-surfaces during LDV and PIV measurements.

2.2.1.2 Particle Image Velocimetry. [34] A two-dimensional TSI Particle Image Velocimetry (PIV) apparatus (TSI Incorporated, Shoreview, Minnesota, USA) was used to determine the velocity flow field inside Apparatus 2.
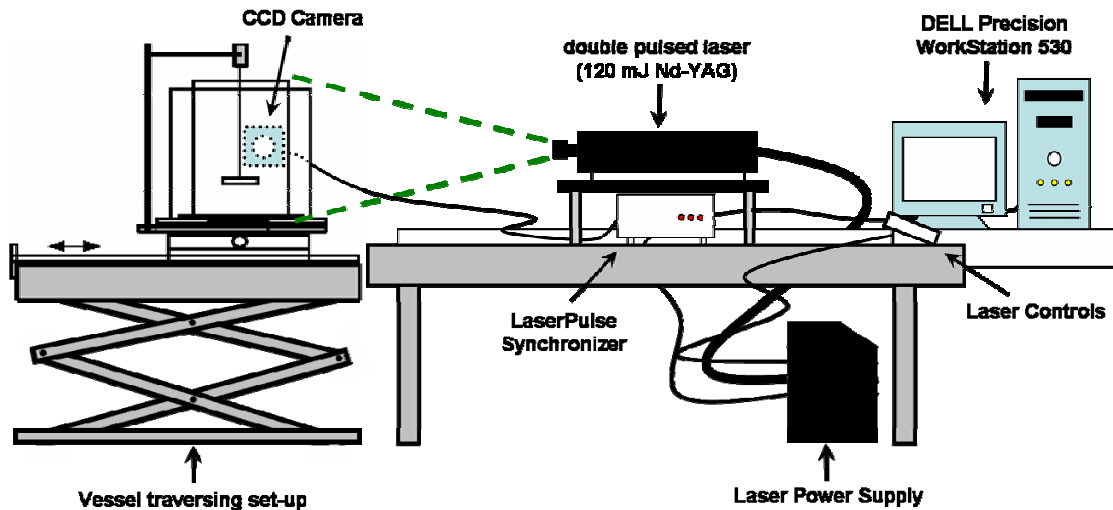
Figure 2.3 Schematic diagram of laboratory PIV experimental set-up.

A schematic of the PIV apparatus is given in Figure 2.3. The PIV system used a double pulsed 120 mJ Nd-Yag laser (New Wave Research model Gemini PIV 15, Fremont, CA, USA) consisting of two infrared laser heads combined in a single package with a second harmonic generator and two discrete power supplies. The laser source came from a Class IV laser, which emitted 532 nm wavelength light. Both laser heads were individually water cooled, and the power supplies contained safety interlocks which were wired to the doors of the laboratory. The laser produced two pulsed infrared laser beams which passed through an optical arrangement of lenses to generate a laser light sheet. This laser light sheet acted as the photographic flash for the single digital camera (PIVCAM 10-30, TSI model 630046). The laser and the digital camera were connected to a synchronizer (LASERPULSE Synchronizer, TSI model 610034), which was then in turn connected to a computer (DELL Precision WorkStation 530). All these components were controlled by software (Insight PIV Software) in the computer. The software collected pairs of digitized images from the CCD camera (with the two images in each

pair being collected at a small but known time interval), which were subdivided into small subsections called interrogation areas. Each pair of frames for a given interrogation areas was then analyzed using cross-correlation to determine the spatial x- and y- displacement that maximized the cross-correlation function for that interrogation area. The resulting displacement vector obtained by dividing the x- and y- displacements by the time interval was taken as the fluid velocity in that interrogation area. In the experiments performed here, silver-coated hollow borosilicate glass spheres (Dantec Measurements Technology USA, Mahwah, NJ, USA) with a density of 1.4 g/cm^3 were added to the water as seed particles. Their sizes ranged from 2 to 20 μm, and their mean particle size was 10 μm. They were used to follow the fluid flow and scatter the laser light used in the PIV fluid velocity measurements.

2.2.2 Experimental Methods

The Apparatus 2 vessel was placed in a square Plexiglas tank filled with water in order to minimize refractive effects at the curved surface of the vessel wall during LDV and PIV measurements. The exact geometries of the impeller and shaft, also measured with a caliper, are illustrated in Figure 2.4 and Table 2.1. The temperature of the water was maintained at 22±0.5 °C. An electric motor connected to an external controller was used to rotate the impeller clockwise at three agitation speeds, i.e., 50 rpm, 75 rpm, and 100 rpm, respectively.

The vessel was mounted on an adjustable table that could be traversed manually in the horizontal and vertical directions, with a position accuracy of 0.1 mm and 0.1 mm, respectively.
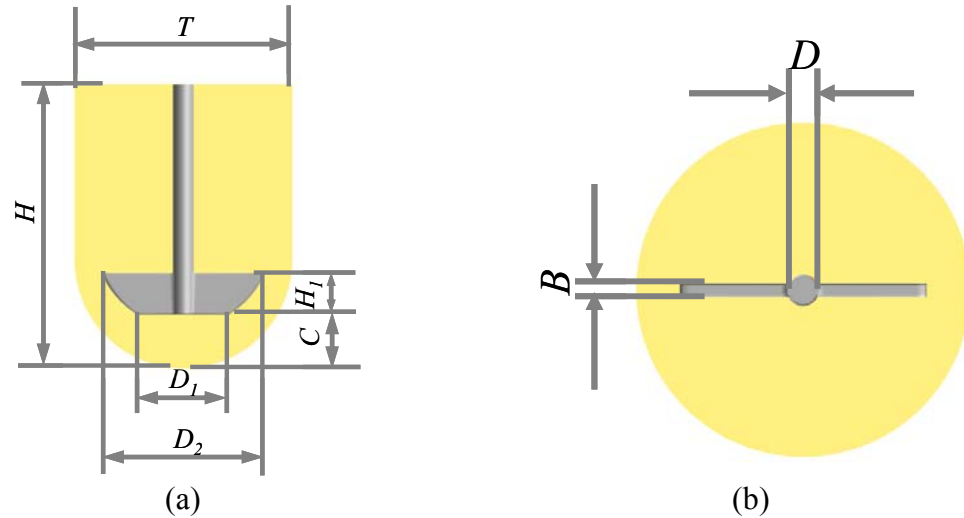
Figure 2.4 Standard Apparatus 2 vessel: (a) front view; (b) bottom view.

The velocities inside the vessel were typically measured at 9 locations on eight different horizontal surfaces (Figure 2.2). Among the eight planes, two were located above the impeller (z=75 mm, z=50 mm), three were in the impeller region (z=44 mm, z=35 mm, z=25 mm), and three were below the impeller bottom (z=19 mm, z=13 mm, z=7 mm).

Table 2.1 Dimensions of Impeller, Shaft and Vessel

Component of Impeller and Shaft	Dimension mm
Height of vessel H	170.00
Vessel diameter T	100.16
Shaft diameter D	9.52
Length of top edge of impeller blade D_1	74.00
Length of bottom edge of impeller blade D_2	42.00
Height of impeller blade H_1	19.00
Clearance of the bottom C	25.00
Thickness of impeller blade B	4.00

In additional experiments, a millimeter scale was taped to the shaft. The change in liquid level near the impeller shaft at different agitation speeds with respect to the same level observed with the impeller at rest was measured by taking photographs at different agitation speeds. The liquid level at the shaft was found to drop by approximately 0.0 mm, 1.0 mm, and 2.3 mm, when compared to the liquid at rest, at agitation speeds equal to 50 rpm, 75 rpm, and 100 rpm, respectively. These level drops correspond to about 0.0%, 1.0%, and 2.3% of the vessel diameter. Furthermore, visual observations showed that this drop was not linear across the surface, but it was primarily concentrated in the neighborhood of the shaft, where the vortex is stronger, implying that most of the liquid surface was nearly perfectly flat for all practical purposes. This observation additionally implies that the assumption made for the boundary conditions used in the numerical simulations in Chapter 4, i.e., that the liquid level is flat at all the agitation speeds tested in this work, is indeed appropriate.

The liquid velocity at any point in the vessel has three components, and the overall flow pattern in the vessel depends on the variations in these three velocity components from point to point. The first velocity component is tangential and acts in a direction tangent to a circular path around the shaft. The second component is axial and acts in a direction parallel with the shaft. The third component is radial and acts in a direction perpendicular to the shaft of the impeller. In the usual case of a vertical shaft, the radial and tangential components are in a horizontal plane, and the axial component is vertical.

For incompressible fluid, turbulent flow the velocity at each point can be assumed to be the sum of the mean velocity at that point and the fluctuating velocity. For any point inside Apparatus 2 vessel, the local velocity could be decomposed into three components, tangential, axial and radial velocities (Equations 2.1, 2.2, 2.3). For each component, the velocity could also be described in terms of the mean velocity and fluctuation velocity in that direction, i.e.:

$$U_{\tan gential} = \overline{U}_{\tan gential} + U'_{\tan gential} \qquad (2.1)$$

$$U_{axial} = \overline{U}_{axial} + U'_{axial} \qquad (2.2)$$

$$U_{rdial} = \overline{U}_{radial} + U'_{radial} \qquad (2.3)$$

in which $\overline{U}_{\tan gential}$, $\overline{U}_{axial}$ and $\overline{U}_{radial}$ are mean velocities in the tangential, axial and radial directions. $U'_{\tan gential}$, U'_{axial} and U'_{radial} are fluctuation velocities in tangential, axial and radial directions.

The mean velocity magnitude can be expressed by Equation 2.4.

$$\overline{U} = (\overline{U}^2_{\tan gential} + \overline{U}^2_{axial} + \overline{U}^2_{radial})^{1/2} \qquad (2.4)$$

Finally, the normalized velocity magnitude was calculated via Equation 2.5, where U_{tip} is the tip speed of impeller. The tip speeds were 0.194, 0.291 and 0.388 m/s for 50, 75 and 100 rpm, respectively.

$$\overline{U}/U_{tip} = (\overline{U}^2_{tan\,gential} + \overline{U}^2_{axial} + \overline{U}^2_{radial})^{1/2}/U_{tip} \qquad (2.5)$$

2.3   Results

Figures 2.5, 2.6 and 2.7 show, respectively, the tangential, axial, and radial fluid velocity profiles on eight horizontal iso-surfaces obtained using LDV measurements at three impeller agitation speeds, i.e., 50rpm, 75rpm and 100rpm, respectively. Figures 2.8, 2.9 and 2.10 show the same measurements in 500 mL water. In these figures, the ordinates represent the normalized fluid velocity (scaled by using the impeller tip speed, U_{tip}) and the abscissas represent the normalized radial position (scaled using the vessel radius, *T/2*). It should be remarked that the scales in these figures are different depending on the velocity direction, since the tangential velocity components are typically one or even two orders of magnitude larger than the axial and radial components.

2.3.1 Velocity Distribution (900 mL)

2.3.1.1 Velocity Profiles above the Impeller.   Figure 2.5 shows that all the tangential velocities above the impeller (iso-surfaces at *z*=75 mm and *z*=50 mm) are in same direction of the impeller rotation (all positive values). The LDV data shows that on both iso-surfaces, and for all agitation speeds, the tangential velocities increase from near zero at the impeller shaft to peak values which are about 40% of impeller tip speed at similar radial positions (0.4<*2r/T*<0.5). The LDV tangential velocity data remain nearly flat in the region 0.5<*2r/T*<0.9. When LDV measurements are taken very close to the vessel wall (*2r/T*=0.98), the tangential velocities drop to below 30% of the impeller tip

speed on the iso-surface at z=75 mm and to about 10% (50 rpm) to 15% (100 rpm) on the

iso-surface at z=50 mm, which is what one would expect since the velocity at the wall

must be zero. In the region for which $2r/T$<0.3, the axial velocities are very small above

the impeller, irrespective of agitation speed (Figure 2.6). On the iso-surfaces at z=75

mm, and z=50 mm the axial velocities are negative (downward flow) for 0.4<$2r/T$<0.7,

while an upward flows occurs when 0.7<$2r/T$<1.0 for all three impeller agitation speeds.

This type of flow is qualitatively similar to that observed with axial impellers in baffled

system, although the intensity of the velocities is very weak here. Finally, Figure 2.7

shows that radial velocities in the region above the impeller are extremely low compared

to the other two velocity components. For example, the highest value of radial velocity

on the iso-surface at z=50 mm is experimentally found to be about 1.2% of the impeller

tip speed and the highest value of the radial velocity on the iso-surface at z=75 mm is

found to be 0.26% of the impeller tip speed irrespective of the impeller agitation speed.

2.3.1.2 Velocity Profiles around the Impeller. Because of the small gap between

the rotating impeller and the vessel wall, only a limited number of LDV velocity

measurements could be collected in this region, i.e., on the iso-surfaces at z=44 mm (top

edge of the impeller), z=35 mm (middle of the impeller) and z=25 mm (bottom edge of

the impeller), as shown in Figure 2.2. Figure 2.5 shows that in the impeller region, the

tangential velocity magnitude for all three impeller agitation speeds follows same pattern,

i.e., higher close to the impeller and lower close to the vessel wall. The LDV

measurements show that the non-dimensional tangential velocity profiles do not change

with increasing impeller agitation speeds except for measurements close to the wall or

next to the impeller. However, even in these cases the changes are small. In Figure 2.6,

the LDV measurements for the iso-surface at $z=44$ mm show that the non-dimensional axial velocity increases rapidly with radial distance, irrespective of impeller speed, thus generating an upwards flow next to the wall. However, even the highest experimental velocity is found to be only 11% of impeller tip speed, i.e., much smaller than the corresponding tangential velocity. On the iso-surface at $z=35$ mm, the non-dimensional axial velocities from LDV measurements are very small (no more than 5.2% of the impeller tip speed) for all three impeller agitation speeds, but now they start being directed downward. However, the near-zero value of these velocity for nearly all *2r/T* values indicates that this iso-surface is very close to the horizontal plane where the horizontal jet generated by the impeller is split upwards and downwards after hitting the vessel wall (stagnation point). Finally on the iso-surface at $z=25$ mm (lower edge of the impeller blade) the LDV measurements turn from minimally positive (for 0.4<*2r/T*<0.7) to appreciably negative (for *2r/T*>0.7) indicating a stronger downwards flow next to the vessel wall. For radial velocities (Figure 2.7), only a limited number of LDV measurements could be collected on the three iso-surfaces in the impeller region. This is primarily caused by the combination of a narrow gap between the edge of the impeller blade and the vessel wall and the curvature of the vessel in this region, which make radial velocity measurements much more difficult to take than for the tangential or axial velocity cases, especially near the wall. The LDV measurements are all found to be close to zero. These measurements are repeated between three and six times to confirm the precision of the measurements, especially since it is expected that the radial component would be higher in the impeller region as opposed to other regions of the vessel.

2.3.1.3 Velocity Profiles below the Impeller. The tangential velocity profiles for

the iso-surfaces below the impeller ($z=19$ mm, $z=13$ mm and $z=7$ mm) presented in Figure 2.5 show that the non-dimensional velocities increase nearly monotonically with radial distance up until nearly the wall (remark: for these iso-surfaces the vessel wall is not found at $2r/T=1$, as in the cylindrical section of the vessel, but at $2r/T<1$ because of the curvature of the hemispherical vessel bottom). All the tangential velocity profiles in this region show a distinct pattern. In the inner core region (for $2r/T<0.2$ for the iso-surfaces at $z=19$ mm and $z=13$ mm and for $2r/T<0.3$ for the iso-surface at $z=7$ mm) the non-dimensional tangential velocity starts at about zero and increases linearly with the radial distance, thus making the fluid move in a solid-body type or rotation, at least in the tangential direction. In the outer region, the non-dimensional velocity still increases to eventually reach a maximum, but not as steeply as in the core region, and some, although small, differences among the curves at different agitation speeds can be noticed. For the profile near the vessel bottom ($z=7$ mm), the core region extends almost up to the wall, making the fluid in this region swirl around the center line, where the velocity is zero or very close to it. The velocity profiles for the same iso-surfaces reported in Figure 2.6 show that the non-dimensional axial velocities are weak and generally positive, i.e., generating an upward flow below the impeller blade, while they become negative, implying a downward flow, only near the wall. It is interesting to notice that in the smaller inner core region, for $2r/T<0.1$, the LDV data indicate that the axial velocity is essentially zero irrespective of agitation speed and z value, and that it becomes slightly stronger only when $2r/T>0.1$. As for the radial velocities below the impeller, on the iso-surface at $z=19$ mm in Figure 2.7, the non-dimensional radial velocities are very close to zero for $2r/T<0.6$, independently of the change in agitation speed. Negative velocity

values near the vessel wall from LDV data indicate that the radial velocity points slightly inward in this region. On the iso-surface at z=13 mm, the axial velocities by LDV measurements show weakly outward velocities for $0.1<2r/T<0.3$. The LDV measurements on this iso-surface show that the non-dimensional radial velocities decrease as the impeller agitation speed increases. On the iso-surface at z=7 mm, peaks in the non-dimensional radial velocities appear at $2r/T$=0.2, based on the LDV measurements. The peak values decrease as the impeller agitation speed increases. It should be remarked that, similar to the axial velocity case, a small inner core region exist for $2r/T$<0.1 where the radial velocity is extremely small irrespective of agitation speed and z value.
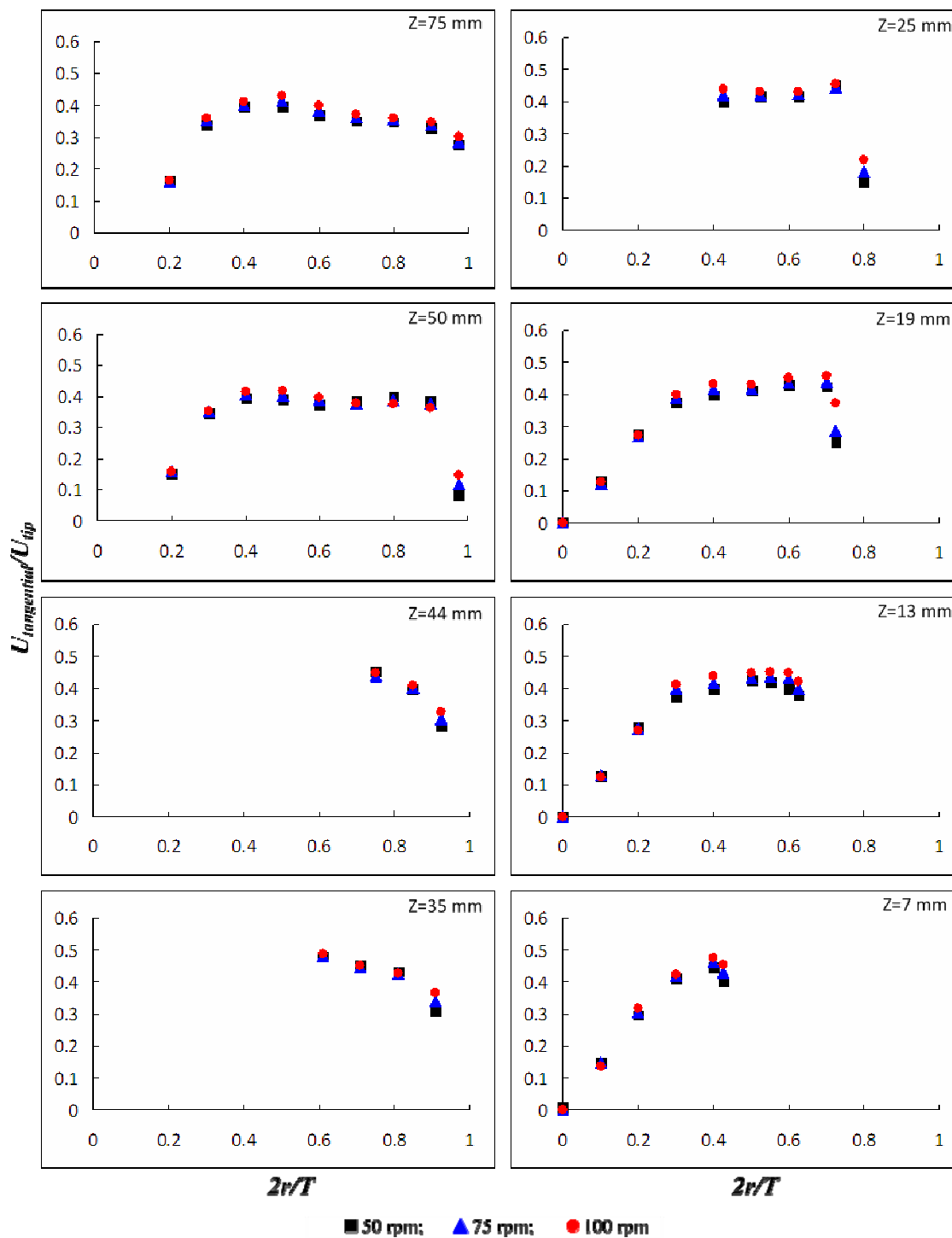
Figure 2.5 LDV measurements for tangential velocities on eight iso-surfaces in standard Apparatus 2 (900 mL water) at agitation speeds of 50, 75 and 100 rpm.
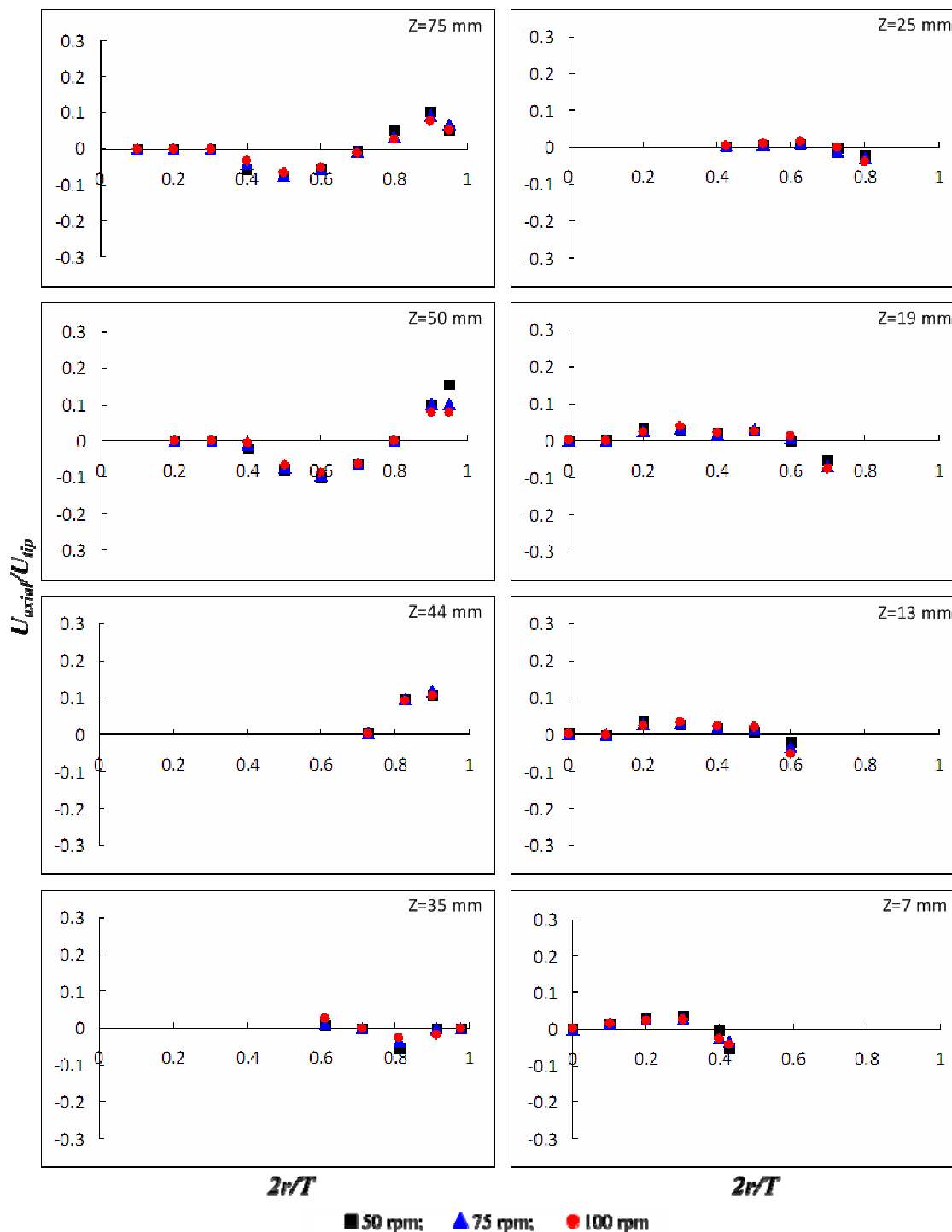
Figure 2.6 LDV measurements for axial velocities on eight iso-surfaces in standard Apparatus 2 (900 mL water) at agitation speeds of 50, 75 and 100 rpm.
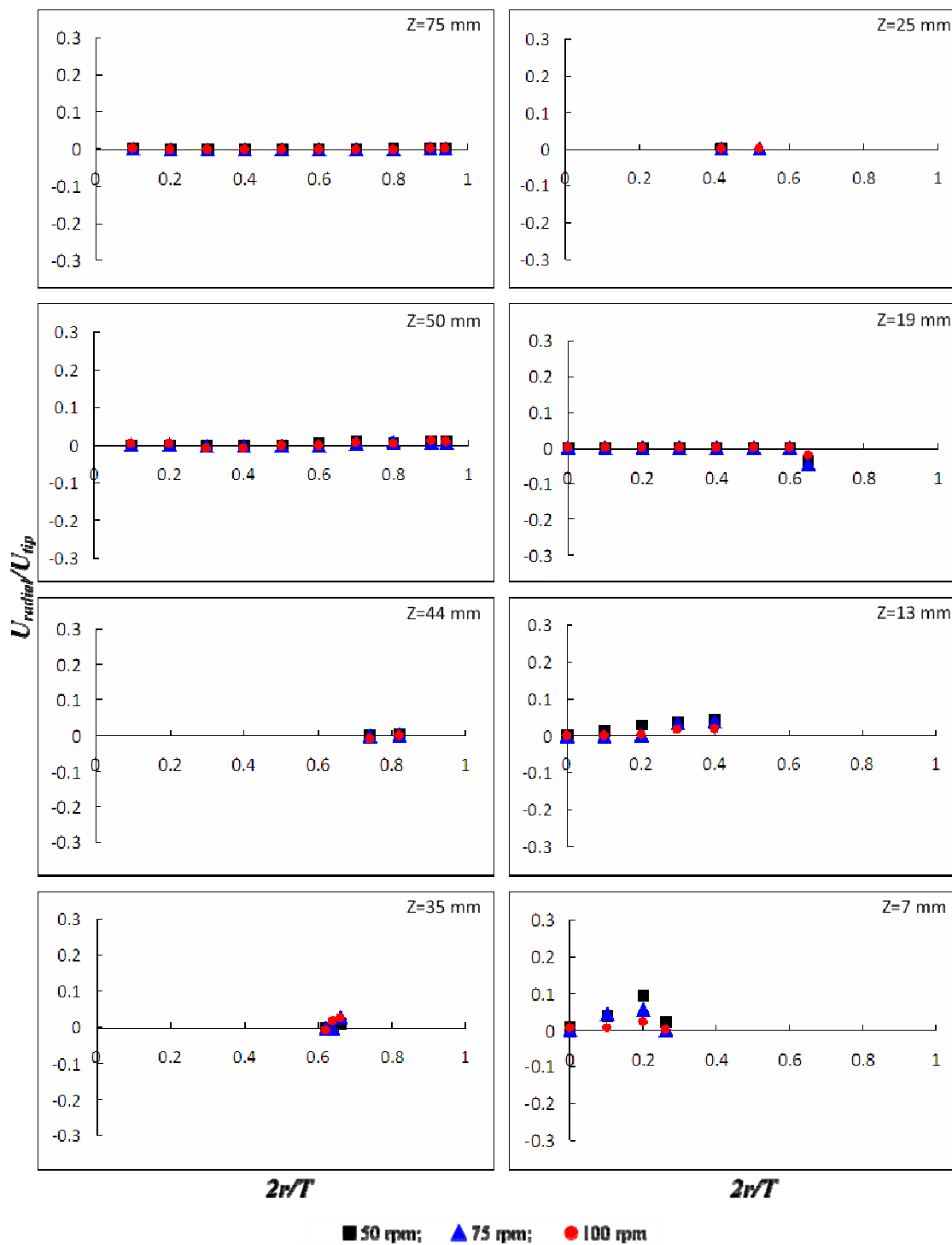
Figure 2.7 LDV measurements for radial velocities on eight iso-surfaces in standard Apparatus 2 (900 mL water) at agitation speeds of 50, 75 and 100 rpm.

2.3.2 Velocity Distribution (500 mL)

The fluid flow in 500 mL system has a similar flow pattern as that in 900 mL system.

2.3.2.1 Velocity Profiles above the Impeller. Figure 2.8 shows that all the tangential velocities above the impeller (iso-surfaces z=75 mm and z=50 mm) are in same direction of the impeller rotation (all positive values). The LDV data shows that on both iso-surfaces, and for all agitation speeds, the tangential velocities increase from near zero at the impeller shaft to peak values which are about 45% of impeller tip speed at similar radial positions (0.4<$2r/T$<0.5). The LDV tangential velocity data decreases gently in the region 0.5<$2r/T$<0.9. When LDV measurements are taken very close to the vessel wall ($2r/T$=0.98), the tangential velocities drop to 25% of the impeller tip speed on the iso-surface at z=75 mm and to about 22% (50 rpm) to 30% (100 rpm) on the iso-surface at z=50 mm, which is what one would expect since the velocity at the wall must be zero. On iso-surface z=75mm, in the region for which $2r/T$<0.3, the axial velocities are very small above the impeller, irrespective of agitation speed (Figure 2.9). On the iso-surfaces at z=75 mm, and z=50 mm, the axial velocities are negative (downward flow) for 0.4<$2r/T$<0.8, while an upward flows occurs when 0.8<$2r/T$<1.0 for all three impeller agitation speeds. Finally, Figure 2.10 shows that radial velocities in the region above the impeller are extremely low compared to the tangential velocity component.

2.3.2.2 Velocity Profiles around the Impeller. Figure 2.8 shows that in the impeller region, the tangential velocity magnitude for all three impeller agitation speeds follows same pattern, i.e., higher close to the impeller and lower close to the vessel wall. The LDV measurements show that the non-dimensional tangential velocity profiles do not change with increasing impeller agitation speeds except for measurements close to the

wall or next to the impeller. In Figure 2.9, the LDV measurements for iso-surface $z=44$ mm show that the non-dimensional axial velocity increases rapidly with radial distance, irrespective of impeller speed, thus generating an upwards flow next to the wall. On iso-surface $z=35$ mm, the non-dimensional axial velocities from LDV measurements start being directed downward in the region of $0.6<2r/T<0.8$ and directed upward in the region of $0.8<2r/T<1.0$. Finally on the iso-surface at $z=25$ mm (Figure 2.9) the LDV measurements turn from minimally positive (for $0.4<2r/T<0.7$) to appreciably negative (for $0.7<2r/T<0.8$) indicating a stronger downwards flow next to the vessel wall. For radial velocities (Figure 2.10), only a limited number of LDV measurements could be collected on the three iso-surfaces in the impeller region. The LDV measurements are found to be close to zero on iso-surface $z=25$ mm. On iso-surface $z=44$ mm, radial velocities are almost zero while the radial velocities are about 20% of the tip speed on iso-surface $z=35$ mm, indicating the velocities are directing toward the vessel wall. These measurements are repeated between three and six times to confirm the precision of the measurements.

2.3.2.3 Velocity Profiles below the Impeller. The tangential velocity profiles for the iso-surfaces below the impeller (at $z=19$ mm, $z=13$ mm and $z=7$ mm) presented in Figure 2.8 show that the non-dimensional velocities increase nearly monotonically with radial distance up until nearly the wall (remark: for these iso-surfaces the vessel wall is not found at $2r/T=1.0$, as in the cylindrical section of the vessel, but at $2r/T<1.0$ because of the curvature of the hemispherical vessel bottom). All the tangential velocity profiles in this region show a distinct pattern. In the inner core region (for $2r/T<0.2$ for iso-surfaces $z=19$ mm and $z=13$ mm and for $2r/T<0.3$ for iso-surface t $z=7$ mm) the non-

dimensional tangential velocity starts at about zero and increases linearly with the radial distance, thus making the fluid move in a solid body rotation, at least in the tangential direction. In the outer region, the non-dimensional velocity still increases to eventually reach a maximum, but not as steeply as in the core region, and some, although small, differences among the curves at different agitation speeds can be noticed. For the profile near the vessel bottom ($z=7$ mm), the core region extends almost up to the wall, making the fluid in this region swirl around the center line, where the velocity is zero or very close to it. The velocity profiles for the same iso-surfaces reported in Figure 2.9 show that the non-dimensional axial velocities are weak and generally positive, i.e., generating an upward flow below the impeller blade, while they become negative, implying a downward flow, only near the wall. This phenomenon creates a weak but clearly detectable vertical recirculation loop. As for the radial velocities below the impeller, on iso-surface $z=19$ mm in Figure 2.10, the non-dimensional radial velocities are very close to zero for $2r/T<0.6$, independently of the change in agitation speed. On iso-surface $z=13$ mm, the axial velocities by LDV measurements show weakly outward velocities. On iso-surface $z=7$ mm, radial velocity is small in the tested region.
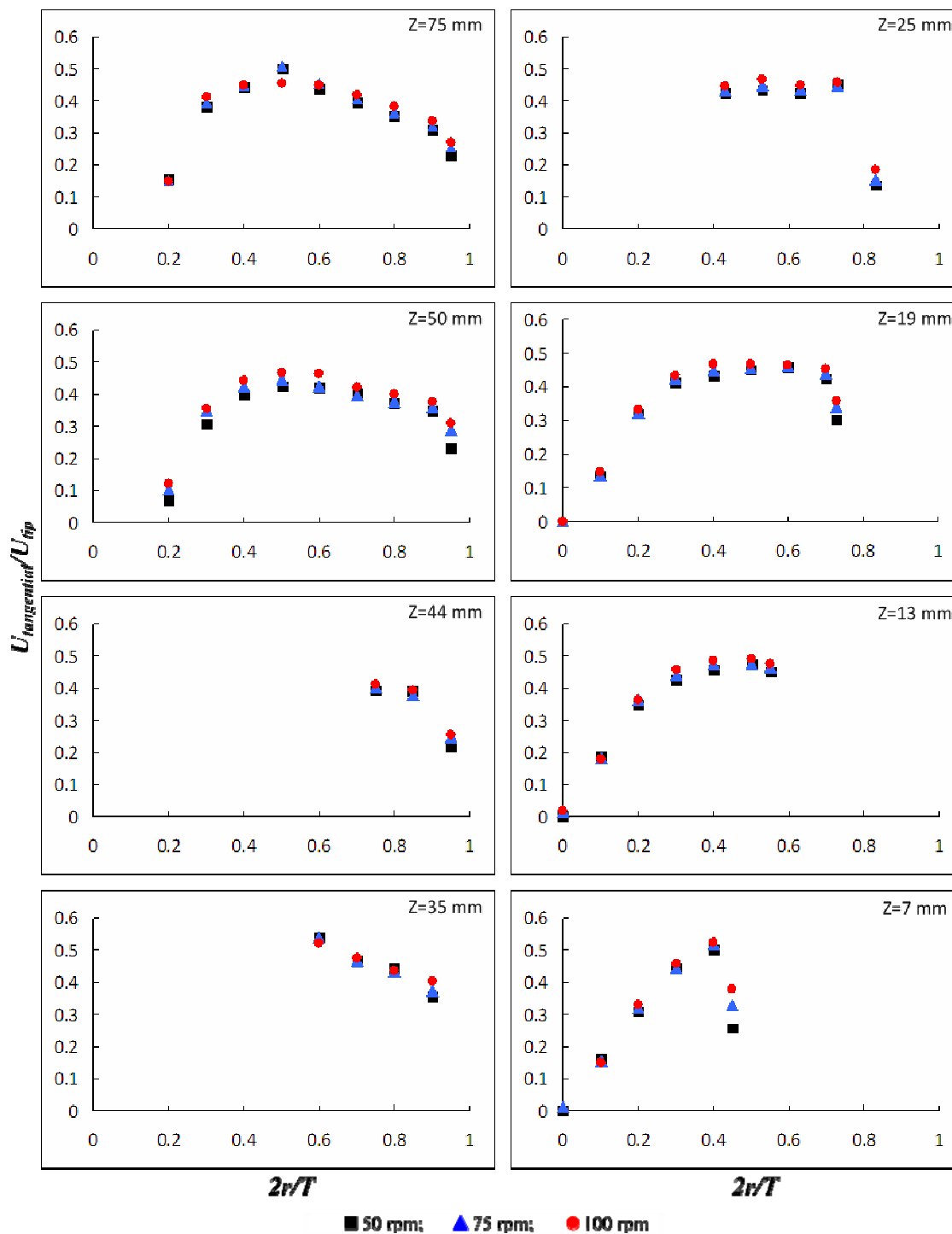
Figure 2.8 LDV measurements for tangential velocities on eight iso-surfaces in standard Apparatus 2 (500 mL water) at agitation speeds of 50, 75 and 100 rpm.
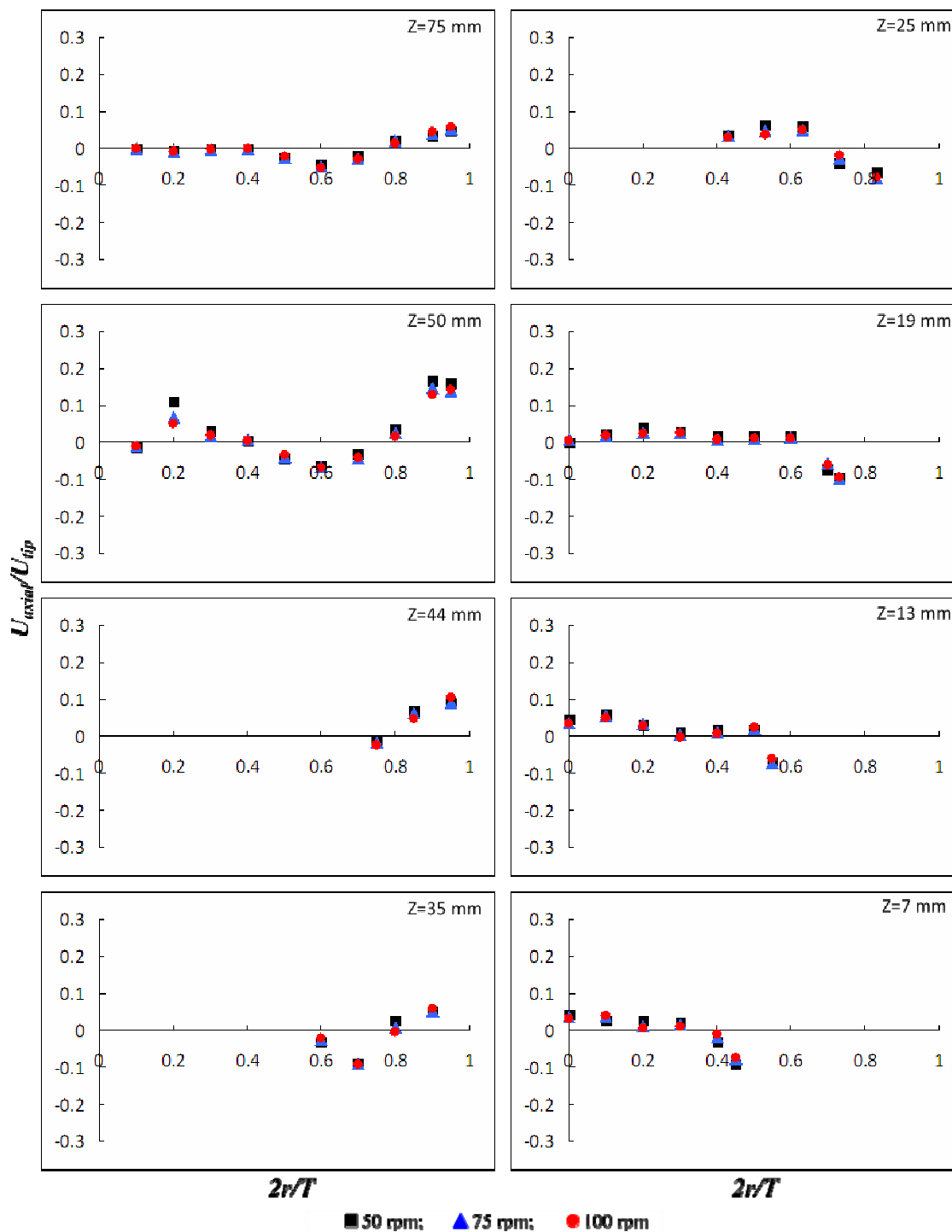
Figure 2.9 LDV measurements for axial velocities on eight iso-surfaces in standard Apparatus 2 (500 mL water) at agitation speeds of 50, 75 and 100 rpm.
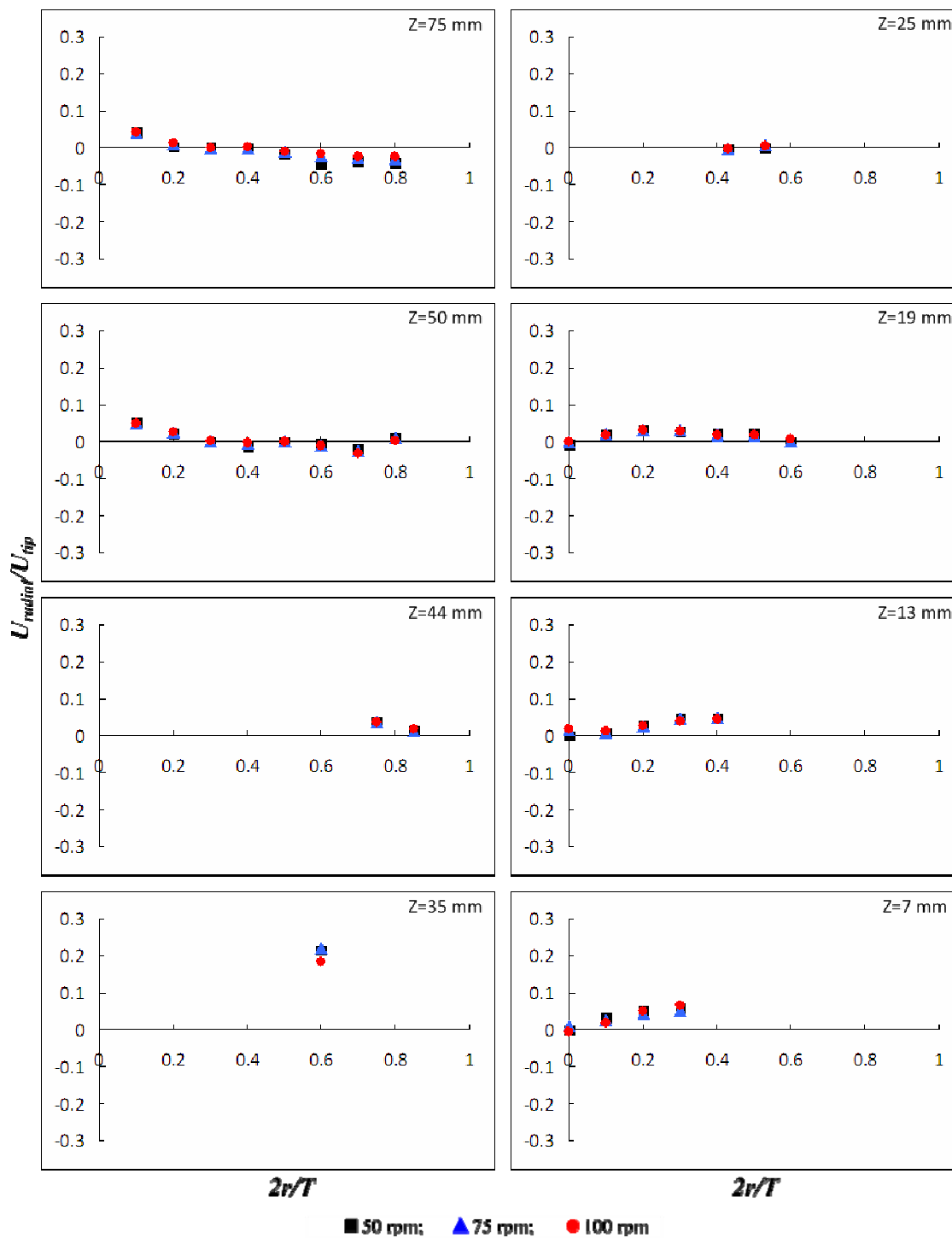
Figure 2.10 LDV measurements for radial velocities on eight iso-surfaces in standard Apparatus 2 (500 mL water) at agitation speeds of 50, 75 and 100 rpm.

In addition, the three-dimensional velocity distributions in Apparatus 2 with 900 mL and 500 mL water are obtained by PIV as well. Since the results are very similar with LDV results analyzed here, the PIV velocity distributions can be found in Appendix A.

2.4   Discussion

The results presented in this work show that LDV and PIV experimental methods used here are able to capture the details of the flow in Apparatus 2 vessel, including those relevant to the zone where tablet dissolution takes place.

The results presented here show that the hydrodynamics in Apparatus 2 vessel is quite complex at any agitation speed. The three-dimensional flow pattern in the Apparatus 2 vessel can be obtained at different impeller agitation speeds. Clearly, the tangential velocity component is the dominant flow feature in Apparatus 2 vessel at all agitation speeds. The experimental data shows that the largest values of the tangential velocities on all iso-surfaces investigated in this work are between 40 %-50 % of the impeller tip speed. In the upper portion of the vessel, this value of the tangential velocity extends over a significant portion of the radial coordinate, thus forming a "velocity plateau" region. The non-dimensional velocity profiles at different agitation speeds are typically remarkably similar to each other, implying that the tangential velocities scale up very well with the impeller agitation speed. The close similarity of the non-dimensional curves in this region implies that increasing the impeller agitation speed results in a direct and proportional increase in the tangential flow below the impeller.

Compared to the tangential velocities, both the axial flow and the radial flow are typically much weaker in terms of magnitude, irrespective of impeller agitation speed and

location within the vessel. In general, radial velocities are even weaker than axial velocities: the highest axial velocity obtained by LDV measurements is about 15% of the impeller tip speed (50 rpm; iso-surface at $z=50$ mm; Figure 2.6) and the highest radial velocity obtained by LDV measurements is only about 10% of impeller tip speed (50 rpm; iso-surface at $z=7$ mm; Figure 2.7). However, the typical axial and radial velocities are much smaller than these peak values, confirming that Apparatus 2 vessel is a relatively poor mixing device in the axial and radial directions at any impeller speed, as also previously reported [17]. In the inner core region, increasing the agitation speed has a negligible effect on the relative axial as well as radial velocities ($z=7$ mm). For the radial velocity component, the LDV data seem to indicate that the non-dimensional radial velocity actually decreases with increasing impeller speeds in this region, implying that even doubling the agitation speed from 50 to 100 rpm would not change the absolute value of the radial velocity near the vessel bottom for $2r/T<0.1$.

Since the tablet is typically located in this inner core region, at first glance these results would hardly justify increasing the agitation speed to increase dissolution effects. However, three other factors need to be considered. The first is that the tangential velocity component increases linearly with radial distance everywhere in the vessel, including in the inner core region below the impeller ($z=7$ mm). This implies that the thickness of the boundary layer surrounding a non-disintegrating tablet in this region can be expected to decrease with increasing agitation speeds, resulting in an increase in the mass transfer rate and a faster dissolution process. The second factor to be considered is that in the outside the inner core region, i.e., for $2r/T>0.1$ (and especially for $2r/T=0.3$), there is a small region where the non-dimensional axial and radial velocities values are

similar at different agitation speeds, which means that increasing the agitation speed indeed results in an increase in the actual values of axial and radial velocity components in the fluid there. This, in turns, could have an impact on disintegrating tablets since the tablet fragments in this outer core region will be pushed a bit more strongly in the positive radial direction (i.e., outward) as the impeller speed is increased, where the axial velocity component would produce the necessary lift. However, and more importantly, in order for the fragments to move to this outer region they need to leave the inner core region first. Therefore, the third and more critical factor is that the increased tangential velocities generated everywhere when the agitation speed is increased can produce a stronger centrifugal force on the tablet fragments even when they are in the inner core region because of the density difference between the solids and the liquid.

This analysis shows that the key to fragment suspension cannot be attributed to an increase in the axial and radial velocity components in the inner core region below the impeller as a consequence of increases in the agitation speed, but it is rather the result of an increase in the tangential velocity everywhere in the vessel (including the inner core region below the impeller), which translates into greater centrifugal forces on the solids and the possibility for them of "escaping" the quiescent inner core region, entering the outer region below the impeller, and only then becoming suspended. In other words, increasing the impeller speed does not appear to produce higher axial velocities in the inner lower core region of the vessel capable of lifting the tablet fragments, but it rather generates larger tangential velocities and flow instabilities which are indirectly capable of moving the solids from the inner core to the external region outside it, where the axial flow is higher (even at 50 rpm) and solid suspension can take place. Increasing the

agitation speed is in fact the typical strategy used by operators to help suspending particles and eliminate coning, although the velocity profiles obtained here and this analysis shows that this effect is not as strong and as direct as one would anticipate.

It should be additionally remarked that the exact location of the tablet on the vessel bottom during dissolution testing is critical for the rate at which the process occurs, and can result in statistically significant different dissolution curves, as previously shown [5]. This phenomenon is expected to be even more acute if the agitation is increased, since the flow field in which the tablet is immersed can be even more different depending on whether the tablet lies in the inner core zone below the impeller or outside it.

2.5 Conclusions

In this chapter, velocity profiles data obtained by LDV and PIV have been reported. Two common media volumes are tested, i. e., 500 mL and 900 mL. In addition, the agitation intensities were set at 50, 75 and 100 rpm, which are the prescribed agitation speeds according to the USP. In both the 900 mL system and the 500 mL system, there was little effect of agitation intensity on the non-dimensional mean velocity distribution (scaled with the impeller tip speed). As a result, similar flow patterns at 50, 75 and 100 rpm were found. In general, the tangential velocity plays a predominant role in the whole vessel. The axial and radial velocities are typically significantly lower than tangential velocity. In the upper portion of the vessel, the velocity distribution profiles are similar at different agitation speeds. The agitation speed almost does not change the proportionality between velocity and impeller tip speed. The non-dimensional velocity profiles and the flow patterns at different impeller agitations speed are generally very

similar to each other in Apparatus 2 vessel. Below the impeller, the tangential velocity profiles also show a trend similar to those above the impeller no matter how large the agitation speed is. The fluid flow in the bottom region of Apparatus 2 vessel is highly non-uniform. Even when the agitation speed is increased, such non-uniformity persists. A central inner core region can be found below the impeller where both axial and radial velocities are extremely low, regardless of the impeller agitation speed. The secondary recirculation loops below the impeller are not able to penetrate the central inner core region, where the axial and radial flows are typically weak but complex, irrespective of the impeller agitation speed.

The increase in tangential velocity magnitude resulting from higher agitation speeds is likely responsible for moving the tablet fragments from the inner core zone, where the solids are initially located during a dissolution test, to the surrounding region, where solids suspension can occur. Consequently, increasing the agitation speed can be an effective strategy to reduce or eliminate particle "coning" effects, promote particle suspension, and increase solid-liquid mass transfer and hence dissolution rate.

In conclusion, the hydrodynamics in Apparatus 2 vessel is very complex, especially below the impeller and in the center of the vessel bottom and this complexity may contribute to high variability in dissolution testing, even when the agitation speed is changed.

CHAPTER 3

EFFECT OF TABLETS LOCATIONS ON DISSOLUTION PROFILES IN THE MODIFIED USP APPARATUS 2

3.1   Introduction

Developing a suitable dissolution test requires careful consideration of operation variables such as the agitation speed, temperature control, dissolution medium, dosage form designs and other important variables [3], as well as geometric variables such as the type and dimensions of all the main components of the dissolution testing system. Several authors have examined a number of such variables. In 2009, Qureshi [35] studied how to select a dissolution medium for dissolution testing. He indicated that water or water-based solutions having a pH range of 5-7 at $37^{o}C$ were good candidates for dissolution testing. In addition, he suggested that making an appropriate dissolution medium should be a simple, practical and unbiased method.

Gao et al. [6] investigated the effect of de-aeration methods on dissolution tests. Nine de-aeration methods were studied. They concluded that it is important to determine if a dissolution medium has been sufficiently degassed. Gao et al. [7] also studied the vibration effects on dissolution tests with Apparatus 2. The authors recommended that in order to obtain more reliable dissolution results, it was necessary to isolate the dissolution apparatus from equipment that may induce vibrations.

Bai et al. [4] studied the influence of the position of the shaft and impeller in dissolution tests. Small changes in impeller location, especially if associated with loss of symmetry, produced extensive changes in velocity profiles and shear rates. Centrally located impellers, irrespective of their off-bottom clearance, produced non-uniform but nearly symmetric strain rates. The off-center impeller produced a more uniform but

41

slightly asymmetric strain rate distribution. The hydrodynamics of the system depended strongly on small differences in equipment configurations and operation conditions, which are likely to affect significantly the flow field and shear rate experienced by the oral dosage form being tested, and hence the solid–liquid mass transfer and dissolution rate. Bai et al. [5] explored the location of tablets during dissolution testing. They concluded that the exact tablet location had a significant impact on the dissolution profile.

Some researchers explored the influence of agitation intensity on the release profile. Hamlin [36] showed that when the agitation speed was increase, the sensitivity was reduced and it became more difficult to determine differences in dissolution rate. Dissolution test must be conducted at an appropriate agitation speed. Test conducted at high agitation rates may lose the ability to differential between good and bad products. Experiments conducted by Hamlin et al. [36] had also shown that variation in the boundary layer thickness due to changing agitation intensity can compromise the ability of the *in vitro* dissolution test to predict *in vivo* performance.

Shah et al. [31] indicated that dissolution testing must be conducted at an appropriate agitation rate. Tests conducted at high agitation rates may lose the ability to differentiate between good and bad products.

McCarthy et al. [26] simulated the hydrodynamics inside the Apparatus 2 vessel. A low-velocity region was evident directly below the center of the rotating paddle. Subsequently, McCarthy et al. [28] investigated the influence of paddle rotation speed on the hydrodynamics in the dissolution vessel via Computational Fluid Dynamics (CFD). The maximum velocity magnitude for axial and tangential velocities at different locations in the vessel was found to increase linearly with the paddle rotational speed. Kukura et

al. [24] demonstrated that under the current operation settings, Apparatus 2 operated in a regime where the flow was in incipient turbulence which may explain the possible inconsistencies in dissolution results. Later, Kukura et al. [27] showed with computational analysis that the shear environment in the vessel was highly non-uniform. Increasing the paddle speed from 50 to 100 rpm did not improve shear homogeneity within the Apparatus 2 vessel. The author concluded that the uneven distribution of hydrodynamic forces was a direct cause of dissolution testing variability. Baxter et al. [25] predicted sharp variations in the shear along the bottom of the vessel where the tablet was most likely to settle. Experiments in which the tablet location was carefully controlled revealed that the variation of shear within the testing device can affect the measured dissolution rate. A significant amount of work on the hydrodynamic characterization of Apparatus 2 vessel was also conducted by Armenante's research group [4, 5, 17, 18]

In recent years, some researchers and scientists have developed new methods or improved devices to conduct dissolution tests. Some articles suggested that new apparatuses for dissolution testing may cause less variability and more homogenous flow, and might even produce correlations with *in vivo* performance of the product. Qureshi [37] proposed a new crescent-shaped spindle to address the issues related to high variability and lack of bio-relevant of Apparatus 2 in 2004. Baxer et al. [38] use a PEAK vessel instead of Apparatus 2 vessel. A reduction in shear heterogeneity was observed in the region that the tablets are most likely to visit during testing. Peeters et al. [39] conducted dissolution testing using potentiometric sensors. The resulting dissolution profiles were very reproducible and exhibited a low variability compared to the

measurements using manual sampling and UV or HPLC analysis. They recommended that this method be standardized for *in situ* dissolution measurements. While these attempts showed recognition on the part of the pharmaceutical community of the problems associated with dissolution tests, they still did not fully address the non-reproducibility issue of the current method.

Dissolution testing has routinely been used to meet the regulatory requirements. It is useful for controlling the quality of oral products and rejecting bioinequivalent products. However, more concerns are raised that dissolution testing does not always ensure accurate performance. Several sources of variability in dissolution tests can affect the quality of the results. Even though calibrator tablets are used in a dissolution testing, the variability of results is a difficult problem to address. The release profile from Apparatus 2 does not always lead to a reproducible pattern. One of the reasons that can cause the non-repeatability of release profiles is the location of the tablet inside the vessel [18]. Since the tablet is manually dropped into the agitated vessel at the beginning of each test, it can be rest anywhere around the center of the bottom. The eventual location of the tablet seems to have a significant effect on the release profile. Armenante's group conducted the dissolution testing for two different kinds of drugs. Each drug was tested at four different positions (Figure 3.1) inside the bottom where the tablets are most typically located. The center of vessel bottom was defined as 0°. The other three positions were 10° off-center, 20° off-center and 40° off-center, respectively. The results for both drugs show that they have different release profiles at different drug locations. Although one is allowed to conduct six dissolution tests to get the average release profiles, the effect of tablet location cannot be ignored. Therefore, tablet location inside

Apparatus 2 vessel can be one of the main reasons which caused non-reproducibility. Therefore, one of the objective of this work was to develop a more stable system which the release profile is not going to be affected by the location of tablet.

(a)   (b)
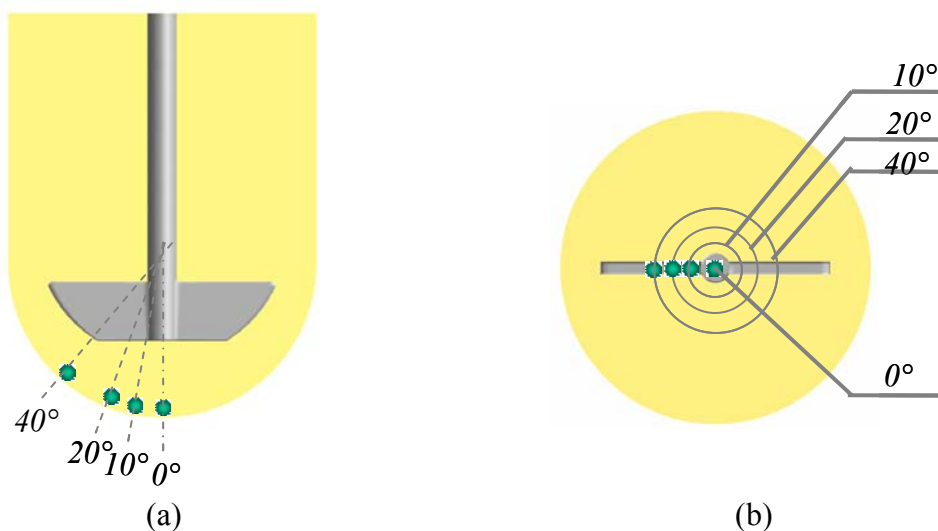
Figure 3.1 Four different positions in previous work [18]: (a) front view; (b) bottom view.

Chapter 2 indicated that poor reproducibility of dissolution testing data and inconsistency of dissolution results can arise from the complex hydrodynamics present in the unbaffled, hemispherical-bottom, agitated vessel that constitute the Apparatus 2 vessel. Armenante's group investigated the hydrodynamics in Apparatus 2 vessel and showed that the velocity distribution in the bottom region of the vessel, where the tablet was typically located and where dissolution occurs, was highly non-uniform and the flow pattern was highly variable.

In this chapter, a modified USP Apparatus 2 is described in which the impeller is placed 8 mm off center (Figure 3.2). This modified Apparatus 2 is similar to the existing one, but incorporates a key design change that makes the dissolution results of this

apparatus less sensitive to tablet location. The new design described here is quite simple and economic. Dissolution tests where calibrator tablets (prednisone and salicylic acid tablets) were placed at different positions on the vessel bottom are described here. These tests were conducted using both the standard Apparatus 2 and the modified Apparatus 2. In order to compare the statistical similarities between dissolution profiles at different tablets locations, a simple approach using a different factor (f_1) and a similarity factor (f_2) are employed.
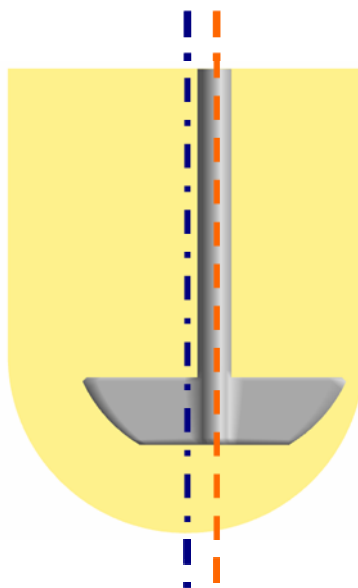
Figure 3.2 Illustration of modified Apparatus 2 vessel.

In this chapter, the modified USP Apparatus 2 system is referred to as "modified Apparatus 2", while the standard USP Apparatus 2 is still called "Apparatus 2".

3.2   Experimental Materials, Apparatuses and Methods

3.2.1 Materials and Apparatuses

Two types of calibrator tablets containing different drugs products were tested in this portion of the work, i.e., 10 mg prednisone calibrator tablets (disintegrating tablets; NCDA #2, which were kindly donated by Dr. Zongming Gao, Food and Drug Administration (FDA), Division of Pharmaceutical Analysis, Center for Drug Evaluation and Research, St. Louis, MO) and 300-mg salicylic acid calibrator tablets (non-disintegrating tablets; USP LOT Q0D200, purchased from USP, Rockville, MD).

Dissolution tests were conducted using a Distek Premiere 5100 dissolution system (Figure 3.3), containing seven built-in vessel positions. The volume of each vessel has a range of 500 mL to 1000 mL, which is programmable by setting parameters in the LED Display. The agitation rates can be digitally controlled from 25 rpm to 300 rpm with a resolution of 0.1 rpm. The accuracy of the agitation rate control is +/-0.2 rpm. The temperature of each individual vessel is continuously monitored and controlled with a resolution of $0.01^{o}C$. The accuracy of temperature control is +/-$0.25^{o}C$. The shafts wobble is controlled less than 0.010" TIR. All the settings can be changed by pressing up, down, left, right buttons on the 0.75 inch high output four-digit LED display screen.

Figure 3.3 Distek Premiere 5100 dissolution system.

The modified Apparatus 2 was a modified version of the standard Apparatus 2 system just described. Instead of changing the position of impeller and shaft, the vessel body was moved. In the original system, each vessel is centrally located within its hole in the metal plate (which supports all the vessels) with three plastic spring inserts. Here, one of these inserts was removed, producing a shift of the vessel sideways. As a result, the vessel body was translated horizontally by 8 mm with respect to its original position. Additional gaskets and support materials were inserted around the vessel to stabilize the vessel in its new position.

As described below in greater detail, in each experiment, a tablet was initially immobilized at one of nine different locations on the vessel bottom, i.e., at 0° (position 1), 10° (positions 2-5) and 20° (positions 6-9), as shown in Figure 3.4.
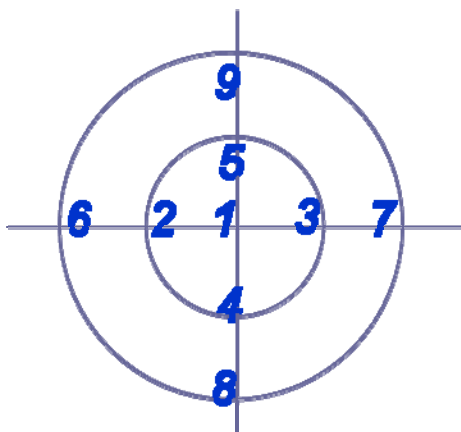
Figure 3.4 Different tablet locations in the bottom of the vessel.

3.2.2 Experimental Methods

Dissolution testing was conducted using two different kinds of solid oral dosage forms, i.e., prednisone tablets (10 mg) and salicylic acid tablets (300 mg). In the prednisone experiments, 500 mL of de-aerated water was used as the dissolution medium and the agitation rate was set up at 50 rpm. The UV wavelength used for prednisone detection in solution was 242 nm. In the salicylic acid experiments, the dissolution media was 900 mL de-aerated phosphate buffer and the agitation rate was 100 rpm at 37°C. The UV wavelength for salicylic acid detection was 296 nm. A PVDF 0.45 μm filter was used for sampling during the dissolution testing. Details of the experiments method are listed in Table 3.1.

Table 3.1 Detailed Operation Conditions of Dissolution Tests

	Prednisone tablet	Salicylic acid tablet
Dose	10 mg	300 mg
Medium	500 mL de-aerated, de-ionized water	de-aerated, 900 mL pH=7.4 buffer
Temperature	37°C	37°C
Agitation speed	50 rpm	100 rpm
Filter	PVDF 0.45 μm	PVDF 0.45 μm
UV wavelength	242 nm	296 nm
Standard Tablets	NCDA #2	USP salicylic acid tablets RS Lot Q0D200
Time	5 min interval; 45 min total	5 min interval; 45 min total

The experimental procedure used in this work was slightly different from that typically used in dissolution testing (USP, 2008) since the tablet was not dropped in the stirred dissolution medium but was glued in place prior to the addition of the dissolution medium and the beginning of the experiment.

Before each experiment, all key geometrical measurements were checked (impeller clearance, impeller position, etc.) and dissolution apparatus was modified by shifting the impeller 8 mm off center. In order to test the effect of tablet position during dissolution testing, a tablet was attached at a one of the nine predefined spots on the vessel bottom with a very small bead of commercial glue.

Once the tablet and the vessel were setup properly, the appropriate volume of the de-aerated dissolution medium, previously preheated at 37.5 °C, was gently poured into the vessel in order to minimize the introduction of gas and prevent the rapid initial dissolution of the tablet. Because of the thermal inertia of the vessel, the resulting

temperature of the liquid was 37 $^{\circ}$C. This temperature was maintained throughout the dissolution experiment by the system's temperature controller. The agitation was started immediately after the addition of dissolution medium.

The first sample was taken immediately after starting agitation. This data was defined as zero-time point. The time interval between samples was 5 minutes. Each experiment lasted 45 minutes and a total of 10 series of samples were taken for each experiment. Experiments were performed in six replicates for each tablet location in the modified system, and in triplicate for the standard system.

Sampling consisted of removing a 10-mL medium aliquot with a 10-mL syringe connected to a cannula (2 mm ID). The volume of medium removed by sampling was not replaced, in accordance to the USP procedure [1]. The sampling point was horizontally located midway between the impeller shaft and the vessel wall, and midway between the top edge of the impeller and the surface of the dissolution medium, i.e., within the sampling zone prescribed by the USP. After sample withdrawal, about 2-mL of the sample were discarded, the cannula was removed, and a PVDF 0.45 μm filter was mounted on the syringe. The remaining sample volume (about 8-mL) was transferred to a vial until analyzed.

Analysis of samples was carried out using and 1-cm quartz cells placed in a UV-visible spectrophotometer (Varian CARY 50 Bio) measuring absorbance at a specified wavelength, i.e., 242 nm for prednisone (the approximate wavelength of maximum absorbance) and 296 nm for salicylic acid.

3.2.3 Data Analysis

In recent years, FDA has placed more emphasis on dissolution profiles comparisons. Among several methods investigated for dissolution profile comparison, the one proposed by Moore and Flanner is the simplest. The approach uses a difference factor (f_1) and a similarity factor (f_2) to compare dissolution profiles [40]. The difference factor f_1 calculates the percent (%) difference between two curves at each time point and is a measurement of the relative error between the two curves. The difference factor can be calculated from:

$$f_1 = \frac{\sum_{t=1}^{n} |R_t - T_t|}{\sum_{t=1}^{n} R_t} \times 100 \qquad (3.1)$$

where n is the number of time points, R_t is the dissolution value of the reference at time t, and T_t is the dissolution value of the test location at time t.

The similarity factor (f_2) is a logarithmic reciprocal square root transformation of the sum of squared error and is a measurement of the similarity in the percent (%) dissolution between the two curves.

$$f_2 = 50 \log_{10} \{[1 + (\frac{1}{n}) \sum_{t=1}^{n} (R_t - T_t)^2]^{-0.5} \times 100\} \qquad (3.2)$$

A specific procedure to determine difference and similarity factors is as follows:

1. Determine the dissolution profiles of the testing and reference locations. (6 unit each)

2. Use the mean dissolution values from both curves at each time interval; calculate the difference factor (f_1) and similarity factor (f_2) using Equations 3.1 and 3.2.

3. For curves to be considered similar, f_1 value should be close to 0, and f_2 value should be close to 100. Generally, f_1 values up to 15 (i.e., in the range 0-15) and f_2 values greater than 50 (i.e., in the range 50-100) ensures sameness or equivalence of the two curves and, thus, of the performance of the test and reference locations.

This model is most suitable for dissolution profile comparison when three to four or more dissolution time points are available.

3.3   Results and Discussions

3.3.1 Dissolution of Disintegrating Tablets

The dissolution profiles for the 10 mg prednisone calibrator tablets were obtained in both the standard Apparatus 2 and in the modified Apparatus 2. The results are shown in Figure 3.5 (Apparatus 2) and in Figure 3.6 (modified Apparatus 2).

In Figure 3.5, the dissolution behavior of prednisone at different positions is shown with time. C/C^* is the relative concentration of prednisone during experiments. The dissolution testing curves obtained at 10 degree and 20 degree show different release behaviors compared with the reference position. Dissolution curve of reference position start with C/C^*=0.06 (6%), and then increase linearly reaching C/C^*=0.48 (48%) over the next 35 minutes. In the last ten minutes, prednisone is released at a lower release rate. The concentration at t=45 minutes is C/C^*=0.51 (51%). At 10 degree and 20 degree, dissolution curves start at the same C/C^* as that at reference position. In the initial five minutes, dissolution curves show faster dissolution rates (C/C^*~30%) compared with reference position (C/C^*=0.14 (14 %)). From t=5 to t=25 minutes, dissolution curves are parallel to the curves obtained at reference position. From t=25 to t=35 minutes,

dissolution rates decrease slight and show the same dissolution rates as reference position in the last ten minutes. In general, the main difference between the dissolution curves occurs during the initial five minutes.

The dissolution behavior difference in the first five minutes is probably due to the different hydrodynamic environments at different tablet locations. As demonstrated in Chapter 2, fluid flow in the center of the bottom region of the vessel has the most variable and extremely small velocities. From the center core to the outer core region in the bottom, velocities change significantly and become larger. Different fluid flow can introduce different forces and shear rate on the surface of the prednisone tablet, which can consequently influence the disintegration and release rate of prednisone. For example, in the first five minutes, when the tablet is still glued to a pre-defined location, a prednisone tablet at 20° experiences a much larger velocities compared to a tablet at the 0° location, which increases the disintegration and dissolution rates as showed in Figure 3.5. After the initial five minutes, the prednisone tablets break into small fragments, which are no longer glued and fixed to specific positions. Since these fragments are now free to move, they travel to a position which has the lowest energy in the system, i.e., they move to the same central location irrespective of where they were initially placed. Now the fragments experience the same fluid environment and consequently show the same release behavior.

In the standard Apparatus 2, at 10 degrees and 20 degrees, the difference factors were found to be 32.6 and 37.8, and the similarity factors are around 46.7 and 44.4, respectively, which are out of predefined ranges for difference factors (0-15) and

similarity factors (50-100). In general, the difference factors and similarity factors obtained from different positions indicate the differences with reference position.
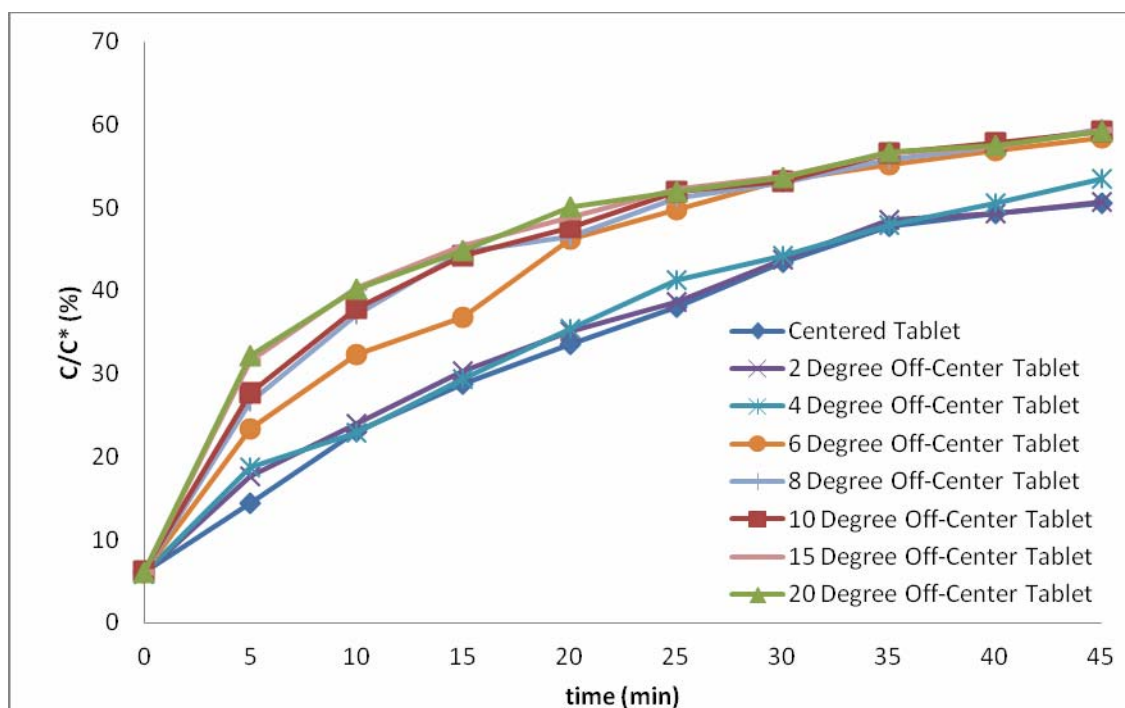
Figure 3.5 Dissolution results of prednisone tablets in standard Apparatus 2.

Table 3.2 Similarity Factor and Difference Factor of Prednisone Tablets in Standard Apparatus 2

Position	Difference factor (f_1)	Similarity factor (f_2)
10 degrees	32.6	46.7
20 degrees	37.8	44.4

In Figure 3.6, the nine dissolution profiles for prednisone tablets at nine different tablet locations in the modified Apparatus 2 are plotted together in order to have a clear comparison of the result. Although the tablets are located at nine different locations, the release profiles almost overlap. They all have a very similar release pattern, which indicates that the position of the tablet does not affect the dissolution results. In the first

ten minutes, the plot shows that the dissolution rate is very fast. The relative concentration is more than 0.5 (50 %). From $t=10$ to $t=20$ minutes, the dissolution rate shows a transition period. The release rate tends to be smooth when compared to the initial ten minutes. The relative concentration changed from 0.6 (60 %) to 0.8 (80 %) gradually. In the last 25 minutes, the release rate is more limited. The relative concentration varied from 0.8 (80 %) to 0.95 (95 %). The fastest release rate of prednisone tablets occurred in the first ten minutes.

In the modified Apparatus 2, the release data shows a very consistent and reproducible trend even when the tablets are in different locations when compared to the standard system.

In order to have a more accurate and quantitative comparison, difference factor and similarity factor were calculated and are listed in Table 3.3. The maximum of the similarity factors is 78.8 and the minimum is 63.0. All the similarity factors are located in the region between 50 and 100, which indicated that the test release profiles are statistically similar to the reference release profile. The difference factors range from 3.1 to 5.1, showing a very small difference between the test release profile and the reference release profile. Both the similarity factor and difference factor ensure the sameness between two release profiles.
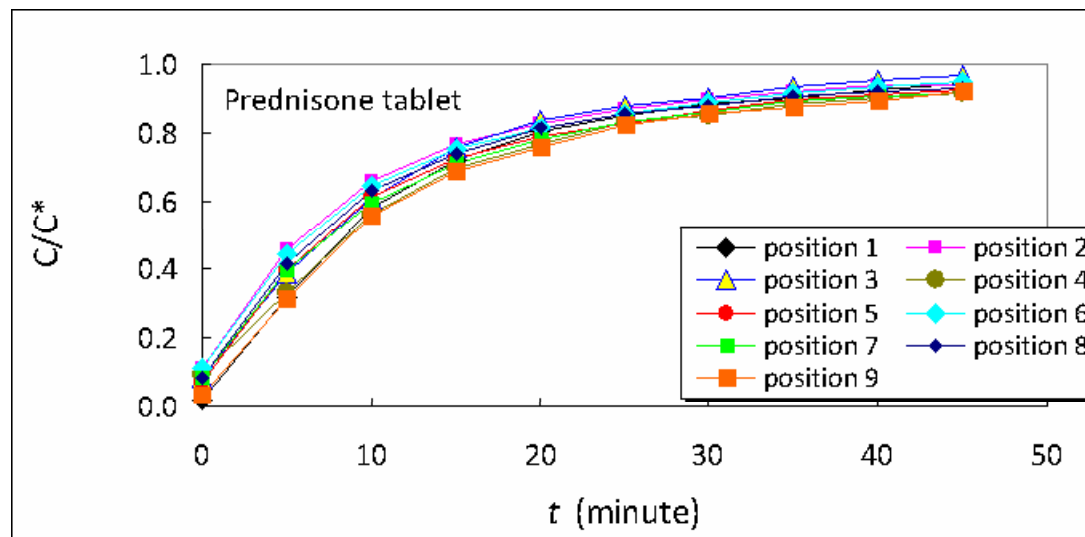
Figure 3.6 Dissolution results of prednisone tablets in modified Apparatus 2.

Table 3.3 Similarity Factor and Difference Factor of Prednisone Tablets in Modified Apparatus 2

Position #	Difference factor (f_1)	Similarity factor (f_2)
2	5.1	63.0
3	4.3	72.2
4	3.3	78.8
5	3.1	74.4
6	3.9	66.0
7	3.3	74.6
8	3.1	71.1
9	3.7	75.6

3.3.2 Dissolution of Non-Disintegrating Tablets

The 300-mg salicylic acid calibrator tablets were tested in both the standard Apparatus 2 and the modified Apparatus 2. The results are shown in Figure 3.7 (standard Apparatus 2) and in Figure 3.8 (modified Apparatus 2).

Overall, the three curves (0 degree, 10 degrees and 20 degrees) increase linearly during the 45 minutes. At 10 degree position and 20 degree position, dissolution curves start at the same C/C^* as that at reference position and increase linearly with experiment time. Final C/C^* reaches ~31%. The difference between the testing positions and the reference position becomes greater with time. Since the salicylic acid tablets are non-disintegrating tablet, during the whole dissolution testing, tablets do not break into small fragments. Instead, the tablets slowly erode in the dissolution fluid. Since salicylic acid tablets are initially and permanently glued and fixed at different pre-defined locations, the fluid environments are totally different at different sites in the bottom region throughout the entire test. Tablets experience different hydrodynamic environments during the entire test. Therefore, the release behaviors of salicylic acid tablets are different, and the difference increases with experiment time.

In Apparatus 2, at 10 degrees position and 20 degrees position, the difference factors were found to be 36.2 and 55.5, and the similarity factors are around 66.7 and 58.1, respectively, which are out of predefined range for difference factors (0-15) and the similarity factors (50-100). In general, the difference factors and similarity factors obtained from 10 degrees positions and 20 degrees position indicate a big difference compared with the reference position.
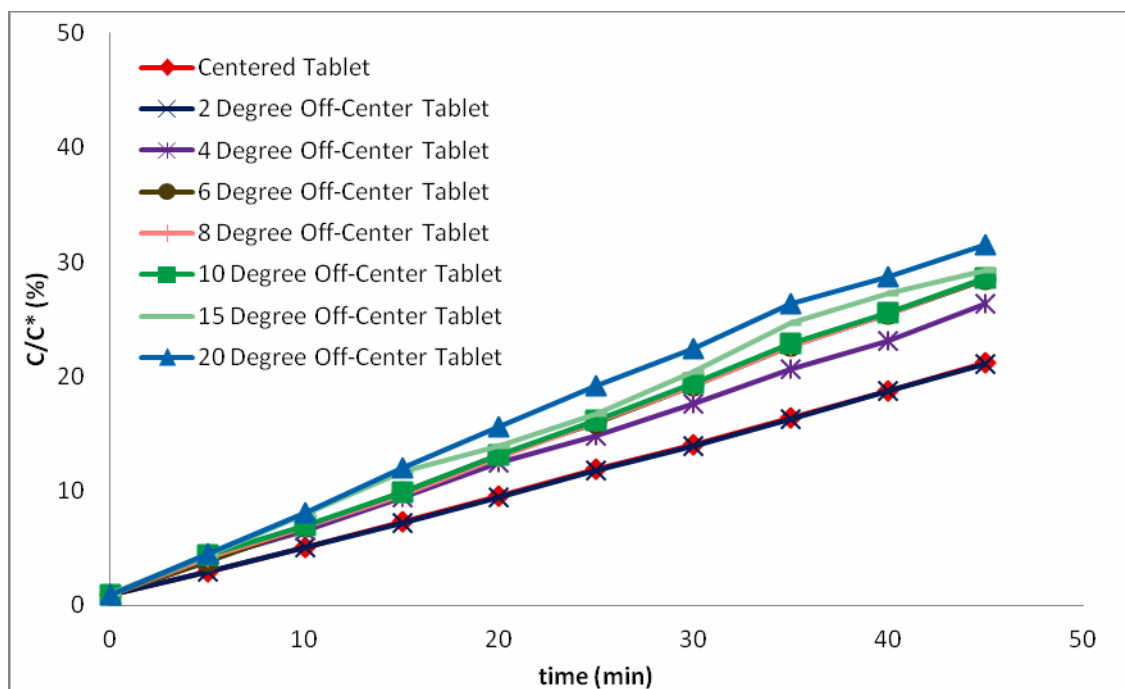
Figure 3.7 Dissolution results of salicylic acid tablets in standard Apparatus 2.

Table 3.4 Similarity Factor and Difference Factor of Salicylic Acid Tablets in Standard Apparatus 2

Position	Difference factor (f_1)	Similarity factor (f_2)
10 degrees	36.2	66.7
20 degrees	55.5	58.1

In Figure 3.8, nine dissolution profiles from the modified Apparatus 2 are plotted together. Although the tablets are located at nine different locations, the release profiles almost overlapped. They all have a very similar release pattern, which indicates that the position of the tablet did not affect the dissolution results. Unlike the prednisone tablets, the release pattern of the salicylic acid tablets looks more linearly from $t=0$ to $t=45$ minutes. In the modified Apparatus 2, the release data shows a very consistent and reproducible trend even when the tablets are in different locations when compared to the standard system.

The maximum of the similarity factor is 88.0 and the minimum is 67.5 (Table 3.5). All the similarity factors are located in the range of 50 to 100, indicating that the test release profiles are very similar to the reference release profile. The difference factor ranges from 4.7 to 14.9, which shows that difference between the test release profile and the reference release profile meet the testing criteria. The difference factor of salicylic acid tablet is higher than that of prednisone tablet. Both the similarity factor and difference factor ensured equivalence between two release profiles.
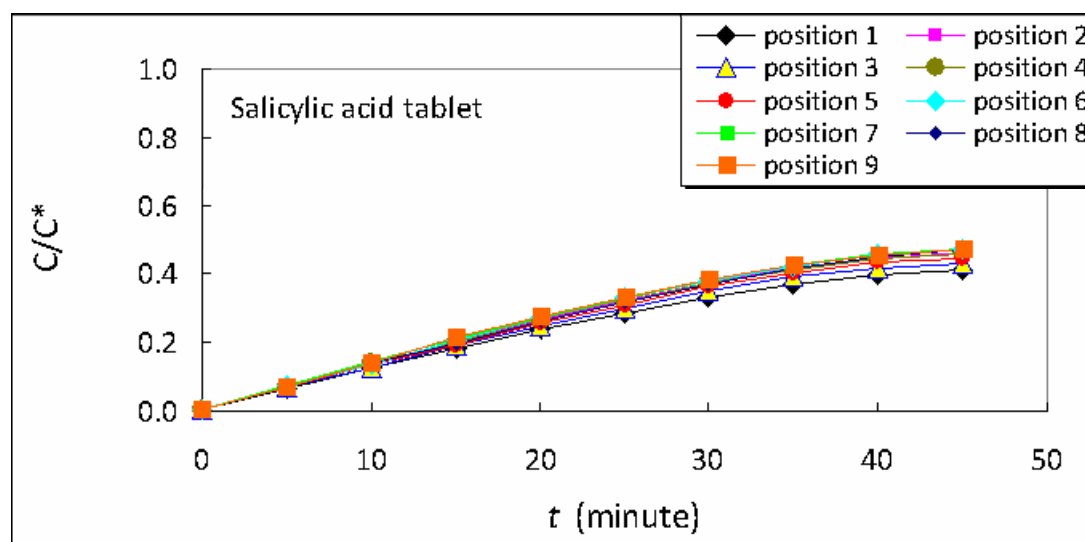
Figure 3.8 Dissolution results of salicylic acid tablets in modified Apparatus 2.

Table 3.5 Similarity Factor and Difference Factor of Salicylic Acid Tablets in Modified Apparatus 2

Position #	Difference factor (f_1)	Similarity factor (f_2)
2	12.2	71.7
3	4.7	88.0
4	11.4	72.8
5	8.5	78.5
6	14.2	68.2
7	14.7	68.7
8	11.7	71.4
9	14.9	67.5

3.4   Conclusions

Dissolution testing was conducted on two kinds of drugs in the modified dissolution testing system. Both prednisone tablet, a disintegration tablet, and salicylic acid tablet, a non-disintegration tablet showed similar and reproducible release profiles irrespective of where the tablet were located at the bottom of the vessel. Furthermore, by calculating similarity factor f_2 and difference factor f_1, a more accurate and quantitative conclusion was obtained. The similarity factors f_2 between for the curves at different tablet locations and the curve for the centrally located tablet were always in the range of 50 to 100, which implies that the release profiles at positions 2 to 9 are very close to that at position 1, the reference position.   For prednisone tablets, the difference factors f_1 were very low, indicating that the difference between position 2 to 9 and position 1 are very small. The difference factors f_1 for salicylic acid tablet were also small, although slightly larger than those for the prednisone tablets. Therefore, it can be concluded that the dissolution rate

in the modified Apparatus 2 is independent of the locations of tablets.

Robust and consistent dissolution rate were observed in the modified Apparatus 2. This new system could possibly be used to improve the reliability of dissolution tests in the future.

CHAPTER 4

CFD DETERMINATION OF VELOCITY PROFILES IN STANDARD AND MODIFIED APPARATUSES 2

4.1 Introduction

In previous research work by this group [4, 5, 17, 18], it was shown that the hydrodynamics is an important factor in dissolution testing in Apparatus 2 vessel. The effect of a number of variables on the hydrodynamics was quantified first, and then their impact on dissolution rates was experimentally and computationally determined. More specifically, a detailed mapping of the flow field was experimentally conducted and the velocity distribution was then computationally determined and compared with the experimental results. The effect of varying the impeller position (within the range specified by USP) and the tablet locations was also experimentally and computationally assessed, and it was found that even small changes in these variables introduced significant variability in the hydrodynamics of the system, and, more importantly, in the dissolution rates. The main reason for this behavior lies in the complex hydrodynamics in the bottom region of the vessel, which in turn governs the dissolution process.

In Chapter 3, further exploration was conducted on the effect of operating variables on the existing USP Apparatus 2, and how the existing Apparatus 2 can be simply modified to add robustness to the system as far as dissolution testing reproducibility is concerned. The effect of the exact location of the impeller on the system's hydrodynamics and the dissolution rate of tablets were investigated. The impeller was placed 8 mm away from the centerline of the vessel and it was found that the 8 mm off-center impeller significantly improved the dissolution testing results. In

additional work where the dissolving tablets were placed at nine different locations on the vessel bottom, the dissolution curves determined experimentally were no longer affected by the tablets positions.

In this chapter, the computational predictions of the velocity profiles in both the standard Apparatus 2 and the modified Apparatus 2 are presented and the computational results are compared with experimental results.

Numerical simulations of the velocity distribution inside the standard Apparatus 2 and the modified USP Apparatus 2 were conducted using a commercial mesh generator (GAMBIT 2.4.6) coupled with a computational fluid dynamic (CFD) package (FLUENT 6.3.26). The full 360° tank geometry was incorporated in the simulations. The exact geometry of each component of the system (such as the glass vessel, impeller shaft, impeller blades, etc.) was obtained by measuring the actual dimensions with a caliper. The geometry data were then inserted in the mesh generator to get the exact shape of the volume in which the numerical CFD simulation was conducted.

4.2   Computational Tools

4.2.1 CFD Commercial Software Package [41, 42]

A mesh generator, GAMBIT 2.4.6, was used to generate the geometry and mesh inside the standard Apparatus 2 and the modified Apparatus 2. A mixed mesh, including structured Cooper-type hex mesh and T-Grid mesh were created in the cylindrical part of the vessel and in the hemispherical bottom to follow the curved shape more accurately.

ANSYS FLUENT was used to numerically solve the general equations representing the conservation of mass and momentum. In Cartesian coordinates, the

continuity equation for an incompressible fluid using the summation convention can be written as in Equation 4.1.

$$\frac{\partial u_i}{\partial x_i} = 0 \tag{4.1}$$

Similarly, the momentum balance equation for the same incompressible fluid (Navier-Stokes equation) can be written as in Equation 4.2.

$$\frac{\partial u_i}{\partial t} + u_j \frac{\partial u_i}{\partial x_j} = -\frac{1}{\rho}\frac{\partial P}{\partial x_i} + v \nabla^2 u_i + g_i \tag{4.2}$$

In this equation, the second term on left hand side accounts for the convective momentum transport, while the terms on the right hand side represent, respectively, pressure forces, viscous transport, and body forces, such as gravity.

4.2.2 Multiple Reference Frame (MRF) Model [42]

The MRF model is, perhaps, the simplest approach for multiple zones. It is a steady-state approximation in which individual cell zones move at different rotational and/or translational speeds. While MRF approach is clearly an approximation, it can provide a reasonable model of the flow for many applications. For example, the MRF model can be used for turbo machinery applications in which rotor-stator interaction is relatively weak, and the flow is relatively uncomplicated at the interface between the moving and stationary zones. In mixing tanks, for example, since the impeller-baffle interactions are relatively weak, large-scale transient effects are not present and the MRF model can be

used. This approach can also be used in the standard Apparatus 2 and the modified Apparatus 2. MRF can also alternatively used as a starting flow condition for a sliding mesh calculation. When using the MRF model, two regions are created within the dissolution system. One region surrounds the impellers and extends some distance above and below them. This impeller grid region is stationary, but within it, the conservation equations are solved in a rotating frame. The rotation angular velocity of this region is the same as that of the impeller and shaft. Thus, no angular velocity is applied to the shaft or impeller blades, since the velocity of these elements is zero relative to the frame. The second region is associated with the outside walls of Apparatus 2 vessel. The conservation equations in this grid region are solved in the stationary frame of the vessel itself. Thus, no motion need be applied to the vessel walls, the upper surface. Values of the conserved quantities are matched at the interface between these two grid regions.

4.2.3 Sliding Mesh Model [42]

The sliding mesh model is the most general model for three-dimensional mixing tank simulations. It provides a time-dependent description of the periodic interaction in an asymmetric vessel. With this model, one grid region surrounds the impeller, extending some distance above, below, and radially beyond the blade tip. Another grid region is used for the rest of the vessel.

The cells that meet at the interface differ during the course of the solution, depending upon the orientation of the impeller grid relative to the stationary grid. As time progresses, the solution reaches a periodic steady-state condition, in which the flow field exhibits a repeating pattern as a single blade passes from one baffle to the next.

Although the sliding mesh model is the most accurate of all the mixing tank models, it is also the most expensive one to run from a computational standpoint. Instead of performing a single calculation to obtain a converged result, as is the case with steady-state flows, sliding mesh simulations advance forward in time using small time steps.

4.2.4 Turbulent Models [42]

FLUENT provides different turbulence model options during the numerical simulations. These models are the standard k-ε model, the RNG k-ε model, the realizable k-ε model, and the standard k-ω model. All three turbulence k-ε models have similar forms, with transport equations for k and ε. The major differences in the standard, RNG, and realizable k-ε models are as follows:

1. The method of calculating turbulent viscosity
2. The turbulent Prandtl numbers governing the turbulent diffusion of k and ε
3. The generation and destruction terms in the ε equation

The standard k-ε model is a semi-empirical model based on model transport equations for the turbulence kinetic energy k and its dissipation rate ε. The governing equations for standard k-ε model are as Equations 4.3 and 4.4.

$$\frac{\partial}{\partial t}(\rho k) + \frac{\partial}{\partial x_i}(\rho k u_i) = \frac{\partial}{\partial x_j}[(\mu + \frac{\mu_t}{\sigma_k})\frac{\partial k}{\partial x_j}] + G_k + G_b - \rho\varepsilon - Y_M + S_k \tag{4.3}$$

$$\frac{\partial}{\partial t}(\rho \varepsilon) + \frac{\partial}{\partial x_i}(\rho \varepsilon u_i) = \frac{\partial}{\partial x_j}[(\mu + \frac{\mu_t}{\sigma_\varepsilon})\frac{\partial \varepsilon}{\partial x_j}] + C_{1\varepsilon}\frac{\varepsilon}{k}(G_k + C_{3\varepsilon}G_b) - C_{2\varepsilon}\rho\frac{\varepsilon^2}{k} + S_\varepsilon \tag{4.4}$$

where $C_{1\varepsilon}$=1.44; $C_{2\varepsilon}$=1.92; C_μ=0.09; σ_k=1.0 and σ_ε=1.3.

In the derivation of the standard *k-ε* model, it is assumed that the flow is fully turbulent, and the effects of molecular viscosity are negligible. The standard *k-ε* model is, therefore, valid only for fully turbulent flows. Its main advantages are that it is robust and computationally economical.

4.2.5 Additional Computational Details

Simulations were carried out on a High Performance Computing Workstation. The operating system is RHEL Linux 4.2 Kernel 2.6.9 from the SUN Corporation, equipped with a maximum GFLOPS of 800 and 112 number of compute nodes, connected with a Gigabit Ethernet. Each node has one 2.4 GHz AMD Opteron Model 180 processor. In addition, the random access memory (RAM) of each processor was 2 GB. The RAM for each core was 1 GB. A typical computational run to calculate the flow field in the entire reactor for a multiple reference frame simulation took some 24-48 hours, depending on the different cases and number of cells. For a sliding mesh simulation, a typical computational run take around 2 weeks to complete.

CFD simulations were carried out for all experimental cases. For each of the simulations, a meshed grid was constructed using GAMBIT 2.4.6 using the strategy described above. The geometry of the vessel, shaft and impeller all matched the actual experimental equipment. The mesh files were used to conduct simulations through FLUENT 6.3.26. Agitation speeds of 50, 75 and 100 rpm, corresponding, respectively, to impeller tip speeds of 0.194, 0.291 and 0.388 m/s, and impeller Reynolds numbers equal to 4939, 7409 and 9878 were simulated. Simulations were conducted for two liquid volumes, i.e., 900 mL and 500 mL.

4.3   Results and Discussions

4.3.1 Validation of Velocity

Figure 4.1 shows the mesh for the standard Apparatus 2 and the modified Apparatus 2, in which the impeller was moved away 8 mm from the center of the vessel. The total system volume was separated into two separate volumes. The meshing for the simulation cases can be seen in Table 4.1 which summarizes their corresponding mesh and cell size information. The equiangle skew parameter is used to quantify the quality of mesh (0-best; 1-worst). Significant attention was paid to the generation of a high quality mesh, since this determined whether the simulation converged to a stable solution or not.
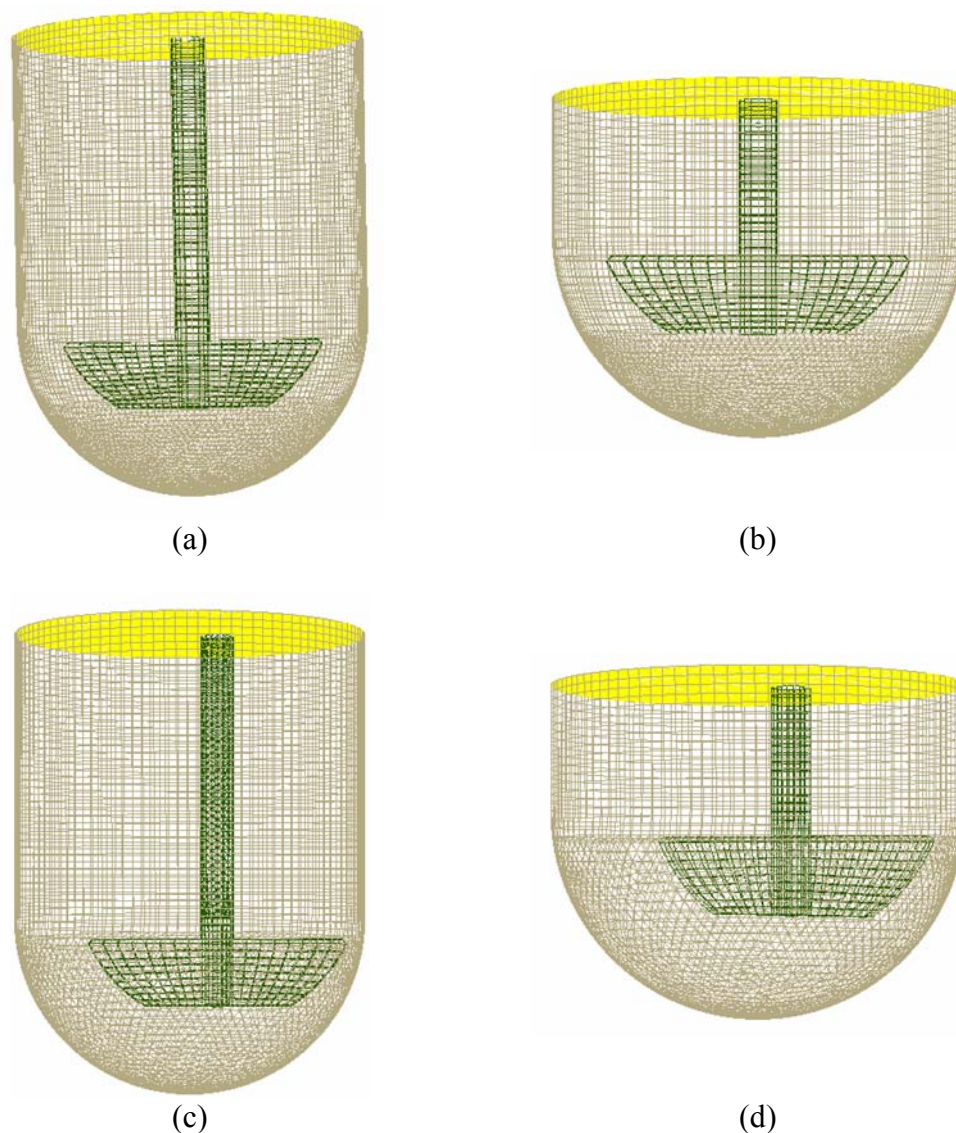
Figure 4.1 Geometric mesh for standard Apparatus 2: (a) 900 mL; (b) 500 mL and modified Apparatus 2: (c) 900 mL; (d) 500 mL.

Table 4.1 Geometric Mesh Information for Each Simulation Case

System	Cells	Faces	Nodes
Apparatus 2 vessel, 900 mL water	161831	454482	111754
Apparatus 2 vessel, 500 mL water	124919	333762	70234
Modified Apparatus 2 vessel, 900 mL water	213547	513251	67843
Modified Apparatus 2 vessel, 500 mL water	85538	224677	43632

Figure 4.2 show the effect of agitation speeds on velocities distributions and how the computational predictions matched the experimental LDV results in both Apparatus 2 and modified Apparatus 2. The tangential fluid velocity profiles on the horizontal iso-surface at z=75 mm was obtained using both experimental measurements and CFD simulations at three impeller agitation speeds, i.e., 50 rpm, 75rpm and 100 rpm, respectively. In this figure, the ordinates represent the normalized fluid velocity (scaled by using the impeller tip speed, U_{tip}) and the abscissas represent the normalized radial position (scaled using the vessel radius, $T/2$). The normalized tangential velocities scale up very well with agitation rates from both LDV experimental results and CFD predictions. At different agitation rates, the velocity profiles exhibit the same flow patterns. Therefore, the velocity distributions was predicted in the standard Apparatus 2 and modified Apparatus 2 only for the 50-rpm case , and were compared with corresponding experimental velocity distributions. Four iso-surfaces were selected. The iso-surface at z=75 mm was in the upper region of the Apparatus 2 vessel. Iso-surfaces at z=44 mm and z=25 mm are two surfaces in the impeller region. The iso-surface at z=13 mm is the surface below the impeller.
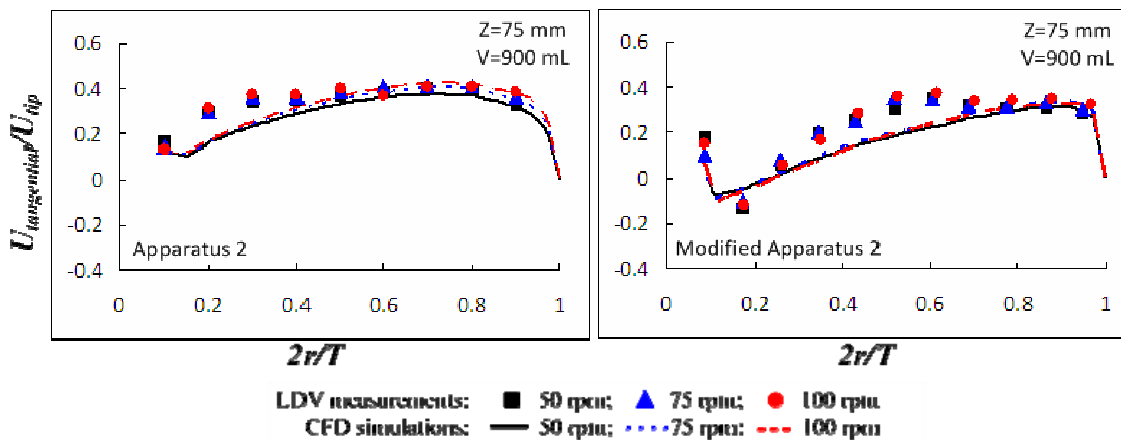
Figure 4.2 Experimentally and computationally determined tangential velocities on iso-surface z=75 mm in standard (left) and modified (right) Apparatus 2 (900 mL water).

4.3.1.2 Apparatus 2. Figures 4.3, 4.4 and 4.5 show CFD predictions and LDV measurements for tangential, axial and radial velocities, respectively. On the iso-surface at z=75 mm (Figure 4.3), the CFD predictions matched the LDV measurements quite satisfactorily in the region 0.6<$2r/T$<0.9. In the region of 0.1<$2r/T$<0.6, LDV measurements were slightly larger than the predicted tangential velocities. On the iso-surface at z=44 mm (900 mL), the non-dimensional, CFD-predicted, tangential velocities at $2r/T$=0.7, 0.9 were found to be higher and lower than the experimental results, respectively. It is clearly that even a small difference between the experimental z value and corresponding z value predicted computationally may result in appreciable discrepancies between the experimental velocity profiles and the corresponding CFD predictions. In addition, during the LDV experiments, the traverse system could not be continuously changed vertically and the shaft is wobbling slightly. All these factors could contribute to the deviation of LDV measurements from with CFD predictions. On the iso surface at z=25 mm (lower edge of the impeller blade), the CFD simulations showed a flow pattern ver similar to the LDV measurements. On iso-surface z=13 mm,

although the CFD simulations over predicted the experimental LDV velocity magnitudes,

both the CFD and PIV results showed a similar flow pattern. In Figures 4.4 and 4.5, the

predicted axial and radial velocities showed good matches with the LDV results as well.
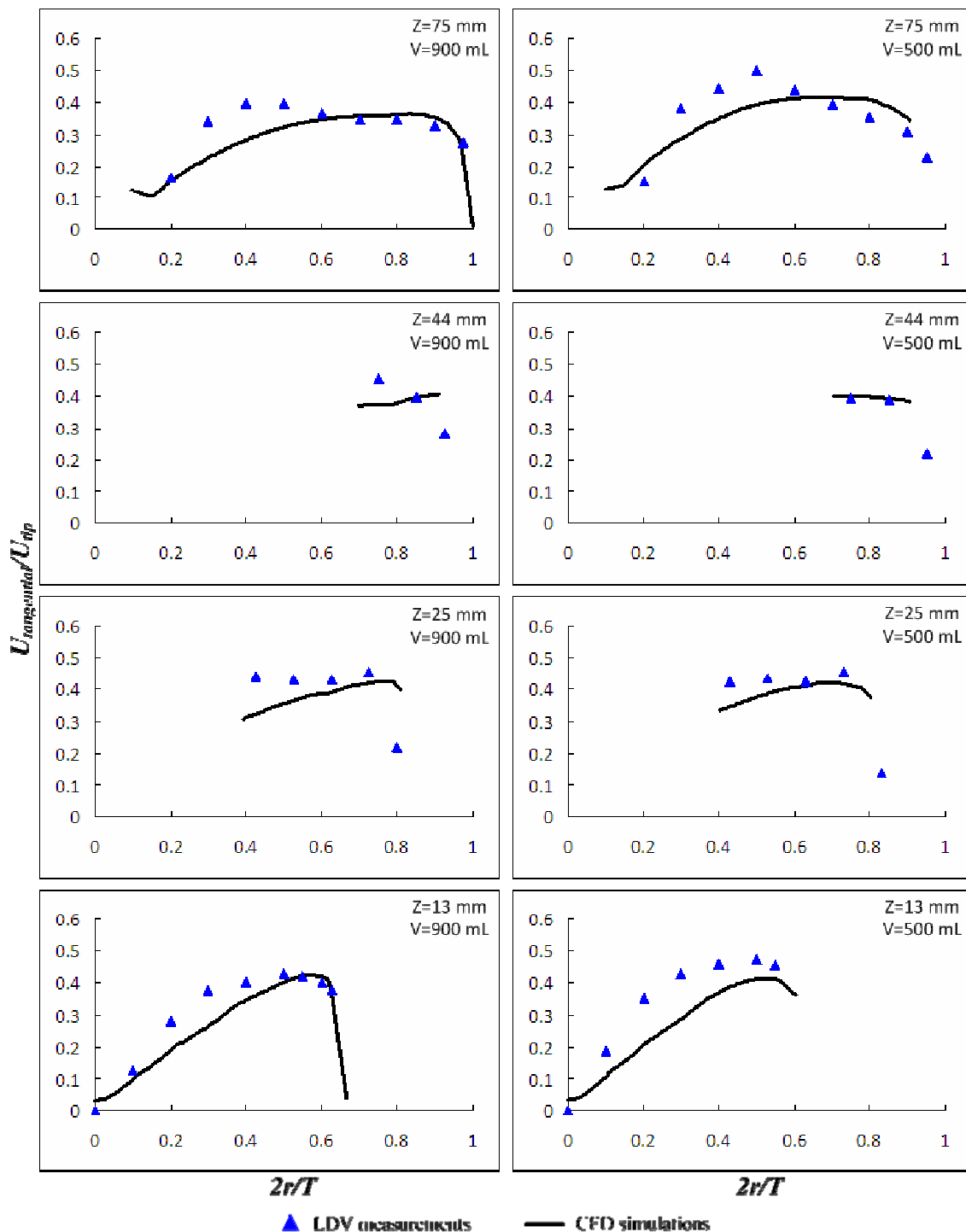
Figure 4.3 Experimentally and computationally determined tangential velocities on four iso-surfaces at an agitation speed of 50 rpm in standard Apparatus 2 with 900 mL (left) and 500 mL (right) water.
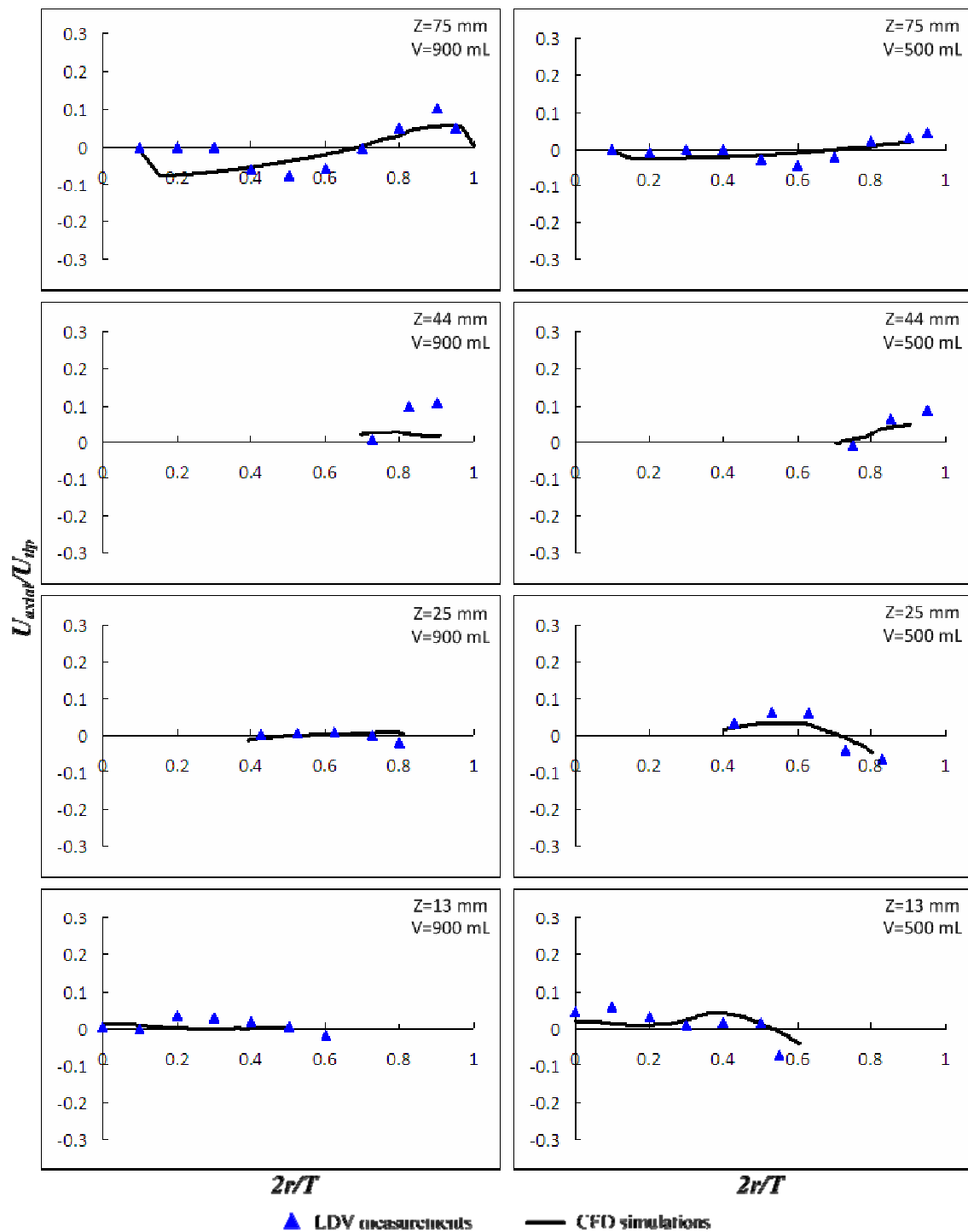
Figure 4.4 Experimentally and computationally determined axial velocities on four iso-surfaces at an agitation speed of 50 rpm in standard Apparatus 2 with 900 mL (left) and 500 mL (right) water.

Figure 4.5 Experimentally and computationally determined radial velocities on four iso-surfaces at an agitation speed of 50 rpm in standard Apparatus 2 with 900 mL (left) and 500 mL (right) water.

4.3.1.2 Modified Apparatus 2.   The k-ε simulations were generally in good agreement with the experimental data (Figures 4.6, 4.7 and 4.8). It is worthy to notice that the axial velocity distributions (Figure 4.7) were larger in the modified Apparatus 2 at iso-surfaces z=25 mm and z=13 mm than that in standard Apparatus 2. On iso-surface z=25 mm, the peak value of axial velocity was about 15% of the tip speed in both the 900 mL and 500 mL systems. In addition, the negative velocity distribution of the axial component indicates that the flow is directed downward, which is expected since this iso-surface (z=25 mm) is at the lower edge of the impeller. The radial velocity distributions (Figure 4.8) on iso-surface z=13 mm in both 900 mL and 500 mL systems are larger than that in standard Apparatus 2. The peak values in 900 mL and 500 mL systems reached 10% and 20% of the tip speed, respectively. The negative radial velocity indicates that the flow directs toward the center of the impeller. Both the larger axial and radial velocities would become the advantages for the modified Apparatus 2 since they can disrupt the solid body rotation in the standard Apparatus 2 and improve the circulation loops in the vessel especially in the bottom region. Larger axial and radial velocities would also be powerful enough to penetrate the inner core region where "coning" effect always occurs.

In general, the CFD predictions were of the same order of magnitudes as the experimental data, indicating that this CFD approach is robust. The simulations based on the k-ε turbulence model were generally in good agreement with LDV measurements. All simulation results present here were obtained using this turbulence model. In the rest of this research work (Chapter 4, Chapter 5 and Chapter 6), all simulations were conducted using the standard k-ε turbulence model.

Figure 4.6 Experimentally and computationally determined tangential velocities on four iso-surfaces at an agitation speed of 50 rpm in modified Apparatus 2 with 900 mL (left) and 500 mL (right) water.

Figure 4.7 Experimentally and computationally determined axial velocities on four iso-surfaces at an agitation speed of 50 rpm in modified Apparatus 2 with 900 mL (left) and 500 mL (right) water.
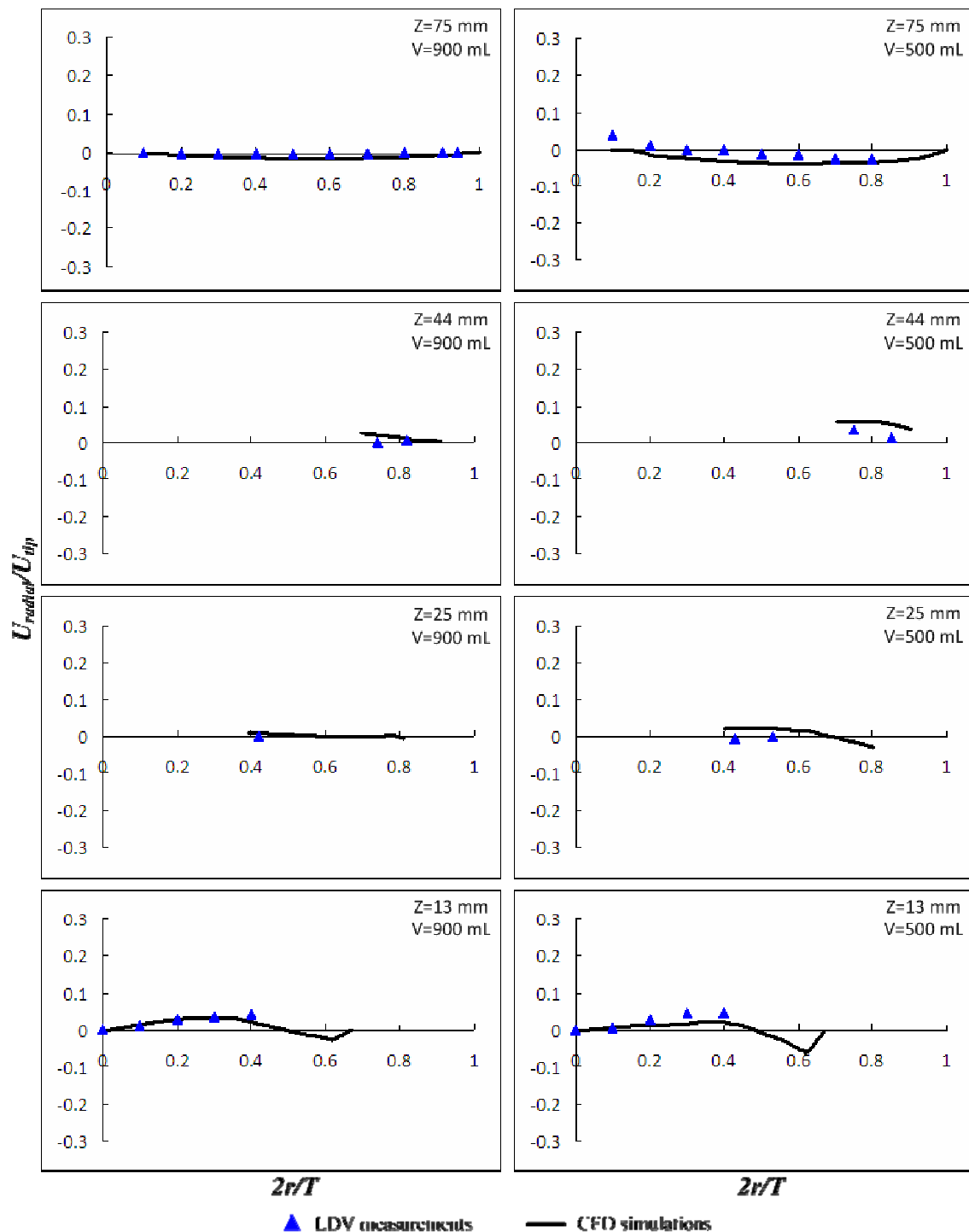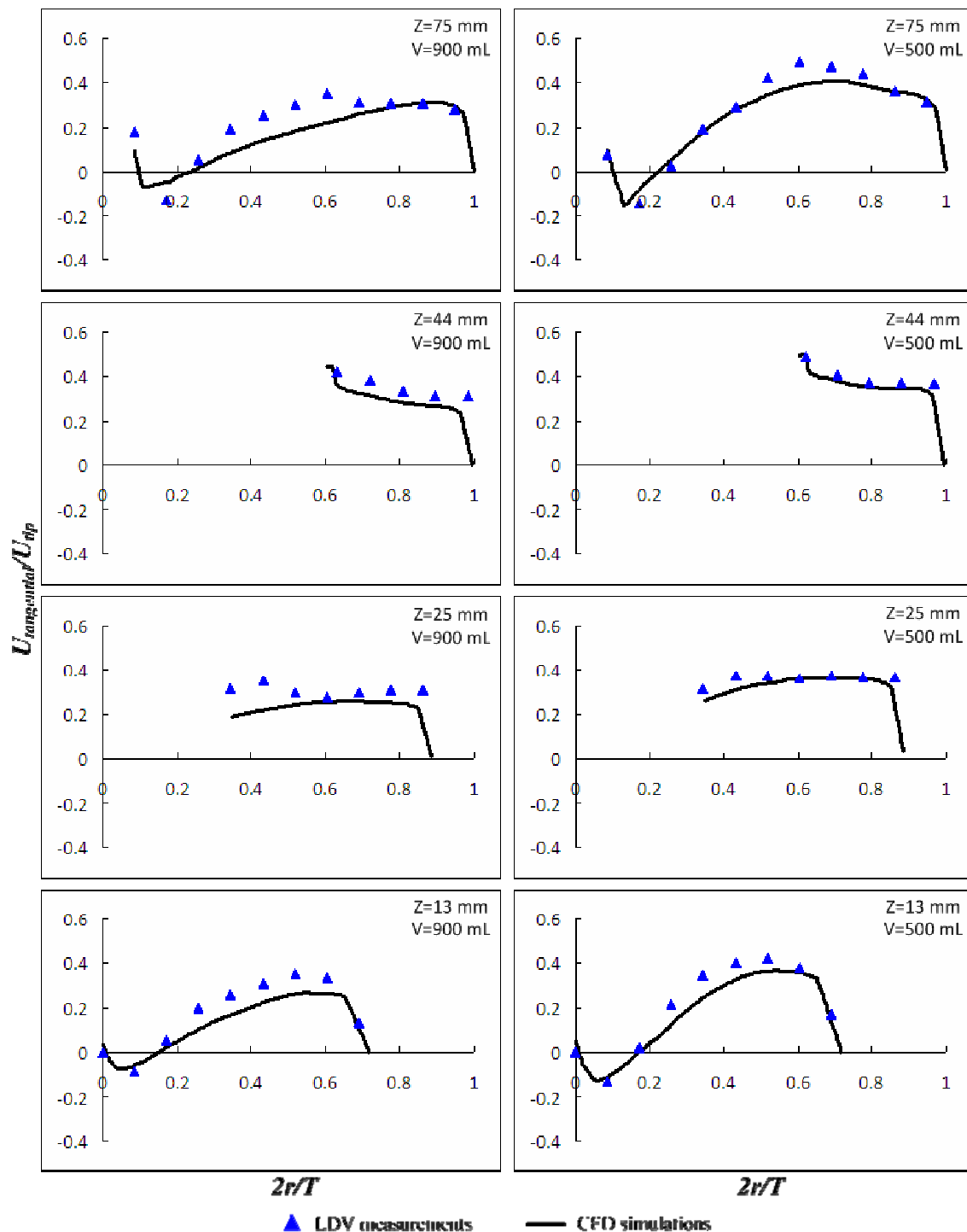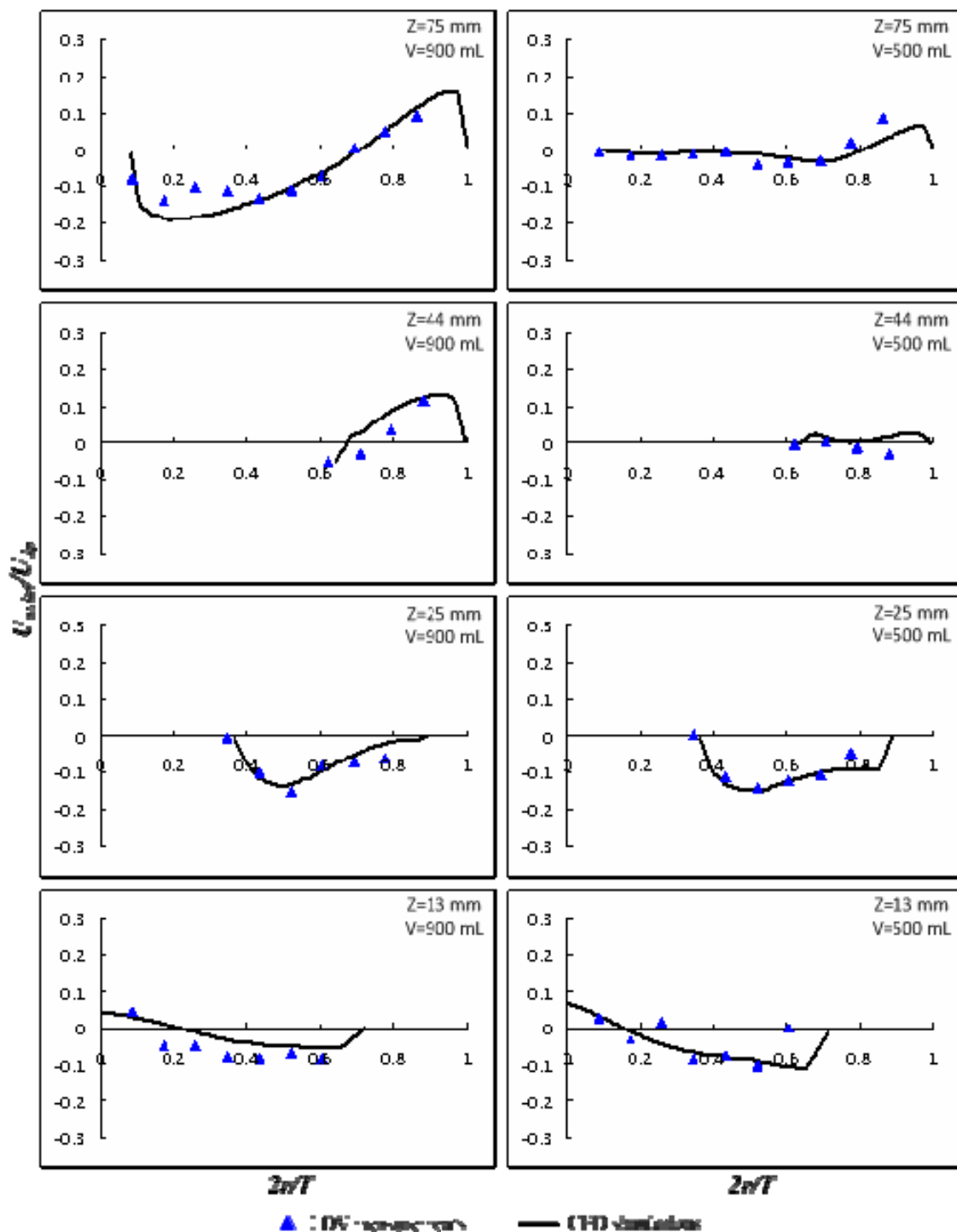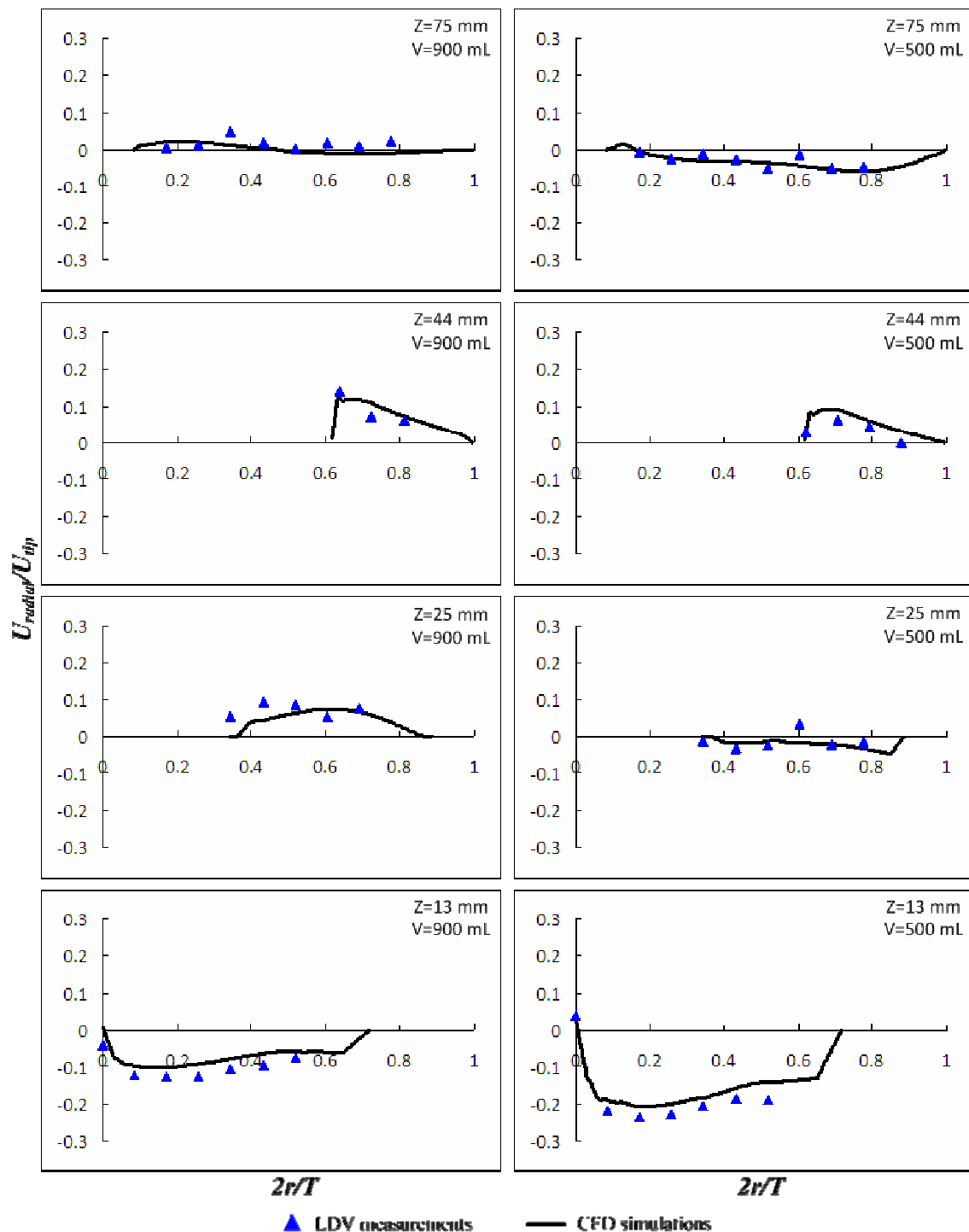
Figure 4.8 Experimentally and computationally determined radial velocities on four iso-surfaces at an agitation speed of 50 rpm in modified Apparatus 2 with 900 mL (left) and 500 mL (right) water.

4.3.2 Velocity Magnitudes

Having validated the CFD velocity predictions with experimental data, it was then possible to use CFD to examine the overall flow patterns generated in Apparatus 2 and modified Apparatus 2. Figures 4.9(a), 4.10(a) and 4.11(a) present the velocity magnitudes in the 900 mL Apparatus 2 generated by the CFD simulations at 50, 75 and 100 rpm impeller agitation speeds, respectively. The corresponding velocity magnitudes in the 900 mL modified Apparatus 2 are shown in Figures 4.9(b), 4.10(b) and 4.11(b). Figures 4.12(a), 4.13(a) and 4.14(a) present the velocity magnitudes in the 500 mL Apparatus 2 at 50, 75 and 100 rpm, respectively. Figures 4.12(b), 4.13(b) and 4.14(b) show the velocity magnitudes in the 500 mL modified Apparatus 2 vessel at 50, 75 and 100 rpm. The color maps in the magnitudes plots are from 0.00 to 0.20 m/s.

4.3.2.1 900 mL Apparatus 2 and Modified Apparatus 2.   In   Figures   4.9(a), 4.10(a) and 4.11(a), the velocity magnitude above the impeller increases significantly with increasing agitation speeds, except in the region near the shaft where the velocity is weaker. However, the velocity magnitude at each point in the vessel is equal to the square root of the sum of the squares of the three velocity components at that point. Therefore, the increase in velocity magnitude with agitation speed can be attributed, to a significant extent, to the corresponding increase in the tangential component, which is the dominating component of the velocity. A similar situation can be observed in the region below the impeller. When the impeller agitation speed is increased, the velocity magnitude increases accordingly. However, in the inner core region below the shaft near the vessel bottom, the velocity is still very low velocity (blue color), even when the agitation speed is increased to 75 rpm or even 100 rpm. That is the region where the

lowest velocity magnitudes in the entire vessel can be found, independently of the agitation speed. However, this is also the region where the tablet is typically located during a test.

In Figures 4.9(b), 4.10(b) and 4.11(b), above the impeller, the velocity magnitude increases significantly with increasing agitation speeds. The velocity distribution in the modified Apparatus 2 vessel is asymmetric. A similar situation can be observed in the region below the impeller. When the impeller agitation speed is increased, the velocity magnitude increases accordingly. However, the velocity distribution becomes much more uniform in the bottom of the modified Apparatus 2 vessel. The inner core region found in Apparatus 2 vessel now shifts to the lower edge of the impeller in the modified Apparatus 2 vessel and the region becomes smaller than that in Apparatus 2 vessel. This change is critical for practical dissolution testing since the poorly mixed region no longer exists at the position where the tablet is typically located during a dissolution test.

(a)   (b)
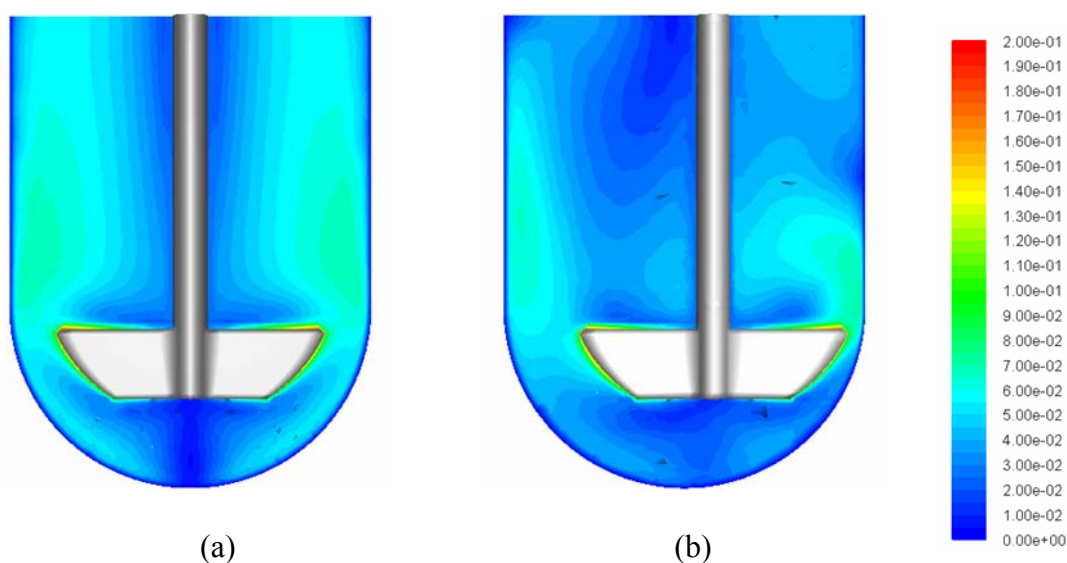
Figure 4.9 Contours of velocity magnitudes at an agitation speed of 50 rpm for (a) standard and (b) modified Apparatus 2 (900 mL water).
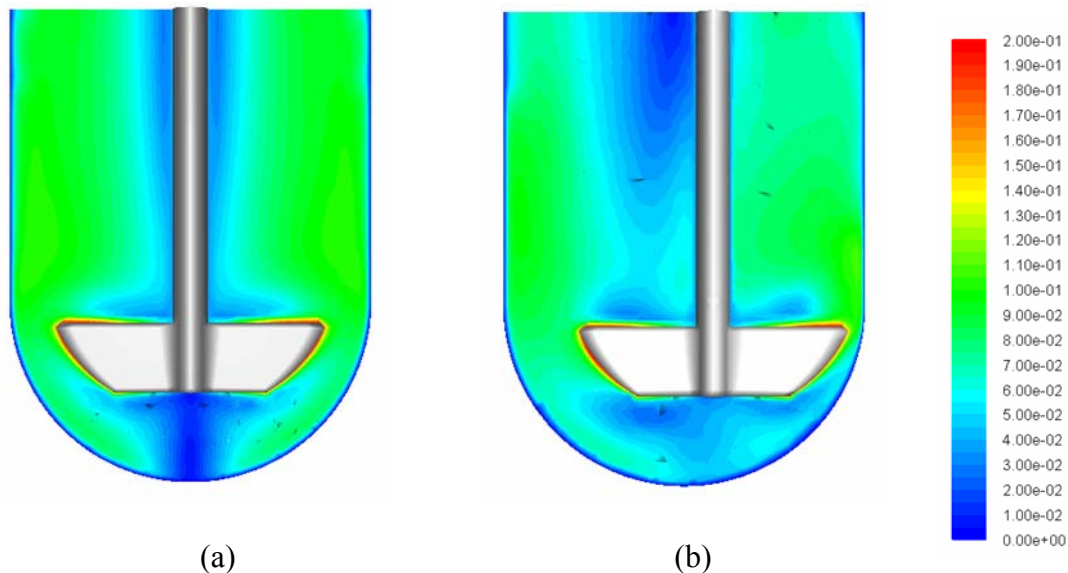
Figure 4.10 Contours of velocity magnitudes at an agitation speed of 75 rpm for (a) standard and (b) modified Apparatus 2 (900 mL water).
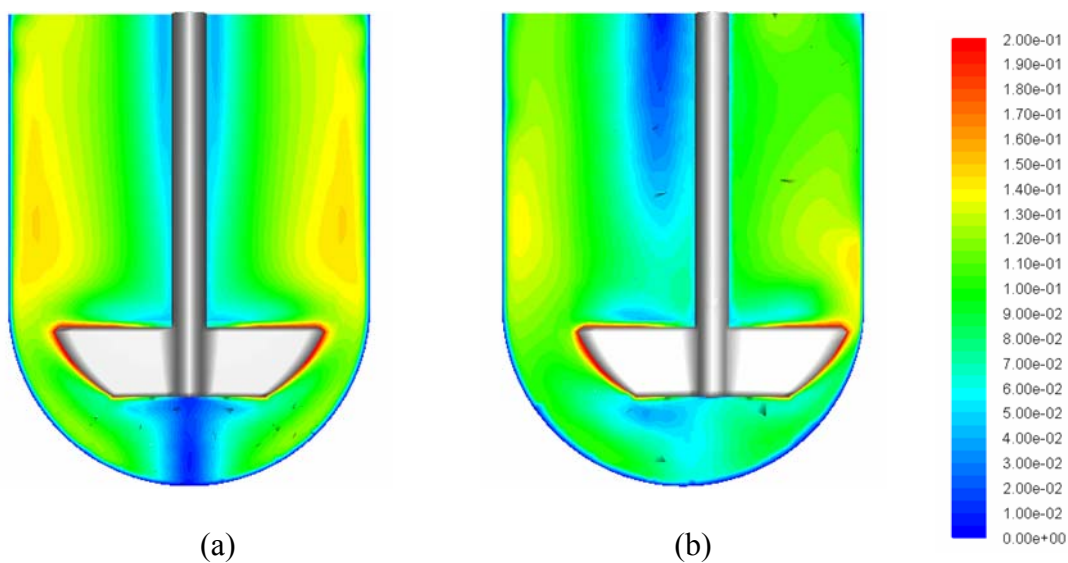
Figure 4.11 Contours of velocity magnitudes at an agitation speed of 100 rpm for (a) standard and (b) modified Apparatus 2 (900 mL water).

4.3.2.2 500 mL Apparatus 2 and Modified Apparatus 2. In Figures 4.12(a), 4.13(a) and 4.14(a), the velocity magnitude above the impeller increases significantly

with increasing agitation speeds. In the region near the shaft, the velocity is still very weak. A similar velocity distribution can be observed in the region below the impeller. However, in the inner core region below the shaft near the vessel bottom, the velocity is still very low (blue color), even when the agitation speed is increased to 75 rpm or even 100 rpm.

In Figures 4.12(b), 4.13(b) and 4.14(b), the velocity distribution in the modified Apparatus 2 vessel is asymmetric. When the impeller agitation speed is increased, the velocity magnitude increases accordingly. However, the velocity distribution becomes much more uniform in the bottom of the modified Apparatus 2 vessel with 500 mL water. The fluid flows have been improved significantly as can be observed from the color distribution, especially in the bottom region. The inner core region found in Apparatus 2 vessel now disappears in the modified Apparatus 2 vessel at 50 rpm and this region becomes smaller than that in Apparatus 2 vessel at 75 and 100 rpm.

(a)   (b)

Figure 4.12 Contours of velocity magnitudes at an agitation speed of 50 rpm for (a) standard and (b) modified Apparatus 2 (500 mL water).

(a)   (b)
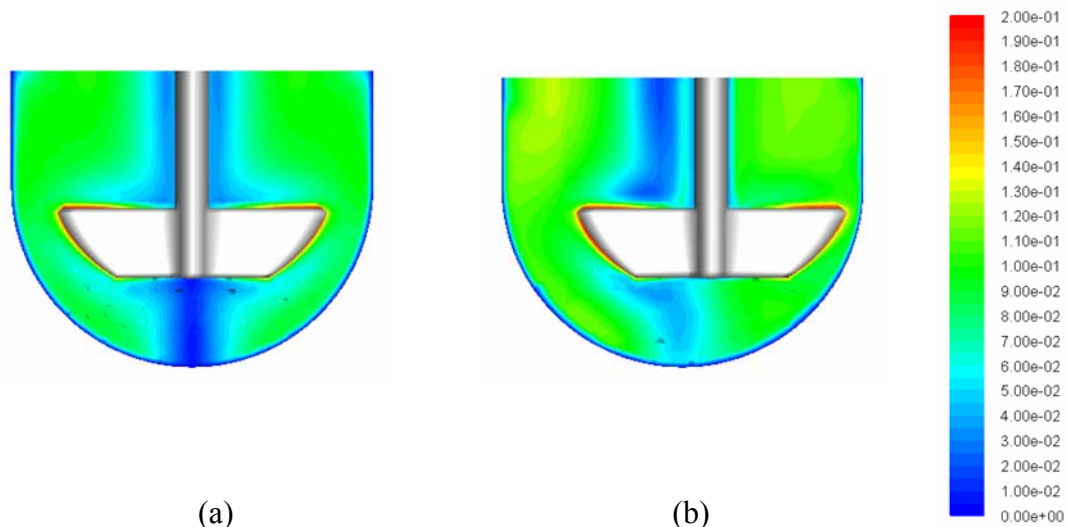
Figure 4.13 Contours of velocity magnitudes at an agitation speed of 75 rpm for (a) standard and (b) modified Apparatus 2 (500 mL water).

(a)   (b)
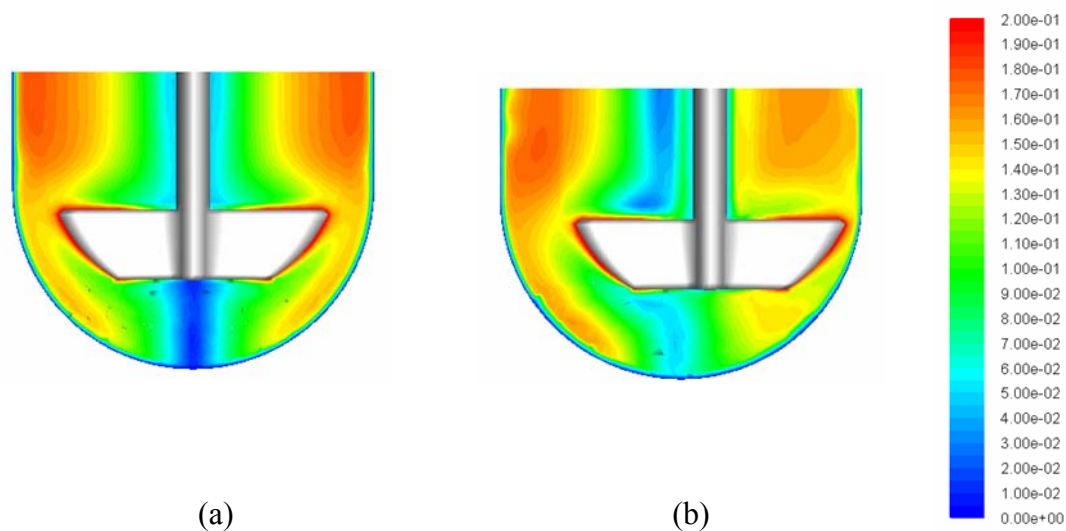
Figure 4.14 Contours of velocity magnitudes at an agitation speed of 100 rpm for (a) standard and (b) modified Apparatus 2 (500 mL water).

In Apparatus 2 with 900 mL, the velocity distributions in the bottom region are extremely low and non-uniform at all agitation rates (50, 75 and 100 rpm). However, when the impeller is shifted 8 mm away from the center of the vessel, the fluid flow in

the bottom region is much more uniform than in Apparatus 2. In the 500-mL system, the same phenomenon is observed.

By comparison, the velocities in the region below the paddle in Apparatus 2 are found to be very low in magnitude. This is the most critical region of Apparatus 2 since the dissolving tablet is likely to be found at this location during the dissolution test. The velocities in this region, although very small, change significantly over short distances along the vessel bottom. This shows that small variations in the location of the tablet on the vessel bottom caused by the randomness of the tablet descent through the liquid are likely to result in significantly different velocities and velocity gradients near the tablet. This is likely to introduce variability in dissolution testing, as it has been confirmed experimentally in controlled dissolution tests where the tablets were placed at different fixed locations (Chapter 3). In the modified Apparatus 2, a much more uniform flow field can be observed. This significant improvement could be an important factor for a much more stable and reliable dissolution testing.

4.3.3 Velocity Vectors

Figures 4.15(a), 4.16(a), 4.17(a), 4.18(a), 4.19(a) and 4.20(a) present the velocity vectors in Apparatus 2 with 900 mL, 500 mL water generated by the CFD simulations at 50, 75 and 100 rpm impeller agitation speeds, respectively. The corresponding velocity vectors in the modified Apparatus 2 with 900 mL and 500 mL water are shown in Figures 4.15(b), 4.16(b), 4.17(b), 4.18(b), 4.19(b) and 4.20(b).

4.3.3.1 900 mL Apparatus 2 and Modified Apparatus 2.   In Figures 4.15(a), 4.16(a) and 4.17(a), the horizontal radial jet generated by the impeller produces weak upward and downward flows once it impacts the vessel wall, forming secondary

recirculation loops above and below the impeller. Above the impeller, the circulation loops are dominated by weak axial velocities for all agitation speeds. The flow pattern below the impeller is the most complex of the entire vessel. Two regions can be identified below the impeller based on the flow patterns associated with them. The first region is the outer region characterized by recirculation loops formed by the downwards flow originating from the radial jets produced by the agitation of the impeller near the vessel wall. The second region is the inner core zone just below the shaft at the center of the vessel bottom. This is the most important region in the dissolution vessel since the dissolving tablet is typically located in this region during most tests. This region is not penetrated by the recirculation loops of the first region, and it is clear that the flow in this central inner core region is very weak, variable, and unstable. Furthermore, this region appears to be a common feature of the flow pattern in the vessel independently of the agitation speeds.

In Figures 4.15(b), 4.16(b) and 4.17(b), there are still horizontal radial jets generated by the impellers, producing upward and downward flows once it impacts the vessel wall, forming secondary recirculation loops above and below the impeller. Above the impeller, the velocity vectors are no longer symmetric. The flow patterns below the impellers become much more uniform and possess obvious flow patterns at different agitation rates although they are not symmetric. It is clear that the inner core found in Apparatus 2 now shift from the bottom of the vessel to the lower edge of the impeller. The recirculation loops formed by the downwards flow originating from the radial jets can penetrate the bottom of the vessel. This is the most important region in the

dissolution vessel since the dissolving tablet is typically located in this region during most tests. It is clear that the flow at the bottom now is much stronger and uniform.

(a)   (b)
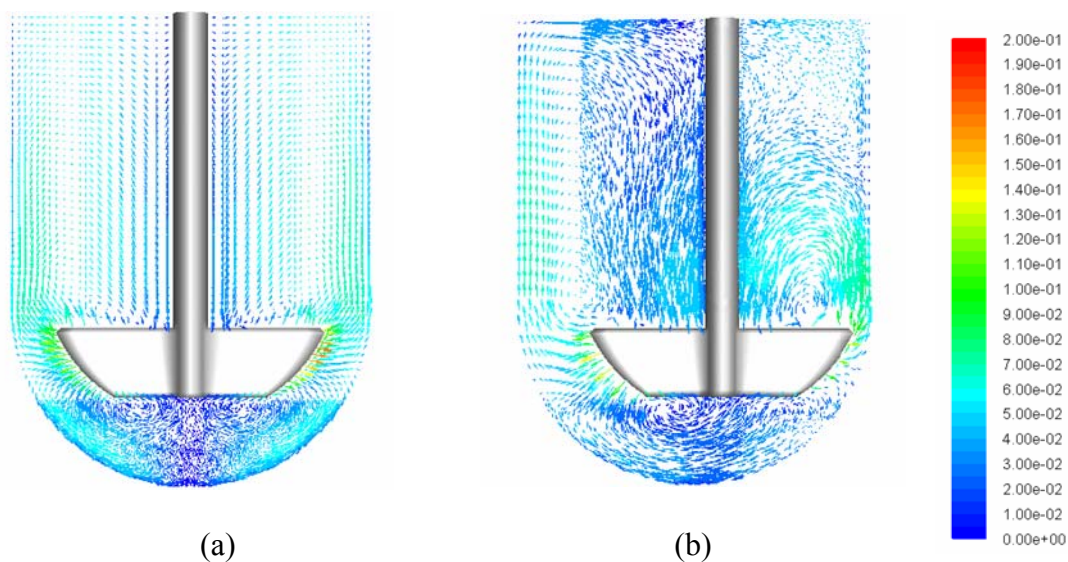
Figure 4.15 Velocity vectors at an agitation speed of 50 rpm for (a) standard and (b) modified Apparatus 2 (900 mL water).

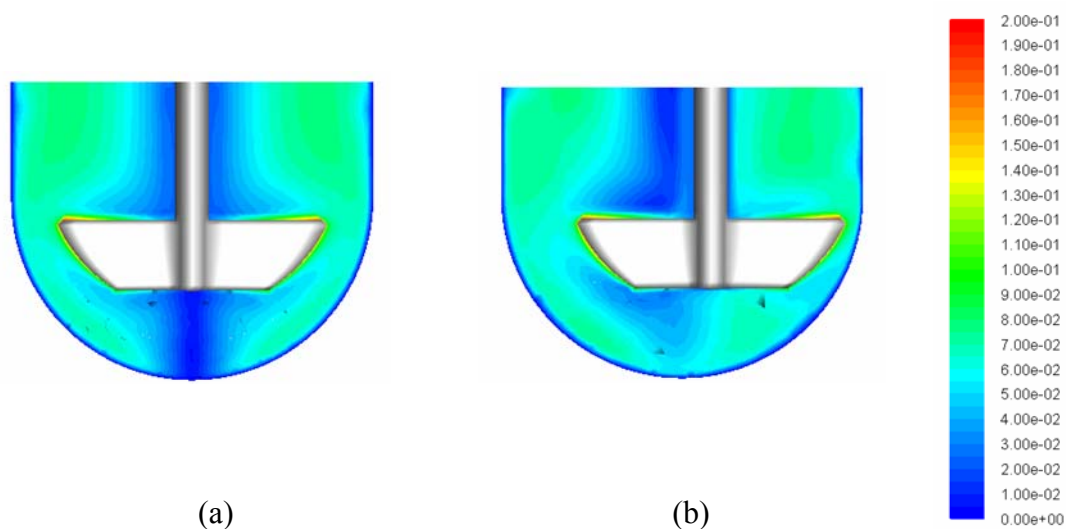(a)   (b)
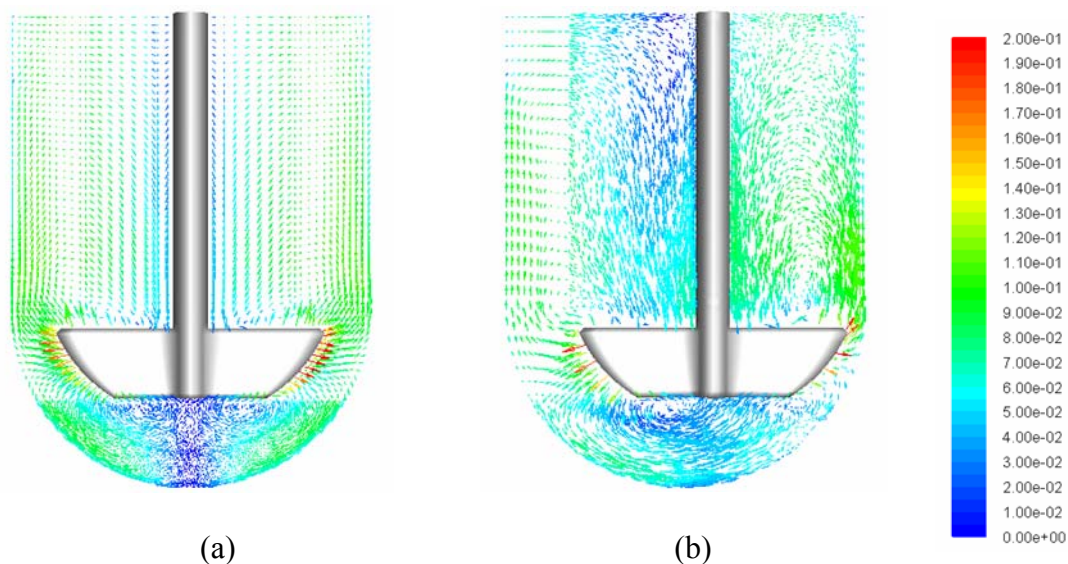
Figure 4.16 Velocity vectors at an agitation speed of 75 rpm for (a) standard and (b) modified Apparatus 2 (900 mL water).

(a)   (b)
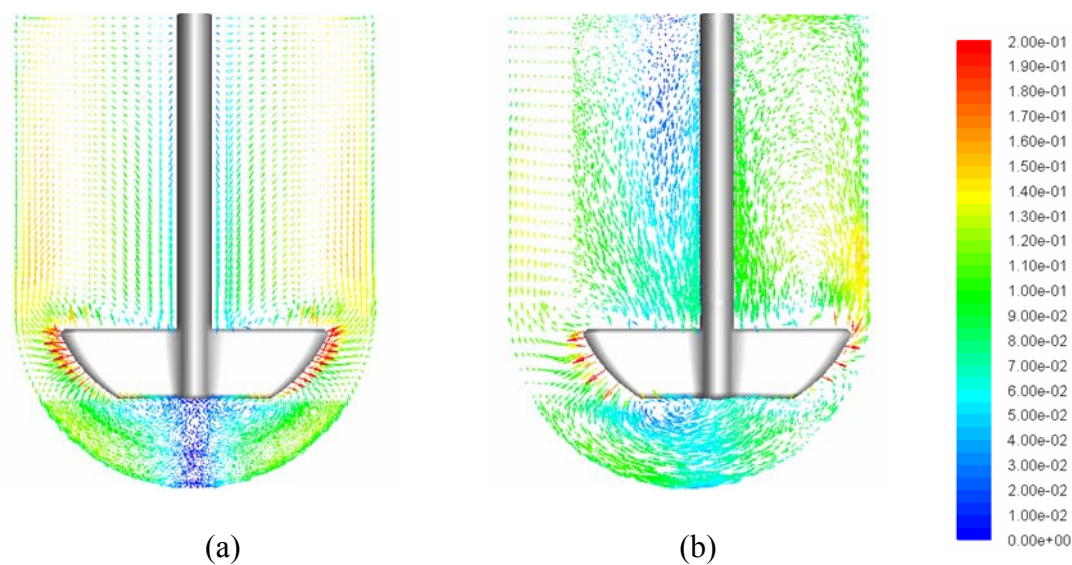
Figure 4.17 Velocity vectors at an agitation speed of 100 rpm for (a) standard and (b) modified Apparatus 2 (900 mL water).

4.3.3.2 500 mL Apparatus 2 and Modified Apparatus 2.   In   Figures   4.18(a),

4.19(a) and 4.20(a), similar velocity vectors in modified Apparatus 2 with 500 mL water

as in the modified Apparatus 2 with 900 mL of water can be observed. Two regions can

be identified below the impeller based on the flow patterns associated with them. The

first region is the outer region formed by the downwards flow originating from the radial

jets near the vessel wall. The second region is the inner core zone just below the shaft at

the center of the vessel bottom.

In Figures 4.18(b), 4.19(b) and 4.20(b), the velocity vectors in the entire vessel

are no longer symmetric. The flow patterns below the impellers become much more

uniform at all agitation rates. The recirculation loops formed by the downwards flow

originating from the radial jets can penetrate the bottom of the vessel.
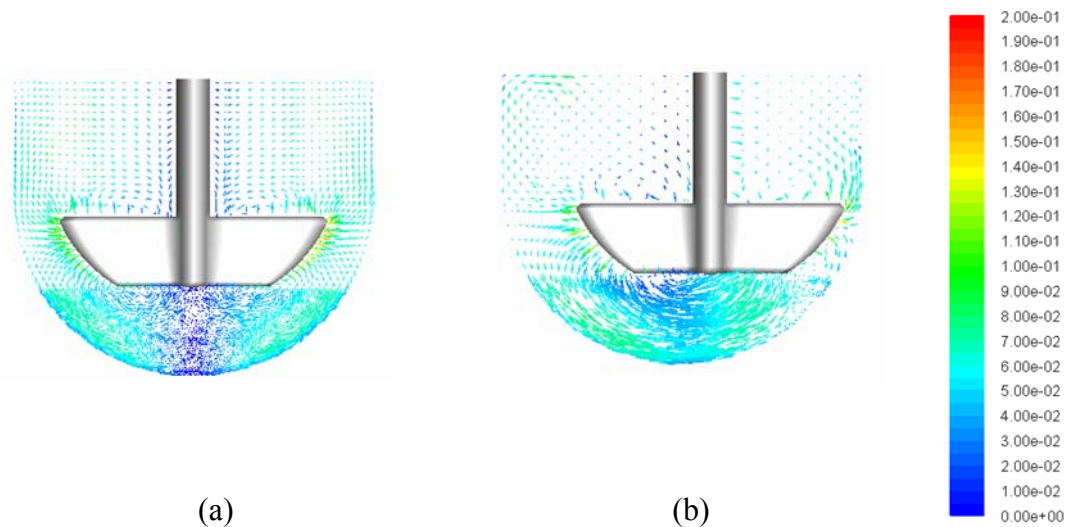
Figure 4.18 Velocity vectors at an agitation speed of 50 rpm for (a) standard and (b) modified Apparatus 2 (500 mL water).
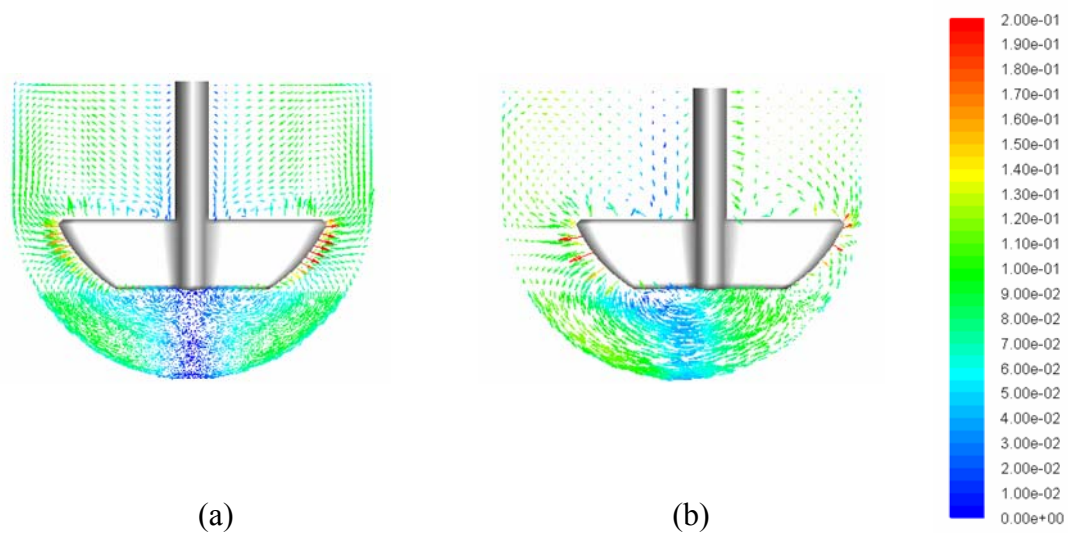
Figure 4.19 Velocity vectors at an agitation speed of 75 rpm for (a) standard and (b) modified Apparatus 2 (500 mL water).

(a)   (b)
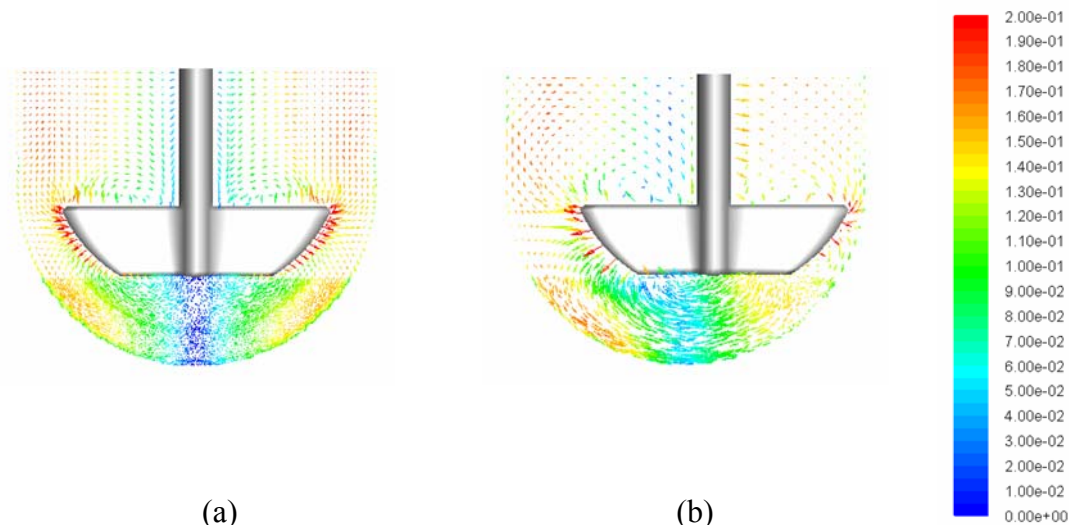
Figure 4.20 Velocity vectors at an agitation speed of 100 rpm for (a) standard and (b) modified Apparatus 2 (500 mL water).

In Apparatus 2, the lowest region just below the shaft is characterized by extremely low velocity vectors, which do not have obvious flow patterns. These small and random velocity vectors could be the most suspicious reason for the instability during dissolution tests. However, when the impeller is placed 8 mm away from the vessel center, the velocity vectors are greatly improved in the bottom of the vessel. Vectors become bigger and possess an obvious flow pattern near the vessel bottom. The flow field in the modified system is much homogeneous than in Apparatus 2. Now the fluid can access easily the bottom of the vessel, where tablet is usually located, and improve the mass transfer process during dissolution testing.

4.4   Conclusions

The fluid velocity profiles at different locations inside Apparatus 2 and the modified Apparatus 2 were computationally obtained via Computational Fluid Dynamics (CFD) at three impeller agitations speeds, namely 50 rpm, 75rpm and 100 rpm. The predictions

obtained with CFD, where k-ε model was used to account for turbulence effects, were validated with the experimental results. In general, good agreement was found between the experimental velocity measurements and the CFD simulation predictions. The CFD predictions in the modified Apparatus 2 show that the velocity profiles and flow pattern are significantly improved. The flow field in the modified Apparatus 2 are now much more homogeneous than that in Apparatus 2, especially in the bottom region. The inner core region just below the impeller, where the dissolving tablet is usually located, does not exist in the modified Apparatus 2. In the modified Apparatus 2, both the velocity vectors and velocity magnitudes show that the flow inside the vessel, and especially near the bottom, is stronger and more homogenous and this is likely to result in more reproducible dissolution profiles that are insensitive to the position change of the impeller.

CHAPTER 5

POWER CONSUMPTION AND MASS TRANSFER COEFFICIENT IN USP APPARATUS 2

5.1 Power Number Theory

The mechanical energy dissipated per unit time in a stirred vessel, i.e., the power, *P*, dissipated by an impeller mounted on a vertical shaft and rotating in a viscid liquid at a rotational speed *N*, is given by:

$$P = \omega \cdot \tau = 2\pi N \tau \tag{5.1}$$

where ω is the angular velocity of the impeller and τ is the torque required to rotate the impeller. This equation can be used to obtain experimentally the power dissipated by any impeller, if the agitation speed and the torque at the shaft can be measured simultaneously. In previous investigations with a variety of mixing systems, the value of the power dissipation has often been obtained experimentally using this approach [43, 44, 45, 46, 47, 48, 49, 50, 51].

All physical variables (such as the density and viscosity of the fluid), dynamic variables (such as the agitation speed), and geometric variables (such as shapes and sizes of the impeller and the vessel, extent of baffling, impeller off-bottom clearance, liquid height, and all other relevant geometric characteristics of the system) can in principle affect the power dissipation in mixing systems and can produce different flow patterns in the fluid being mixed. In order to reduce the number of variables to be studied, non-dimensional analysis has been typically used [45, 46, 47, 52, 53], resulting in an equation

for P where the non-dimensional power number Po (defined as $Po{\equiv}P/{\rho}N^3D^5$) is expressed as a function of several non-dimensional groups, i.e.:

$$Po \equiv \frac{P}{\rho N^3 D^5} = f\left(\frac{\rho ND^2}{\mu}, \frac{N^2 D}{g}, \frac{H}{T}, \frac{T}{D}, \frac{C}{T}, impeller\ type, vessel\ type, baffling\ type\right) \quad (5.2)$$

In this equation, Po is the power dissipated by the impeller made non-dimensional by dividing it by the appropriate physical, dynamic and geometric variables. The first of the non-dimensional groups in parenthesis is the impeller Reynolds number, $Re= \rho ND^2/\mu$, the second group is the Froude number, $Fr=N\ D^2/g$, and the other groups are geometric ratios, including the last one, which depends on what type of vertical baffles are present in the system, if any.

For the case of USP apparatus 2, the vessel size and shape are fixed, and the vessel is unbaffled. The size and shape of the impeller are also standardized (thus also determining the D/T ratio), and so is it impeller clearance off the vessel bottom (and hence C/T). In addition, since the air-liquid level is typically flat or nearly flat in USP apparatus 2 vessel because of the relatively low agitation speeds at which dissolution tests are carried out (less than 200 rpm, and typically in the 50-100 rpm range), the role of gravity forces can be ignored, and the Froude number becomes unimportant. Therefore, Po in Equation 5.2 can be expected to be only a function of Re and the H/T ratio. In the literature on power dissipation in mixing vessels, Po has typically been plotted as a function of Re (usually on a log-log scale), whereas other geometric ratios such as C/T and H/T were used as parameters [53]. Po has been shown to become a

constant for any given geometric configuration and for geometrically similar systems, irrespective of scale, provided that the tank is fully baffled (typically with four wall baffles) and the flow is fully turbulent (i.e., $Re>10^4$) [45, 46, 47, 48, 49, 50, 51]. For unbaffled systems, the power number has been shown to decrease slightly with Re, even in the fully turbulent regime.

When this analysis is applied to USP apparatus 2 vessel, Po can be expected to be a function of Re only, for any given H/T value, although the Po-vs.-Re curve can be different for different values of the H/T ratio. In other words, it should be possible to describe the functionality of the power number in the USP apparatus 2 system as:

$$Po = f\left(\mathrm{Re}\right) \quad \textit{for } H/T = \mathrm{constant} \tag{5.3}$$

The exact type of functionality and the final equation for Po can be obtained by inspecting the experimental data, propose an appropriate function for $f(\mathrm{Re})$, such as a power-law equation [54, 55], and curve fitting the experimental data to determine the equation constants.

Computational Fluid Dynamics (CFD) is a tool, which has the ability to deliver basic fluid dynamic information inside the stirred vessels. The main advantage of this approach is in its potential for reducing the extent and number of experiments required to describe such types of flow. However, validation of CFD as a predictive tool requires comparison of the numerical results with experimental velocity data. Most of the CFD work carried out to date, as far as flow in mixing vessels is concerned, has been focused on applications dealing with baffled vessels [56, 57, 58, 59]. Unbaffled vessels are

nevertheless important both from a fundamental and an industrial point of view. In recent years a few studies have been focused on such systems [60, 61]. The absence of baffles in a vessel typically results in the generation of a central vortex and a swirling flow [62]. If the vessel is operated at a quite low agitation speed, no vortex can be observed. This simplifies the mathematical simulation of flow in unbaffled systems (because of the absence of the air-liquid interface), while still retaining the complexity of the tangentially dominated flow [60, 61].

5.2   Mass Transfer Coefficient

A fundamental understanding of how the drug particles and hydrodynamics are combined to impact the drug release profile still needs to be explored in greater detail. For example, in the Noyes-Whitney equation,

$$\frac{dC}{dt} = k_{SL} \frac{A}{V} (C^* - C) \tag{5.4}$$

the dependence of mass transfer coefficient k_{SL} on drug particle size and power dissipated have never been investigated quantitatively in USP Apparatus 2. Many dissolution models assume k_{SL} to be a constant, which is convenient. However, it is obvious that k_{SL} is altered by the hydrodynamics.

Knowledge of particle-liquid mass transfer coefficient k_{SL} is important for USP dissolution testing not only for quality control, but also for the *in vivo* predictions of the release profile. The effect on system configurations, operation parameters (impeller speed/power input) and physical properties (drug particle size after disintegrating, density

difference) on k_{SL} can have a significant impact on the dissolution process in USP Apparatus 2.

Studies on particle-liquid mass transfer were conducted in stirred vessels have been conducted previously and their results are available in the literature. Hixson and Crowell [63] observed an increase of k_{SL} with an increase in the impeller speeds. Mack and Marriner [64] found that k_{SL} can be correlated in terms of Sherwood number based on vessel diameter with impeller power number and impeller Reynolds number. Armenante and Kirwan [65] found that the mass transfer coefficient for microparticles can be correlated by Equation 5.5, which also correlates the reliable results on microparticles in the literature.

One of the fundamental issues in modeling and understanding dissolution is to determine the relationship between the mass transfer coefficient and particle size under a defined set of hydrodynamic conditions. The mass transfer coefficient dependence on dissolution hydrodynamics has received very little consideration. Therefore, the examination of mass transfer coefficient dependence on particle size and the system's hydrodynamics is theoretically and practically significant. In this chapter, the equations for mass transfer coefficient (Equations 5.5 and 5.6) are as follows [**65**]:

$$Sh = 2 + 0.52(\text{Re})^{0.52}(Sc)^{1/3} \tag{5.5}$$

$$Sh = \frac{k_{SL}d_p}{D_{AB}} \tag{5.6}$$

where the Reynolds number and Schmidt number are given in Equations 5.7 and 5.8, respectively.

$$\text{Re} = \frac{\varepsilon^{1/3} d_p^{4/3}}{v} = \frac{\left(\dfrac{P}{\rho V}\right)^{1/3} d_p^{4/3}}{v} \tag{5.7}$$

$$Sc = \frac{v}{D_{AB}} \tag{5.8}$$

where ε is the energy dissipation rate at a certain agitation speed; d_p is the particle size during dissolution testing; v is the kinematic viscosity of the solution; P is the power dissipated in USP apparatus 2 at a certain agitation speed; ρ is the solid oral dosage form density; V is the volume of medium; D_{AB} is the mass diffusivity between species A and B.

Several assumptions of the dissolution process in USP apparatus 2 used in this chapter are:

1. Drug fragments are spherical particles after disintegration.
2. Drug fragments are fully suspended.

The property of the drug used in this part is based on particle suspension spectrum in USP apparatus 2 with 900 mL water (Appendix B). This spectrum is obtained computationally by Discrete Phase Model in FLUENT.

5.3   Experimental Apparatus and Method

A sensitive torque measurement apparatus is specifically built to measure the small torque applied to the liquid in Apparatus 2 and modified Apparatus 2 when stirred by a USP 2 paddle. A schematic of the basic experimental setup is shown in Figure 5.1. The apparatus is built as follows.

One end of a thin nylon line is permanently glued to the center of a shallow plastic tank 15 cm in side and 4 cm in depth. Separately, a small hole is drilled in the center of a square platform made of a polystyrene foam slab, 10 cm in side and 3 cm thick. The nylon line is passed through this hole, the platform is placed in the shallow tank, and the nylon line is pulled until only about 1 cm of the nylon line separated the bottom of platform from the inside bottom of the tank. The nylon line is then permanently glued to the top of the platform. The shallow tank is then filled with water so that the platform would be floating in the tank while being anchored to the shallow tank bottom by the nylon line, now under tension. A standard USP 2 dissolution vessel is placed on a round vessel holder so that the vessel would be able to stand upright. The vessel and the holder are placed in the middle of the floating platform, and the USP 2 vessel is filled with the desired amount of water. More water is poured in the shallow tank so that the platform is nearly but not entirely submerged, in order to create the maximum buoyancy effect. Small weights are applied to the platform to make sure that it is horizontal. The nylon line is still under tension since the weight of the USP 2 vessel and the water in it is much smaller that the Archimedes force resulting from the nearly completely submerged platform. This entire assembly is placed on a traversing system can could move both horizontally and vertically, which is in turn placed under a stand supporting a 1/4-HP, variable-speed, electric motor (Chemglass, Vineland, NJ) with a maximum rotational speed of 500 rpm, driving a shaft connected via a rigid coupling to a standard USP 2 paddle (Figure 5.1). The dimensions of the paddle had been previously measured with a caliper and had been found to be as in Table 2.1, Chapter 2. The traversing system is used to position the floating USP 2 vessel assembly under the motor

so that the impeller is centered in the vessel and the clearance of the paddle off the USP 2 vessel bottom is 25.00 mm, as specified in the USP [1].

(a)

(b)
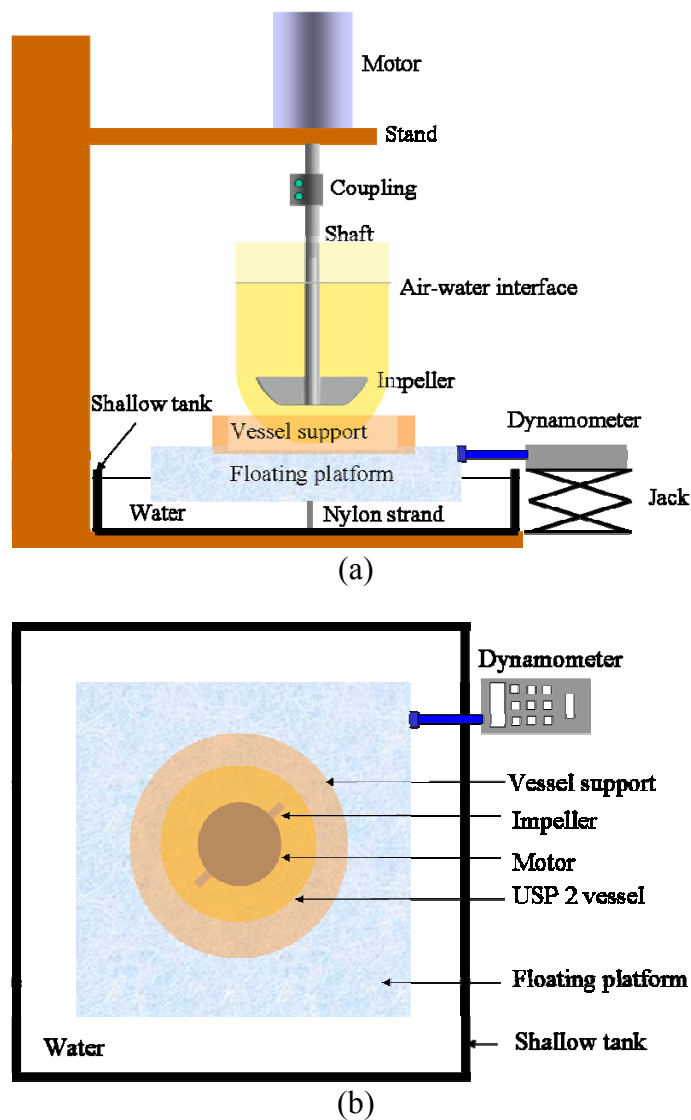
Figure 5.1 Schematic diagram of power measurement setup: (a) front view; (b) top view.

When the impeller is rotated in a clockwise direction (when observed from the top) the floating assembly tended to rotate in the same direction as a result. Therefore, a digital dynamometer, i.e., a force gauge device capable of measuring both tensile and compression force (Nidec-Shimpo America Corp., Itasca, IL; Model EW-93951-31

distributed by Cole-Parmer, Vernon Hills, IL), is mounted horizontally on a laboratory jack next to the floating platform, as shown in Figure 5.1 to prevent the rotation of the platform. The dynamometer has a maximum capacity of 2 N, an accuracy of 0.004 N, and is fitted with an extension rod whose tip rested at a precise location on the platform side. The torque generated by the impeller rotating in the liquid results in a tangential force (with respect to the center of rotation of the floating assembly) which push on the rod tip but is offset by the counter resisting force exerted on, as well as measured by, the fixed dynamometer.

It should be remarked that since water is Newtonian fluid, it cannot produce a shear stress without moving. Therefore, under the static situation occurring in the system, where the dynamometer prevents the floating vessel assembly from turning while the impeller is rotating, no friction is introduced in the force measurement by the water in the shallow tank. Therefore, the torque experienced by the USP 2 vessel and the power dissipated in the liquid can be measured reliably. This makes the system especially appropriate to measure small power dissipations, as in the case of USP dissolution apparatus 2.

A computer connected to the dynamometer is used for data acquisition and data analysis. The sampling frequency is 1000 Hz. By knowing the distance L, i.e., the length of the segment perpendicular to extension rod and passing through the center of rotation of the floating assembly (Figure 5.1), as well as the force applied at that point, the torque could be calculated from:

$$\tau = L \cdot F \sin 90^o = L \cdot F \qquad\qquad (5.9)$$

The impeller rotational speed is measured using a digital tachometer with a photoelectric pick-up sensor (Distek, North Brunswick, NJ), accurate within ±1 rpm. The power dissipated by the impeller rotating in the liquid is calculated using Equation 5.1.

A typical experiment consisted of filling up the vessel with the desired volume of water (either 900 mL or 500 mL), exactly positioning the system and checking the horizontality of the platform and verticality of the USP apparatus 2 vessel, zeroing the dynamometer, turning on the motor and setting it up at the desired agitation speed (between 50 and 200 rpm), waiting 1-2 minutes for the system to equilibrate, and then measuring and recording the force applied to the dynamometer for a period of 60 seconds. All experiments are conducted at room temperature (22°C) and are repeated at least five times.

5.4   CFD Simulations

A commercial CFD software package (FLUENT, 6.3.26; GAMBIT, 2.4.6) is used to predict the power number inside Apparatus 2 and modified Apparatus 2. In addition, the pressure distribution on the surface of the impeller blades from which the torque applied to the impeller and hence the power dissipation were numerically calculated. The standard k-ε model is used to account for turbulence effects. Simulations are carried out for five agitation speeds (50, 75, 100, 150 and 200 rpm). Multiple reference frames (MRF) approach is used to obtain the initial solution of impeller-baffle interaction and sliding mesh is used for a final solution convergence.

The computational domain representing the USP 2 system is divided into two non-overlapping regions, one surrounding the impeller (inner core region) and the other

representing the rest of the vessel (outer region). In the computations, the impeller region is stationary, but within it, the conservation equations are solved in a rotating frame. Therefore, the rotation angular velocity of this region is the same as that of the impellers and shaft and no angular velocity is applied to the shaft or impeller blades, since the velocity of these elements is zero relative to the impeller frame. The second outer region is associated with the outside walls of the apparatus. The conservation equations in this grid region are solved in the stationary frame of the vessel itself and no motion is applied to the vessel wall. The MRF approach relies on the initial simulation of the flow in the inner domain. At the boundary between the two subdomains, the governing equations in the outer subdomain require values for the velocities in the adjacent inner subdomain. Therefore, at this interface the velocities and velocity gradients are converted from a moving reference frame to the absolute inertial frame and used as boundary conditions for the computation in the vessel reference frame. This implies that the continuity of the absolute velocity is applied to provide the correct neighbor values of velocity for the subdomain under consideration. Thus, values of the conserved quantities are matched at the interface between the two grid regions. This procedure is repeated until numerical convergence was achieved.

Since it has been previously reported [66], as well as experimentally observed in this work, that the air-water interface remained nearly flat even at the highest agitation speed, no second gas zone added at the free surface in the simulations. Instead, this interface is treated as a frictionless surface, where the normal gradients of all variables were zero.

All simulations are carried on the mainframe computer at the NJIT High Performance Computing. The simulations are deemed to have converged when residuals fell below 10^{-4}.

The prediction of the power dissipated by the impeller requires calculating the torque acting on the impeller blades using Equation 5.1.

To do so, the pressure distribution on the back and front surfaces of the impeller blades is obtained from the CFD simulations. Considering an infinitesimal surface area $dA=dx{\cdot}dy$ at a generic x-y location on the surface of the impeller blade where the pressure is $p(x,y)$, the infinitesimal torque applied to the impeller by the resulting pressure-generated force is:

$$d\tau = x \cdot p(x,y)\, dx\, dy \tag{5.10}$$

where x is horizontal distance from the centerline of the impeller shaft and y is the vertical coordinate. Then, the calculated power dissipation is given by:

$$P = 2\pi N \left[\iint_{A_{Front}} x \cdot p(x,y)\, dx\, dy - \iint_{A_{Back}} x \cdot p(x,y)\, dx\, dy \right] \tag{5.11}$$

where A_{Front} and A_{back} are the surface areas of the front and the back of the impeller blades. This approach is used to predict the dissipated power using the CFD-generated pressure data.

An additional method to calculate the power dissipated in the system is to obtain the distribution of the local energy dissipation rate per unit mass in USP apparatus 2 vessel, $\varepsilon(x,y,z)$, from the CFD simulation, and then integrate this variable over the entire volume of the vessel, i.e.:

$$P = \rho \iiint_{\substack{Vessel \\ Volume}} \varepsilon(x,y,z)\,dx\,dy\,dz \qquad (5.12)$$

5.5   Results and Discussions

Tables 5.1-5.4 present the power dissipation and power number as a function of agitation speed for Apparatus 2 with 900 mL water, Apparatus 2 with 500 mL water, modified Apparatus 2 with 900 mL water and modified Apparatus 2 with 500 mL water, respectively. The power dissipations are measured from experimental method. Power numbers are calculated via both experiments and simulations. The simulated power numbers are predicted based on two ways. One is based on the torque applied on the impeller blades; the other one is based on the energy dissipation rate, ε, throughout the whole vessel.

Table 5.1 Power Dissipation and Power Number as a Function of Agitation Speeds for Standard Apparatus 2 (900 mL Water)

N (rpm)	P (W)	Re	Po (Experimental)	Po (Predicted – Based on Torque Calculation)	Po (Predicted – Based on ε Integration)
50	0.00045	4939	0.35	0.35	0.38
75	0.00115	7409	0.27	0.33	0.31
100	0.00264	9879	0.26	0.31	0.28
150	0.00870	14817	0.25	0.29	0.26
200	0.01939	19758	0.24	0.28	0.25

Table 5.2 Power Dissipation and Power Number as a Function of Agitation Speeds for Standard Apparatus 2 (500 mL Water)

N (rpm)	P (W)	Re	Po (Experimental)	Po (Predicted – Based on Torque Calculation)	Po (Predicted – Based on ε Integration)
50	0.00049	4939	0.38	0.38	0.29
75	0.00142	7409	0.33	0.26	0.24
100	0.00295	9879	0.29	0.24	0.21
150	0.00852	14817	0.25	0.23	0.20
200	0.01661	19758	0.20	0.22	0.19

Table 5.3 Power Dissipation and Power Number as a Function of Agitation Speeds for Modified Apparatus 2 (900 mL Water)

N (rpm)	P (W)	Re	Po (Experimental)	Po (Predicted – Based on Torque Calculation)	Po (Predicted – Based on ε Integration)
50	0.00075	4939	0.59	0.66	0.67
75	0.00256	7409	0.59	0.66	0.66
100	0.00573	9879	0.56	0.65	0.65
150	0.01729	14817	0.50	0.65	0.64
200	0.03812	19758	0.46	0.65	0.64

Table 5.4 Power Dissipation and Power Number as a Function of Agitation Speeds for Modified Apparatus 2 (500 mL Water)

N (rpm)	P (W)	Re	Po (Experimental)	Po (Predicted – Based on Torque Calculation)	Po (Predicted – Based on ε Integration)
50	0.00066	4939	0.51	0.52	0.52
75	0.00210	7409	0.48	0.50	0.48
100	0.00404	9879	0.39	0.44	0.46
150	0.01247	14817	0.36	0.48	0.44
200	0.02764	19758	0.34	0.48	0.43

5.5.1 Power Consumption

Figure 5.2 and Tables 5.1, 5.2 present the experimentally obtained power consumption as a function of agitation speed for two liquid volumes (900 mL and 500 mL) in Apparatus 2. In the vessel filled with 900 mL water (Figure 5.2 (a)), the power dissipated at 50 rpm

is extremely small (0.00045 Watts). However, power dissipated, P, increases rapidly with agitation rate, N, reaching a value at N=200 rpm, 43 times larger than at N=50 rpm. At 200 rpm, the experimental results show a larger standard deviation than at lower speeds. This figure also reports the corresponding CFD predictions for P. In general, the power dissipation from experiments and simulations are in agreement with each other. The corresponding data for the 500 mL volume are shown in Figure 5.2 (b) and Table 5.2. The agreement between predictions and data is good for this case and a similar trend for P vs. N can be observed. In general, the power dissipation does not change too significantly with liquid volume.
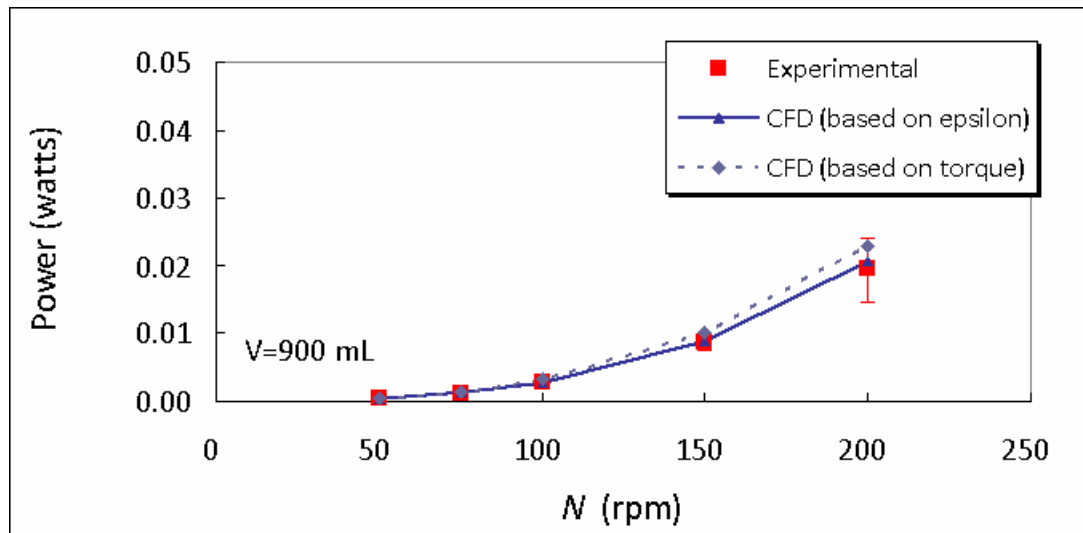
(a)
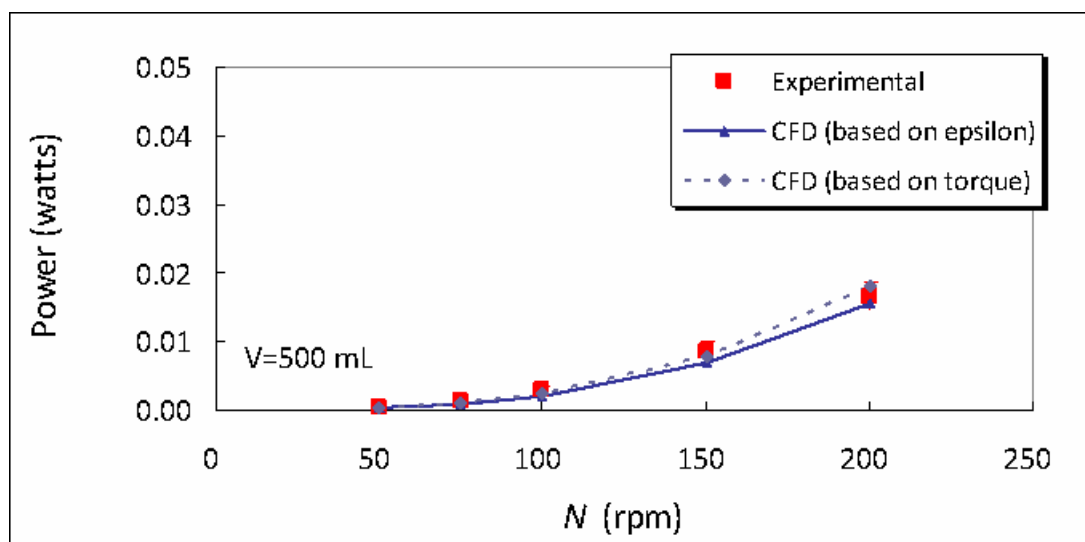
(b)

Figure 5.2 Power dissipation as a function of agitation speed in standard Apparatus 2: (a) 900 mL; (b) 500 mL.

Figure 5.3 and Tables 5.3, 5.4 present the experimentally obtained P data as a function of agitation speed in modified Apparatus 2 with 900 mL, 500 mL water, respectively. In 900 mL volume (Figure 5.3 (a)), at 50, 75 and 100 rpm, power dissipated in modified Apparatus 2 are very small (0.00075 Watts) when compared to the power

dissipation at 150 rpm (0.01729 Watts) and 200 rpm (0.03812 Watts). The simulation results are consistent with experimental results at lower agitation rates, such as 50, 75, 100 and 150 rpm. When agitation rate reaches 200 rpm, the simulated power dissipations (0.05260 Watts) based on epsilon are much larger than the experimental result (0.03812 Watts). In general, the power dissipation from experiments and simulations showed an agreement between each other except at 200 rpm in modified Apparatus 2. This could be explained as follows. The design of the experiment setup is aimed at obtaining a tiny and sensitive torque measurement through a dynamometer. When the impeller is rotating, the torque applied on the impeller can be delivered to the polystyrene foam, where the dynamometer can measure the force delivered from the whole system. If the impeller is centrally located in the vessel, the vessel contained with water rotates around the shaft without changing the center of gravity. Therefore, under this situation, the dynamometer prevents the floating vessel assembly from turning while the impeller is rotating. The torque experienced by the USP 2 vessel and the power dissipated in the liquid can be measured reliably. This makes the system especially appropriate to measure small power dissipations, as in the case of Apparatus 2 where impeller is centrally located. However, when the impeller and shaft are moved to the side of the vessel, the center of gravity of the vessel and water contained changes while the impeller is rotating. Although the dynamometer keeps preventing the floating vessel assembly from turning, the dynamometer receives unstable signal from the system. It is obvious from the observation during experiments that the vessel moves unstable. Therefore, the torque experienced by the modified Apparatus 2 can no longer be measured reliably at higher

agitation rates, i.e., 200 rpm. This method is not recommended for such measurements under higher agitation rates, such as 200 rpm.

In addition, the simulation of power dissipated in 500 mL, modified Apparatus 2 vessel (Figure 5.3(b)) is quite close to the experimental data. Power dissipated in 500 mL, modified system increases with an increasing agitation rate. A close agreement could be found between experimental and CFD results at 50, 75, 100 and 150 rpm. At 200 rpm, the experimental power dissipation is 0.02764 Watts, while the CFD result based on epsilon is 0.03534 Watts. The reason of such deviation has been explained before.
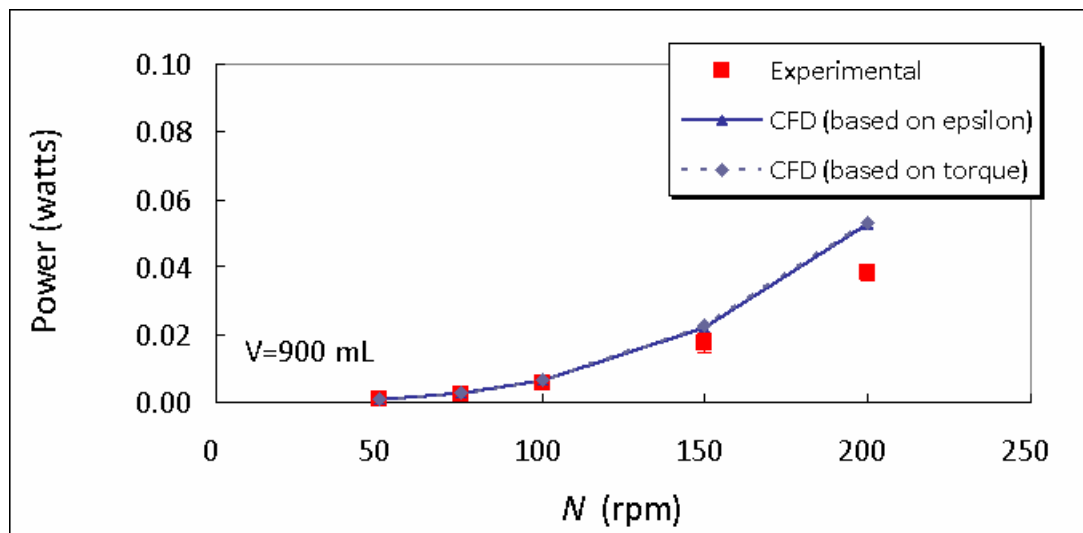
(a)
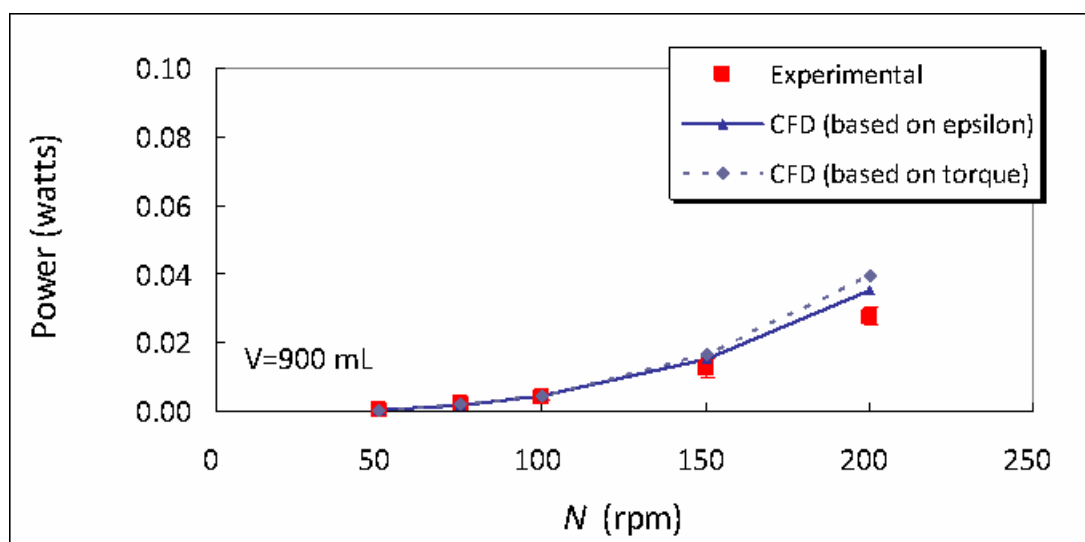
(b)

Figure 5.3 Power dissipation as a function of agitation speed in modified Apparatus 2: (a) 900 mL; (b) 500 mL.

5.5.2 Impeller Power Number

The same data are plotted in terms of the non-dimensional Power number, $Po=P/\rho N^3 D^5$ as function of N, as shown in Figure 5.4. The Power number in the 900 mL system is found to be in range of 0.24 to 0.35 (Figure 5.4(a)). As expected, this variation is much

smaller than the 43-fold increase observed for the power dissipation. At 50 rpm, the simulation predictions, based on both epsilon and torque, match very well with the experimental results. At 75, 100, 150 and 200 rpm, simulation results obtained from torque are in general larger than the experimental results, although within the experimental error for the most part. The power number decreased slightly with N, at least from 50 rpm to 75 rpm, but then it levels off for $N \geq 100$ rpm.

In the 500 mL system, Po also shows a decreasing trend with an increasing agitation rate (Figure 5.4(b)). The experimental power number in this case ranges from 0.20 to 0.38. At 50 rpm, the results obtained from experiment and simulation based on torque matched exactly. The power number from simulation based on epsilon is smaller than the experimental power number at 50 rpm. Between 50 rpm and 75 rpm, the decrease in Po is more pronounced, but Po declines very slowly for $N \geq 75$ rpm. This trend is common to both the simulations and the experimental results. As before, the agreement between the experimental data and the predicted results is in general within the experimental error.
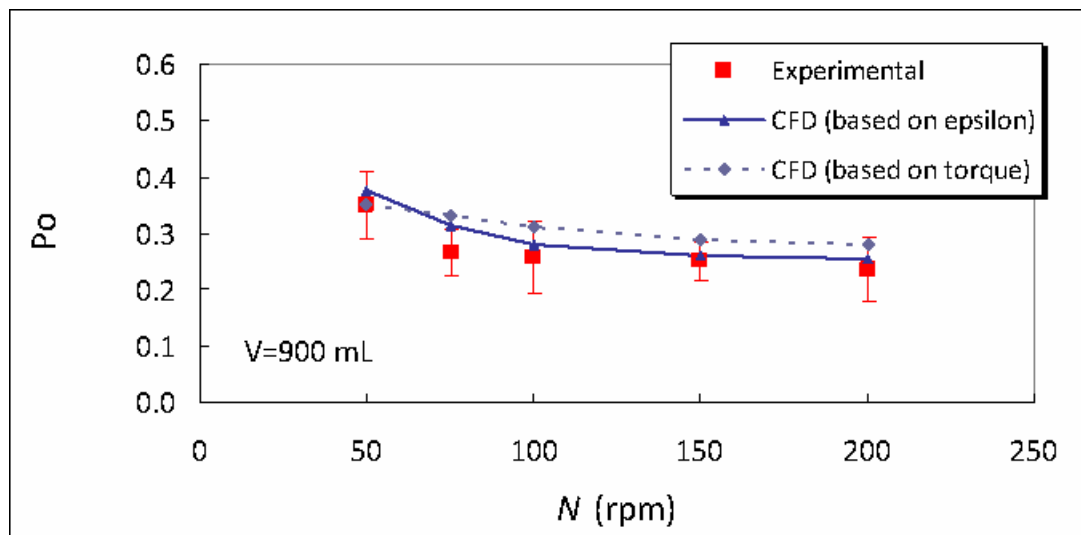
(a)
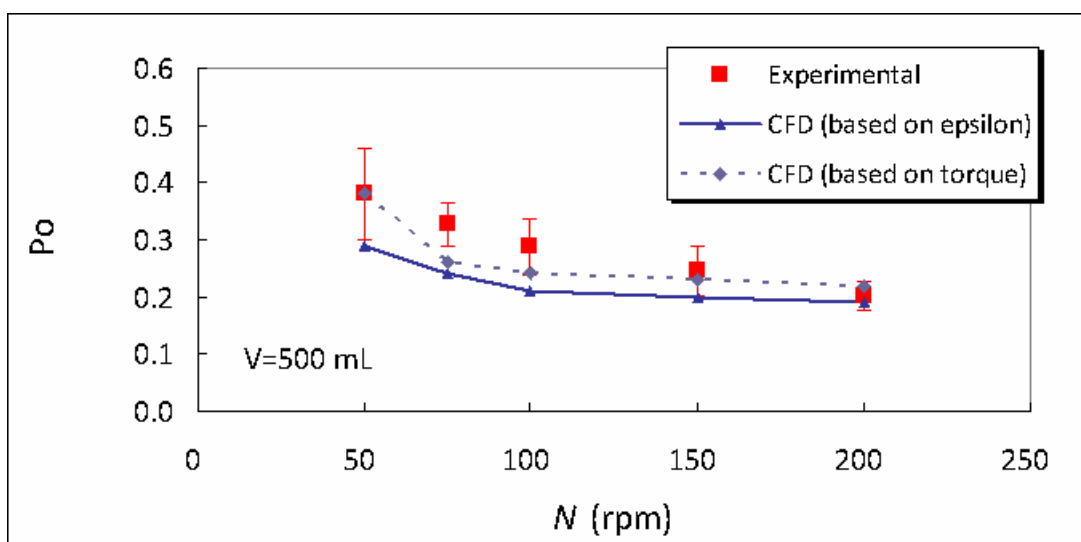
(b)

Figure 5.4 Power number as a function of agitation speed in standard Apparatus 2: (a) 900 mL; (b) 500 mL.

Power numbers in 900 mL and 500 mL in modified Apparatus 2 are plotted versus agitation rate in the Figure 5.5. Experimental power number in 900 mL modified system (Figure 5.5(a)) is in range of 0.46 to 0.59. At 50, 75 and 100 rpm, the simulation power numbers are greater than the experimental data. At 150 and 200 rpm, the

difference between the experimental power number and the simulation results become bigger when compared to lower agitation rates, i.e., 50, 75 and 100 rpm. The experimental power numbers decrease from 50 rpm to 200 rpm. However, the simulation power numbers keep constant from 50 to 200 rpm. Both simulation power numbers match with each other very good.

Experimental power number in the 500 mL modified system (Figure 5.5(b)) also shows a decreasing trend with an increasing agitation rate. The experimental power number in this volume ranges from 0.34 to 0.51. At 50, 75 and 100 rpm, the results obtained from experiment and simulation perfectly matches with each other. At 150 rpm, the experimental power number decreases while the simulated power number based on torque increases slightly. At 200 rpm, the experimental power number still keeps decreasing gently while the computational power number (based on torque) keeps constant. At 150 and 200 rpm, simulation results based on torque show difference with experimental power number. The simulated power numbers based on epsilon are in between of the experimental results and the torque-based simulation results at 150 and 200 rpm.
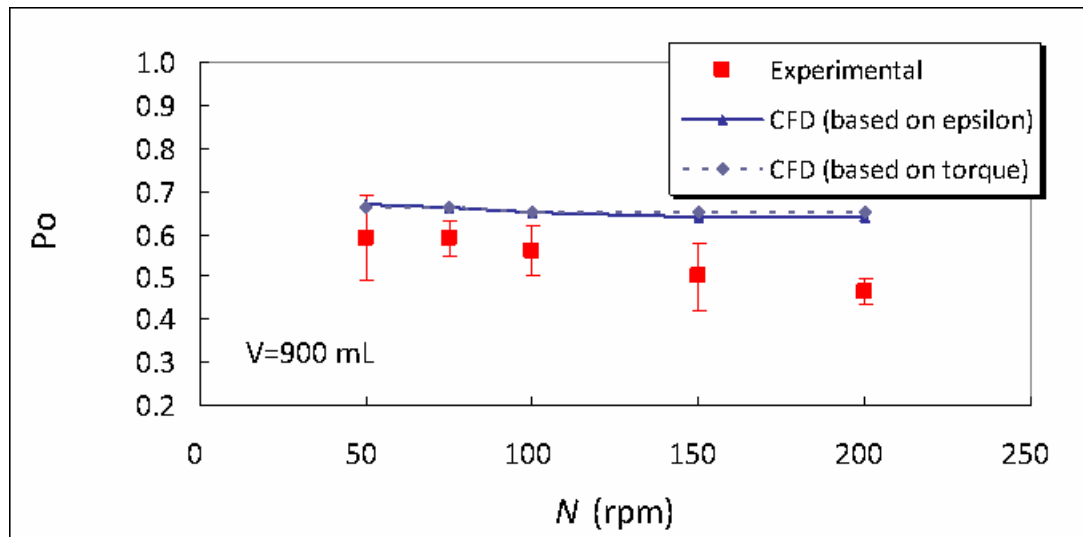
(a)
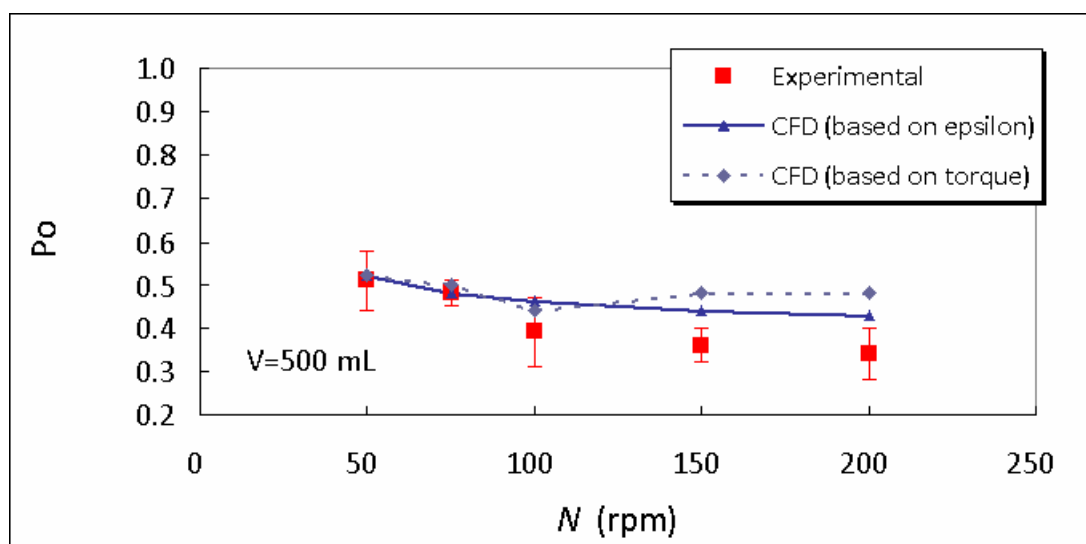
(b)

Figure 5.5 Power number as a function of agitation speed in modified Apparatus 2: (a) 900 mL; (b) 500 mL.

In practice, this CFD prediction based on energy dissipation rate, ε, is less reliable than that based on the torque determination from the pressure distribution on the blades since it requires a very accurate determination of the power distribution, which, in turns depends on the accuracy of the turbulence model, especially in the small frequency

domain of the energy spectrum region, since the local energy dissipation occurs primarily in this range.

Finally, in Figures 5.6 and 5.7, the power numbers are plotted as a function of the impeller Reynolds number using the conventional log-log plot typically used to report power data for impellers in stirred tanks. The results displayed in Figure 5.6 are similar to those shown in the previous figure since the Reynolds number is just a multiple of N for an agitation system, such as the USP 2 apparatus used here, for which the impeller diameter and the properties of the fluid, including ρ and μ, are kept constant. Therefore, for the 900 mL case, Po is in the range 0.24 to 0.35, i.e., as before, while Re varied from about 5×10^3 to 2×10^4, which is the range of importance for dissolution testing (Figure 5.6(a)). This relatively narrow range for Po is to be expected, since the Po does not vary too significantly for most impellers when the Reynolds number is sufficiently high. A similar trend can be observed for the 500 mL case (Figure 5.6(b)).
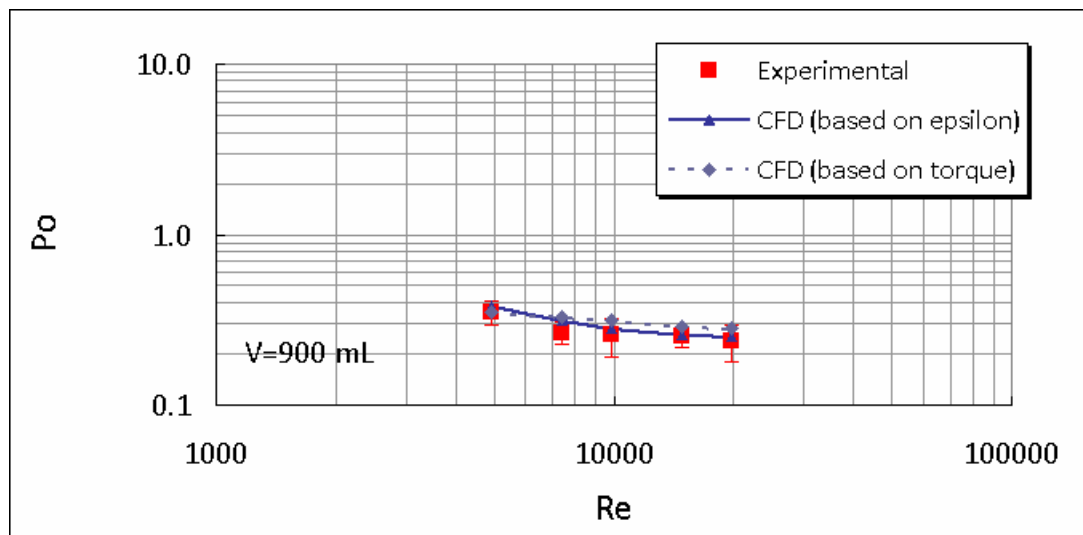
(a)
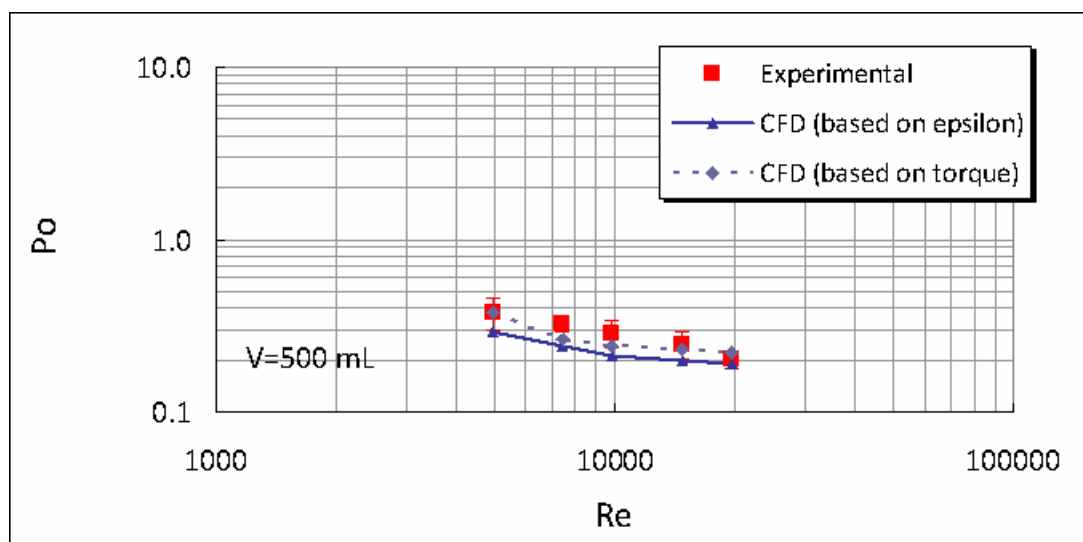
(b)

Figure 5.6 Power number versus Reynolds number in standard Apparatus 2: (a) 900 mL; (b) 500 mL.

Figure 5.7(a) and (b) are the conventional log-log plots of the power number and Reynolds number in the modified Apparatus 2 in 900 mL and 500 mL, respectively. Power number is determined for Reynolds numbers from about 5×10^3 to 2×10^4, the range of importance for the dissolution testing.

In both the 900 mL and 500 mL modified Apparatus 2, the experimental power numbers fall slightly, and never became exactly constant. The simulation power number presented a close curve to the experiments in the beginning range of Reynolds number, indicating a good prediction for the power number. However, when Reynolds number is larger than 1×10^4, simulated power number keeps constant while experimental power number decreases gently.
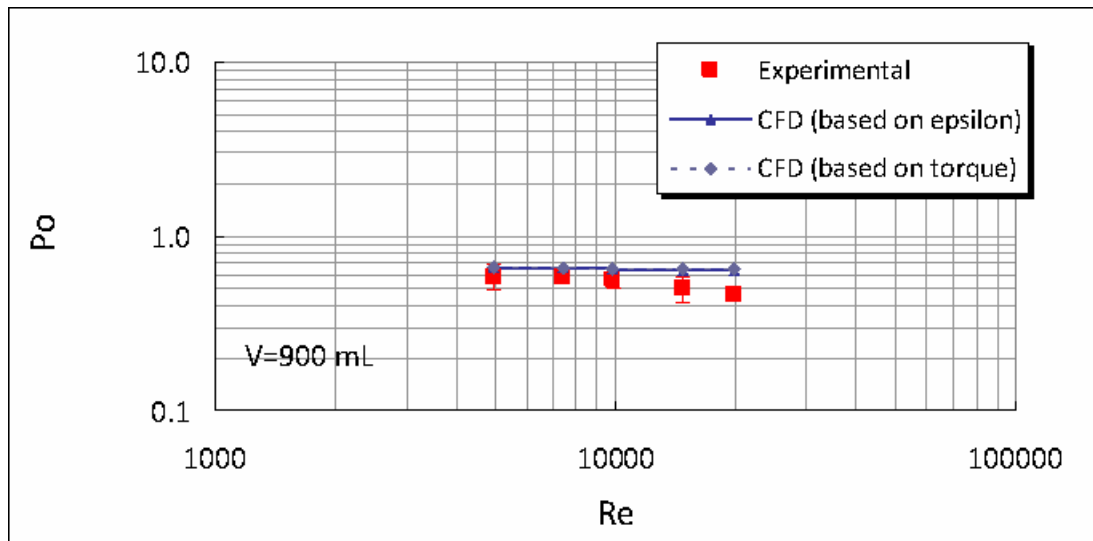
(a)
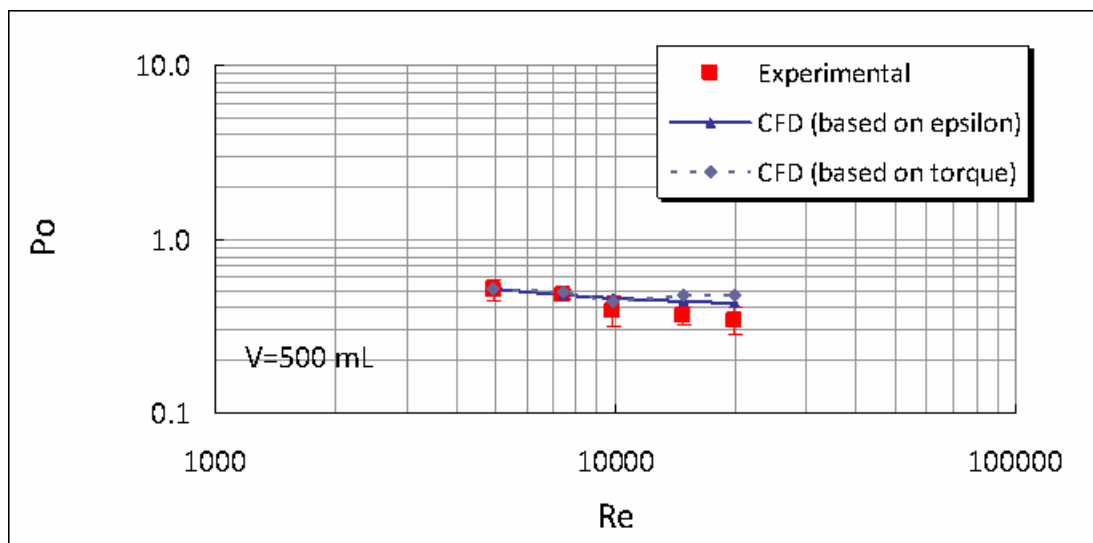
(b)

Figure 5.7 Power number versus Reynolds number in modified Apparatus 2: (a) 900 mL; (b) 500 mL.

Figure 5.8 is the conventional log-log plot of the power equation and is presented here to submit new data on USP apparatus 2 impeller and to illustrate the characteristic curves for different impeller styles. Curve 1 is the correlation between power number and Reynolds number for the radial discharging six-blade turbine impeller (*w/D*=1/5).

The power number is about 5.0 in turbulent regime. Curve 2 is for 45° pitched-blade style six-blade turbine with w/D=1/8. Power number in turbulent regime is about 1.3. Both Curve 1 and Curve 2 are obtained under the "standard" conditions in Newtonian fluids, where, H/T=1, D/T=1/3 and C/T=1/3. The power number from Curve 1 and Curve 2 are obtained in baffled mixing vessels, and keep constant while increasing the Reynolds number in turbulent regime. Curve 3 is for the impeller in USP apparatus 2, with w/D=1/4. It is worthy to notice that power number of Curve 3 levels off in the turbulent regime, while power numbers of Curve 1 and Curve 2 keep constants in the same turbulent regime. Compare to these two commonly used impellers mentioned above in industry, impeller in USP apparatus 2 has a relatively smaller power number.
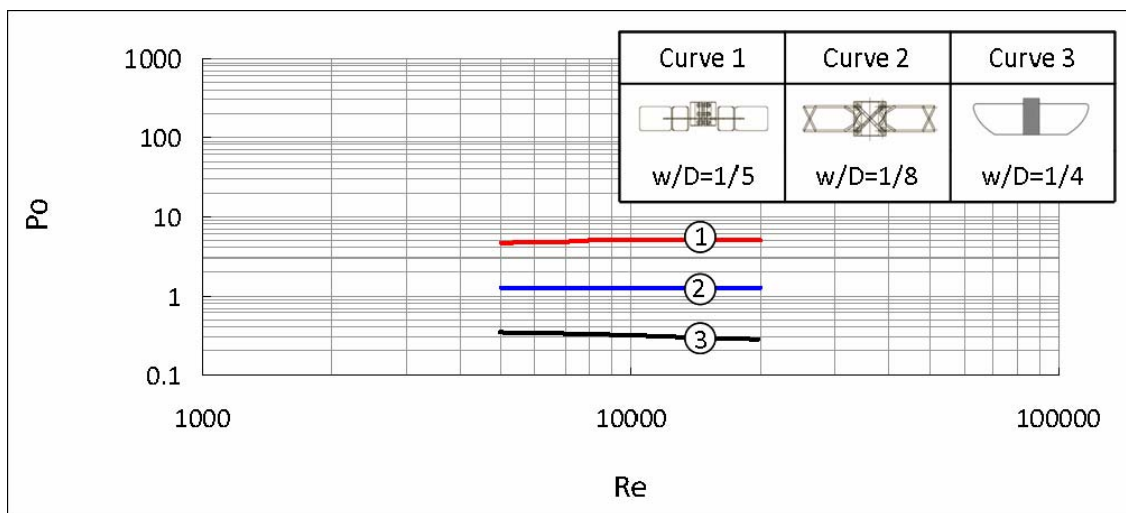
Figure 5.8 Power number-Reynolds number correlation in Newtonian fluids for various impellers.

5.5.3 Effect of Impeller Positions

Power numbers are compared with different impeller positions in Figures 5.9 and 5.10 for Apparatus 2 with 900 mL and 500 mL water, respectively. In Apparatus 2 filled with 900 mL water (Figure 5.9), both experiments and simulations indicate that the power number in modified Apparatus 2 is larger than Apparatus 2.
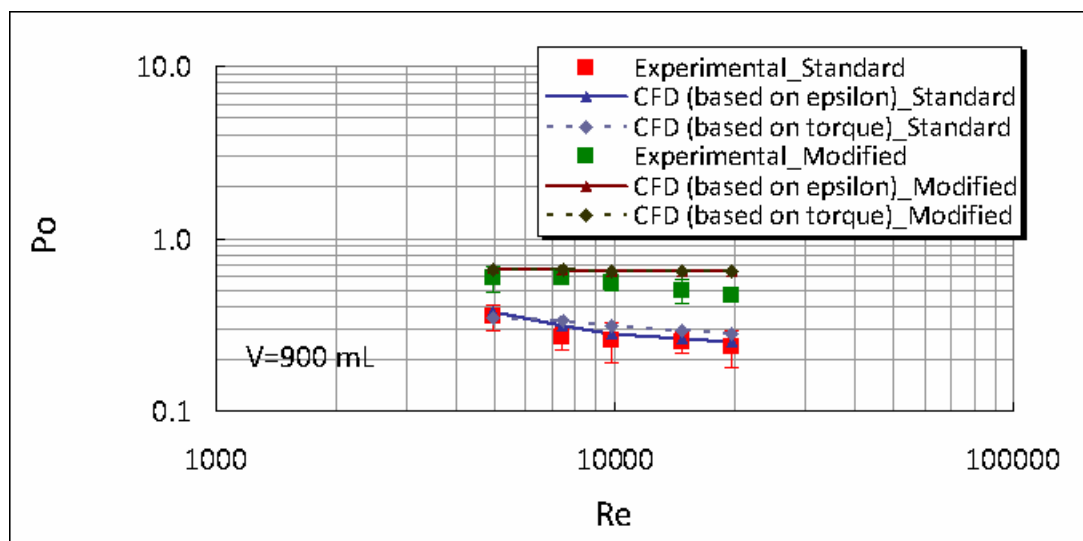
Figure 5.9 Power number versus Reynolds number in standard and modified Apparatuses 2 (900 mL water).

In 500 mL (Figure 5.10), again, both the experimental and computational power numbers are larger in the modified Apparatus 2 than the power numbers in Apparatus 2. This is understandable because the position shift of the impeller can introduce an imaginary baffling effect, which can effectively destroy the solid body rotation in Apparatus 2 and hence improve the uniformity of the hydrodynamics (velocity distribution and flow pattern) inside the vessel during dissolution testing. All of these will require higher energy input and consequently lead to relatively higher power numbers.
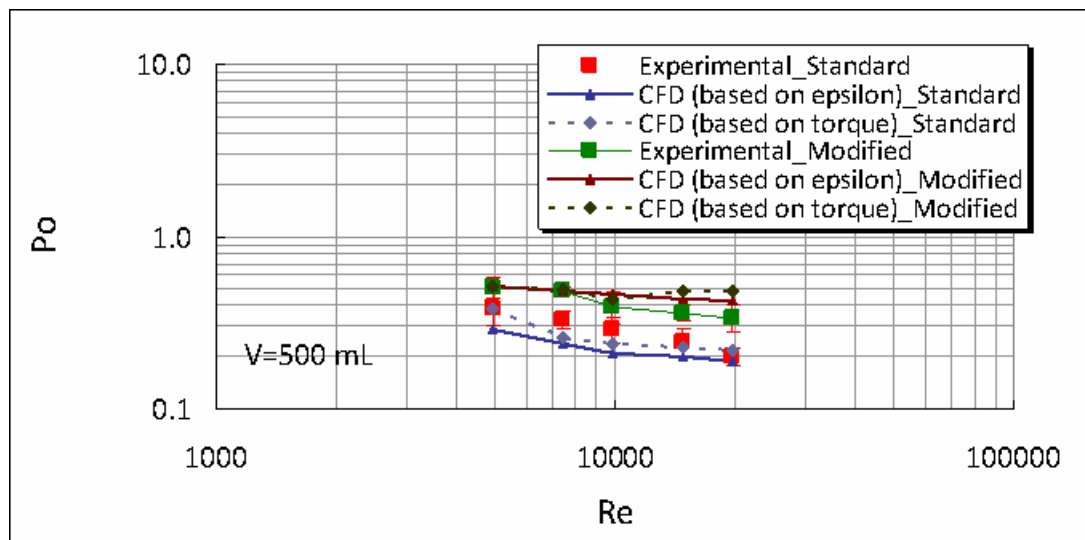
Figure 5.10 Power number versus Reynolds number in standard and modified Apparatuses 2 (500 mL water).

Although power dissipation in agitated systems has been measured before in a number of studies in which the magnitude of the power was much higher, this is probably one of the first times in which an agitated system dissipated so little power and generated so little torque that it necessitated the development of an apparatus dedicated to this purpose. A number of issues have to be overcome, most of them related to the elimination of measurement errors possibly introduced by friction. Other approaches have been attempted in this work, such as the use of very light and "strainable" shafts combined with strain gauges. However, none of them worked and they were therefore abandoned (results not shown). The floating-platform approach used here eliminated the friction problem at the source, since, under static conditions, neither water, nor any Newtonian, can generate any shear stress. Hence, the experimental torque data, and the resulting power dissipation data are expected to be accurate. This method would be recommended for power measurement from vessels where impellers are centrally located.

5.5.4 Mass Transfer Coefficient

Based on Equations 5.5 and 5.6, mass transfer coefficient was calculated as a function of drug particle size and power input during dissolution testing in Apparatus 2 (Equation 5.13). It is worthy to notice that although power input has an impact on mass transfer coefficient during dissolution testing, the impact is relatively small compared to the effect of drug particle size after drug disintegration (Figure 5.11). In Figure 5.11, the mass transfer coefficient (m/s) is plotted in terms of particle size (m) and power input (Watts). The mass transfer coefficient changes rapidly when the particle size increases; however, power dissipation has a minor impact on mass transfer coefficient. Each pair of particle size and power input has a specific mass transfer coefficient during dissolution testing.

$$k = \frac{1.43 \times 10^{-9}}{d_p} + 5.44 \times 10^{-6} \times d_p^{-0.31} \times P^{0.17} \tag{5.13}$$
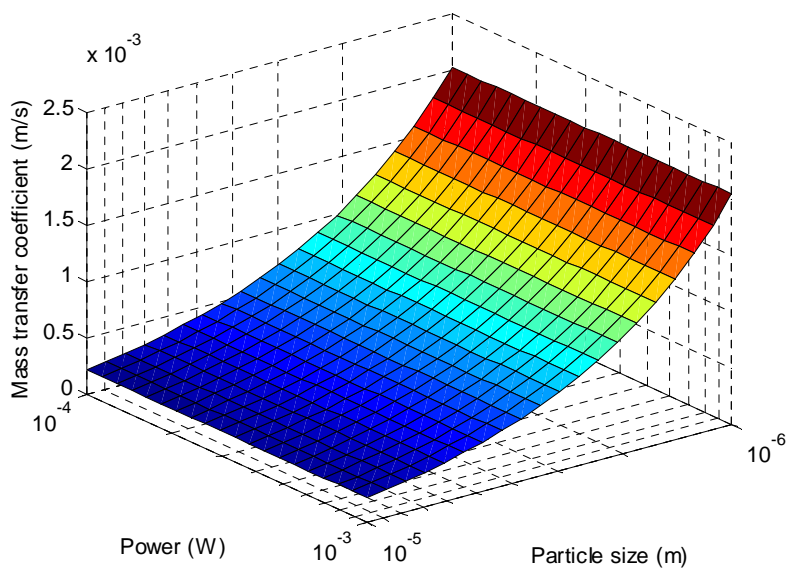
Figure 5.11 Mass transfer coefficient as a function of particle size and power input.

More specifically, the mass transfer coefficient in USP apparatus 2 with 900 mL water at 50, 75 and 100 rpm agitation rates are listed in Table 5.5. The energy input at different agitation rates is different, hence, leading to a different mass transfer coefficient. However, the difference of k_{SL} is not too significant (Figure 5.11).

Table 5.5 Mass Transfer Coefficient in Standard Apparatus 2 at Agitation Speeds of 50, 75 and 100 rpm (900 mL Water)

Particle size (μm)	k_{SL} (m/s)		
	50 rpm	75 rpm	100 rpm
10	1.58E-04	1.61E-04	1.63E-04
20	8.37E-05	8.60E-05	8.81E-05
30	5.84E-05	6.05E-05	6.23E-05
40	4.56E-05	4.75E-05	4.91E-05
50	3.78E-05	3.96E-05	4.11E-05
60	3.25E-05	3.42E-05	3.57E-05
70	2.87E-05	3.03E-05	3.17E-05
80	2.58E-05	2.74E-05	2.87E-05
90	2.36E-05	2.51E-05	2.63E-05
100	2.17E-05	2.32E-05	2.44E-05

5.6   Conclusions

In this chapter, power consumption and impeller power number in Apparatus 2 and modified Apparatus 2 were experimentally measured with a dynamometer at five different agitation speeds (50, 75, 100, 150 and 200 rpm) and two different volumes (900 mL and 500 mL). A computational fluid dynamic (CFD) software package (FLUENT) was used to numerically predict the power consumption of the impeller. Turbulence

effects were simulated using the standard $k\text{-}\varepsilon$ model. The agreement between the experimental data and the numerical predictions was found to be significant in most cases.

In Apparatus 2, the power number was found to decrease slowly while increasing the agitation rates although it never reached an asymptotic value. In the modified Apparatus 2, the differences between the experimental power number and predicted power number were still acceptable but more pronounced, especially at higher agitation rate, i.e., 200 rpm. Power number from simulation was nearly constant in the range of Reynolds numbers tested here, while the experiment data showed a slightly decreasing trend.

A model of the mass transfer coefficient in terms of drug particle size and power input was used. Drug particle size has a significant impact on mass transfer coefficient while power input does not affect k_{SL} as much as particle size.

CHAPTER 6

MIXING TIME IN STANDARD AND MODIFIED APPARATUSES 2

6.1   Introduction

Mixing time, or blend time, is the parameter that describes how long it takes for a liquid in a mixing system to achieve a pre-defined level of homogeneity throughout the liquid itself, and it is a measurement of the effectiveness of the mixing device under investigation. Mixing time is also referred to macroscale mixing time, since this is the time scale associated with mixing the entire content of the vessel to a predefined level. Mixing on the macroscale in turbulent systems is controlled through the use of agitators [67].

In stirred vessels, mixing time depends on impeller speed, power number and the size of the impeller relative to the size of the vessel. Most low-viscosity turbulent applications require baffles to prevent solid body rotation of the liquid, which does not create effective mixing. The most common methods for mixing time measurements in agitated vessels are conductivity probes, discoloration techniques [68, 69] and non-intrusive laser induced fluorescence measurements. Conductivity probes and laser-induced fluorescent techniques are the most common methods to determine experimentally mixing time for different agitated vessels. However, it has been shown that the mixing time obtained using these techniques depends on probe size [70], probe location [71, 72], feed pipe location [73], vessel size [74], and other variables. In the discoloration method, mixing time is determined by adding a small quantity of a liquid to an agitated vessel of similar property liquid. Laboratory tests most often add a liquid that results in a color change, and conduct tests in transparent tanks, allowing the observation

of the color change with time and the determination of indicating the degree of mixing achieved at any time [75]. Some more common color change methods use either a pH indicator solution or an iodine color remover. With the pH approach, a color-to-clear indicator, such as phenolphthalein, first is added into the vessel with sodium hydroxide to form a pink color. Then a small quantity of a more concentrated acid is added to the liquid. The quantity and concentration of the acid is sufficient to take the batch from alkaline to acidic conditions. Repeated tests with careful addition and timing establish a good average for mixing time at the prescribed degree of uniformity. Mixing time test results typically are correlated as a dimensionless mixing time θ, which is expressed as measured mixing time multiplied by the impeller rotational speed. This is dimensionless because mixing time has the units of time and rotational speed has the unit of reciprocal time. For many turbulent systems, θ can be shown to be a constant for geometrically similar configurations. [75]

Correlations have been developed in a form involving the dimensionless mixing time θ, the impeller agitation speed N, the impeller diameter-to-tank diameter ration D/T, the liquid level-to-tank diameter ratio H/T, and the number of impellers n_i. For a four-blade 45° pitched-blade turbine, mixing time for 99% uniformity can be expressed as (Equation 6.1):

$$\theta_{99\%} = (6.34/N)(D/T)^{-2.3}(H/T)^{0.5}n_i^{-0.7} \qquad (6.1)$$

For a four-blade straight blade turbine, the expression becomes (Equation 6.2):

$$\theta_{99\%} = (4.80 / N)(D / T)^{-2.3} (H / T)^{0.5} n_i^{-0.6} \tag{6.2}$$

For hydrofoil impellers, typical three blades, narrow blade or marine propellers, the expression is (Equation 6.3):

$$\theta_{99\%} = (16.4 / N)(D / T)^{-1.7} (H / T)^{0.5} n_i^{-0.8} \tag{6.3}$$

Rate of tracer addition can significantly impact the amount of time needed to attain desired uniformity. If the injection rate is very slow, say ten minutes, therefore, uniformity cannot be achieved until after ten minutes. An intermediate injection rate which is also much less than the estimated mixing time may be appropriate. A high injection rate, sufficient to influence the mixing flow pattern, may lead to a slightly reduced or at least different mixing time [75].

The quantity of tracer addition has effects similar to those for the injection rate. If putting in that amount of injection takes longer than estimated mixing time, then the mixing time becomes the sum of injection time and the mixing time. An intermediate amount of injection would be appropriate for estimating mixing time. [75]

Sometimes location of the feed is more important than its rate or quantity. Typically, surface feed is chosen for mixing experiments. However, for the case of dissolution vessels, the injection should be at the bottom of the vessel considering the drug always locates in the bottom area. The objective in this case is to determine how long it takes for the Active Pharmaceutical Ingredients (API) released from the dissolving tablet to reach a pre-defined homogeneity in the whole vessel.

Information on mixing low viscosity fluids is widely available in the literature [76]. One common approach is to determine the mixing time required achieving a pre-defined degree of homogeneity. This is usually done in stirred tanks equipped with conventional impellers. Different variables affecting the mixing time have been previously studied: impeller type, number of impellers and tank geometry are just a few of them. However, no information, other than that generated by this research group, is available on mixing time of USP Apparatus 2.

The objective of this section is to quantify the mixing time in the conventional USP Apparatus 2 as well as the modified Apparatus 2, by measuring the time required for an added tracer to reach the 95% homogeneity level during dissolution testing. This, in turns, determines how rapidly the API released from a tablet undergoing dissolution testing becomes homogenized within the vessel's liquid contents. Mixing time was determined experimentally using a tracer initially injected from the bottom of the vessel at time zero. The mixing time was monitored at different sites in Apparatus 2 and modified Apparatus 2. In order to find out the mixing time accurately, a monitoring system was set up to follow the concentration of the tracer (HCl) in the vessel as a function of time. In this work, two variables were varied to determine how they affect mixing time, i.e., agitation speed, and impeller location.

CFD simulations were also conducted here to computationally predict mixing time. This was achieved by first determining the flow field in the entire vessel, and then activating the species transport model in the simulator.

6.2   Experimental Method and Apparatus

Mixing time was determined by analyzing the progress of a de-colorization reaction of an indicator using, image analysis, in the presence of an acid-base reaction (NaOH and HCl). An alkaline solution (3 mL of 1.0 M NaOH solution) was first placed in the vessel together with an indicator (phenolphthalein). Then an acid solution (3 mL of a 1.2 M HCl solution) was injected from the bottom of the vessel at the beginning of each experiment at the rate of 1 mL/sec. A digital camera was used to record the neutralization process, as the color changed from pink to colorless during the mixing process. Digital images were recorded with a CCD camera (15 images/sec – 1k x 1k resolution). Each frame was quantitatively analyzed by determining the light intensity for a number of pixels at each time. The Matlab Image Analysis Toolbox was then used here to follow the progression of the light intensity over time at selected locations. Mixing time was measured in both Apparatus 2 and modified Apparatus 2. This technique has been previously used to determine the mixing time for unconventional impellers with robust and reproducible results [68].

The experimental procedure is briefly stated as the following:

1. Agitation is started and the indicator is introduced into Apparatus 2.
2. 3 mL of NaOH 1.0 M are introduced into the vessel. Therefore, the color turns pink.
3. 3 mL of HCl 1.2 M are introduced into the vessel at the beginning of the experiment (time=0).

The color change is observed and recorded by taking digital images with the CCD camera and storing them on a computer for further analysis. The digital pictures are analyzed with Matlab:

1. A working zone is selected in which the agitator is removed from the image.

2. The red, blue and green (RGB) color intensity for a number of pixels in each picture is extracted.

Only the green component was analyzed here since it was the least sensible to external light [68]. The number of mixed pixels at target region at each time was recorded. The mixing efficiency is calculated at different times:

$$M = \frac{\#\,Mixed\ \ Pixels}{\#\,Total\ \ Pixels} \tag{6.4}$$

With M=0 at time=0 and M=1 at time=∞, if the system is completely mixed, a curve of M at different times can, therefore, be plotted and the mixing time is found as the time needed for such curve to reach the value 0.95.

The mixing time is determined in both standard Apparatus 2 and modified Apparatus 2 at 50, 75 and 100 rpm.

Due to the hemispherical bottom, Apparatus 2 is supported on a specifically designed rack with a relevant hole on it. Apparatus 2 together with the rack is fit on a square tank. The tank is filled with water in order to eliminate the light reflection when doing experiments.

6.3   CFD Predictions

Many modeling studies of turbulent flow characteristics of stirred vessels are available in the literature. Osman and Varley [77], Jaworski et al. [72], Bujalski et al. [78], Shekhar and Jayanti [79] used RANS equation approach to predict the mixing time. Fully predictive simulations of mixing time commonly use either the sliding mesh or the

multiple reference frames (MRF) approaches. Sliding mesh is a fully transient approach in which the rotation of the impeller relative to the baffles is explicitly taken into account, while in the MRF a steady flow field is predicted for a fixed position of the impeller. Sliding mesh is more accurate but it is also much more time consuming than MRF. Jaworski and Dudczak [80] used the sliding mesh and standard k-ε model and wall function for the macromixing in a stirred tank. Osman and Varley [77] studied the mixing time in an unbaffled vessel stirred by a Rushton turbine using MRF approach. The results were found to be two times longer than the experimental results. The underestimation of mean velocity in the trailing vortex region was the main reason caused the discrepancies. Shekhar and Jayanti [79] successfully simulated the flow and mixing characteristics in an unbaffled vessel stirred by a paddle impeller using a low Reynolds k-ε model for rather low flow Reynolds numbers.

Species Transport Model

FLUENT can model the mixing and transport of chemical species by solving conservation equations describing convection, diffusion, and reaction sources for each component. Multiple simultaneous chemical reactions can be modeled, with reactions occurring in the bulk phase and/or on wall or particle surfaces, and in the porous region. When one chooses to solve conservation equations for chemical species, FLUENT predicts the local mass fraction of each species, Y_i, through the solution of a convection-diffusion equation for the ith species. This conservation equation takes the following general form:

$$\frac{\partial}{\partial t}(\rho Y_i) + \nabla \cdot (\rho \vec{u} Y_i) = -\nabla \cdot \vec{J}_i + R_i + S_i \qquad (6.5)$$

where R_i is the net rate of production of species i by chemical reaction and S_i is the rate of creation by addition from the dispersed phase plus any user-defined sources. An equation of this form is solved for $N-1$ species where N is the total number of fluid phase chemical species present in the system. Since the mass fraction of the species must sum to unity, the Nth mass fraction is determined as one minus the sum of the $N-1$ solved mass fractions.

In Equation 6.5, $\vec{J}_i$ is the diffusion flux of species i, which arises due to concentration gradients. By default, FLUENT uses the dilute approximation, under which the diffusion flux can be written as Equation 6.6.

$$\vec{J}_i = -\rho D_{i,m} \nabla Y_i \qquad (6.6)$$

Here $D_{i,m}$ is the diffusion coefficient for species i in the mixture.

In turbulent flows, FLUENT computes the mass diffusion in the following form:

$$\vec{J}_i = -(\rho D_{i,m} + \frac{\mu_t}{Sc_t})\nabla Y_i \qquad (6.7)$$

where Sc_t is the turbulent Schmidt number ($Sc_t = \dfrac{\mu_t}{\rho D_t}$, where μ_t is the turbulent

viscosity and D_t is the turbulent diffusivity).

6.4   Results and Discussions

6.4.1 Mixing Time

When a miscible tracer is added to a homogenous liquid in an agitated vessel, the local concentration typically fluctuates with time.   The amplitudes of the concentration fluctuations decrease with time, and eventually the tracer concentration becomes completely uniform throughout the vessel.   The mixing time defined here is the time required for the tracer to reach a 95% degree of uniformity in the liquid at the sampling location in USP Apparatus 2.   The mixing times obtained from experiments and simulations in Apparatus 2 as a function of velocity are listed in Table 6.1 (Apparatus 2, 500 mL solution), and in Table 6.2 (modified Apparatus 2, 500 mL solution) at 50, 75 and 100 rpm.

Table 6.1 Mixing Time for Standard Apparatus 2 (500 mL Solution)

N (rpm)	$t_{95\%}$ (second) (Experimental)	$t_{95\%}$ (second) (Predicted)
50	20.9±0.5	21.8
75	15.5±0.5	16.2
100	13.9±0.8	14.0

Table 6.2 Mixing Time for Modified Apparatus 2 (500 mL Solution)

N (rpm)	$t_{95\%}$ (second) (Experimental)	$t_{95\%}$ (second) (Predicted)
50	19.0±0.8	20.4
75	14.3±0.6	15.6
100	12.1±0.6	13.6

The relative concentration of HCl from experiments is plotted in Figure 6.1 as a function of time in Apparatus 2 with 500 mL solution. The x axis represents the experimental time in second, and y axis is the relative concentration of HCl during experiments. In the initial several seconds, C/C^* was almost zero. At 50 rpm, C/C^* increased from zero to one gradually and reached the predetermined 95% homogeneity level value at about 20.9 seconds. C/C^* increased faster at 75 and 100 rpm, and reached the 95% level at 15.5 and 13.9 seconds, respectively.
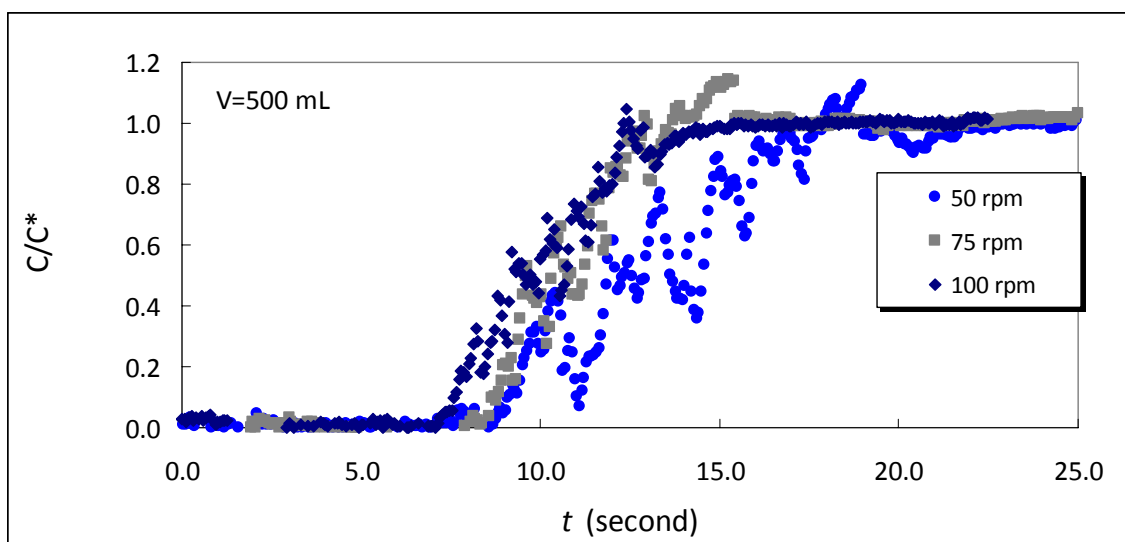
Figure 6.1 Experimental relative concentration of HCl as a function of time in standard Apparatus 2 (500 mL solution) at agitation speeds of 50, 75 and 100 rpm.

The results for the simulation of *C/C** for HCl in Apparatus 2 with a 500 mL solution are plotted as a function of the time in Figure 6.2. At 50 rpm, *C/C** reached the 95% homogeneity level in the whole vessel at 21.8 seconds. At 75 rpm, *C/C** 16.2 seconds were required and 14.0 seconds at 100 rpm.
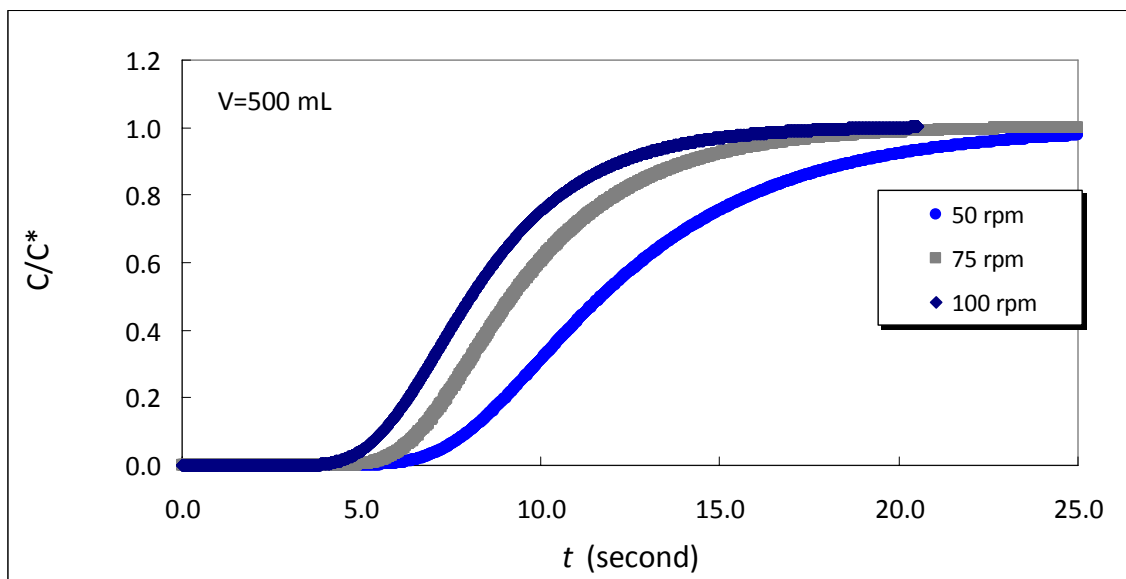
Figure 6.2 Predicted relative concentration of HCl as a function of time in standard Apparatus 2 (500 mL solution) at agitation speeds of 50, 75 and 100 rpm.

The mixing time obtained from Figures 6.1 and 6.2 are plotted as a function of agitation rates in Figure 6.3. Both experimental mixing time and simulated mixing time decrease with an increasing in agitation rates.   The predicted mixing times are 21.8, 16.2 and 14.0 seconds at 50, 75 and 100 rpm, which is about 0.9, 0.7 and 0.1 second greater than experimental results at 50, 75 and 100 rpm.   The simulation results are in good agreement with the experimental mixing times.

Figure 6.3 Mixing time versus agitation speed in standard Apparatus 2 (500 mL solution).

The experimental *C/C** evolution with time in the modified Apparatus 2 with 500 mL of solution is plotted as a function of agitation speed (Figure 6.4). At 50 rpm, *C/C** reached the 95% homogeneity level in 19.0 seconds. At 75 and 100 rpm show the corresponding 95% missing time was reached in a shorter time (14.3 seconds at 75 rpm and 12.1 seconds at 100 rpm).
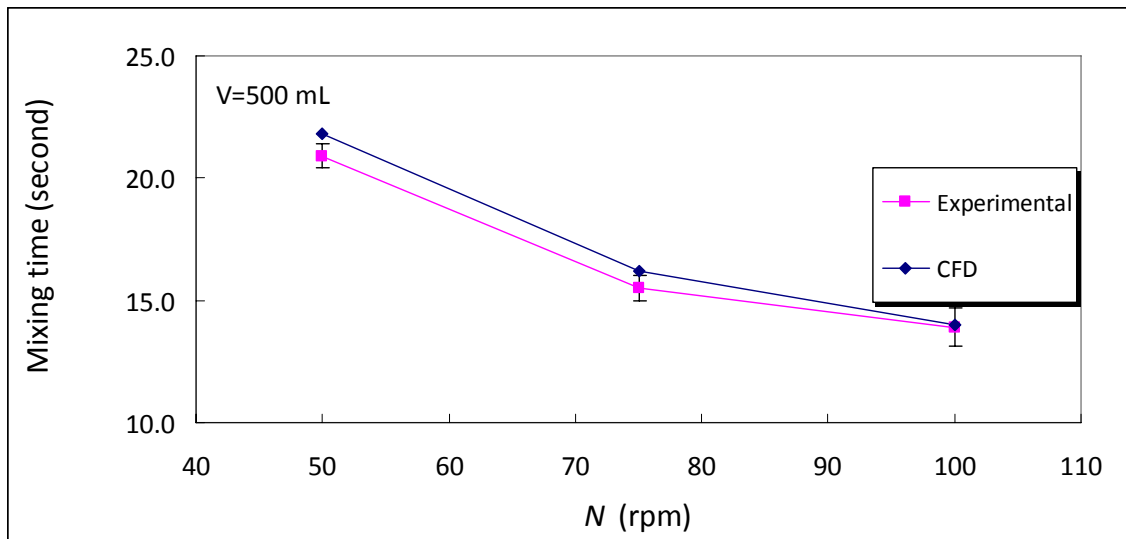
Figure 6.4 Experimental relative concentration of HCl as a function of time in modified Apparatus 2 (500 mL solution) at agitation speeds of 50, 75 and 100 rpm.

The results for the simulation of C/C^* for HCl in the modified Apparatus 2 with a 500 mL solution are plotted as a function of the time in Figure 6.5. C/C^* reached the 95% homogeneity level in the whole vessel at 20.4, 15.6 and 13.6 seconds, at agitation speeds equal to 50, 75 and 100 rpm, respectively.
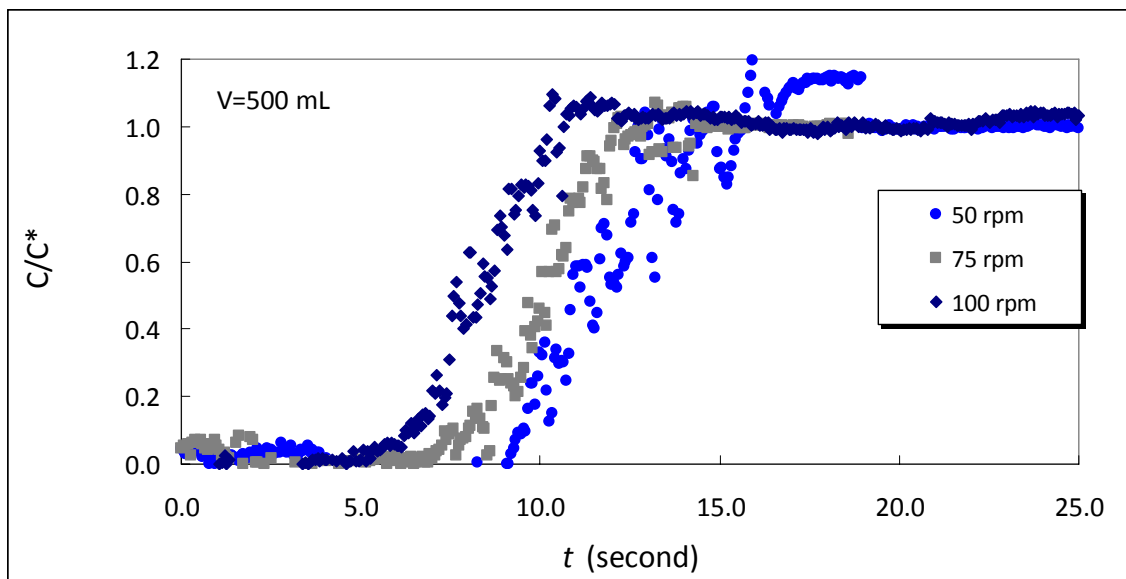
Figure 6.5 Predicted relative concentration of HCl as a function of time in modified Apparatus 2 (500 mL solution) at agitation speeds of 50, 75 and 100 rpm.

In Figure 6.6, both experimental mixing time and predicted mixing time can be shown to decrease with increasing agitation speeds. The predicted mixing times are 1.4, 1.3 and 1.5 seconds greater than experimental results at 50, 75 and 100 rpm. Also in this case, the simulation results are in good agreement with the experimental mixing times.
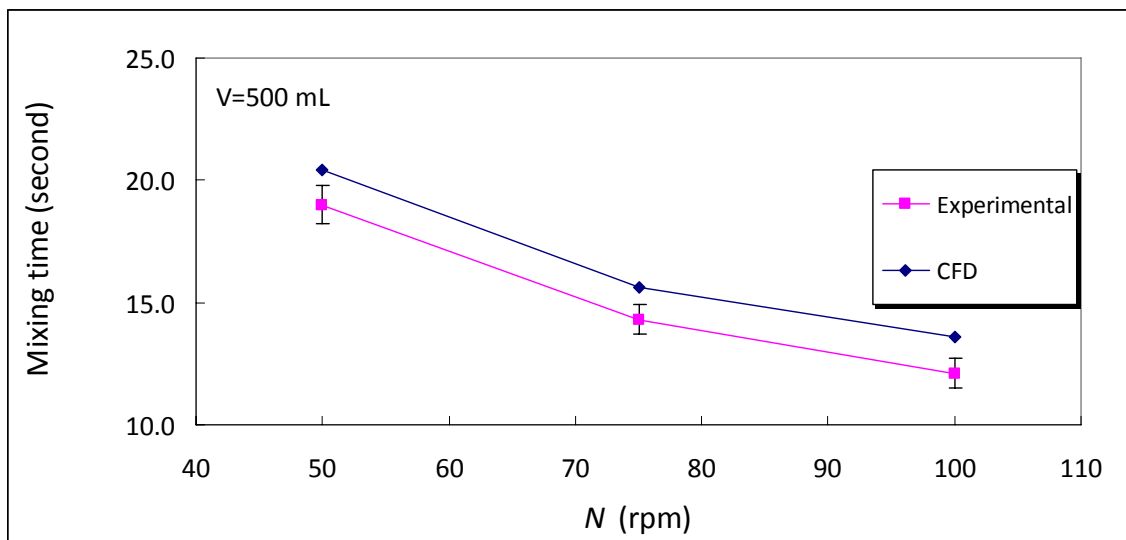
Figure 6.6 Mixing time versus agitation speed in modified Apparatus 2 (500 mL solution).
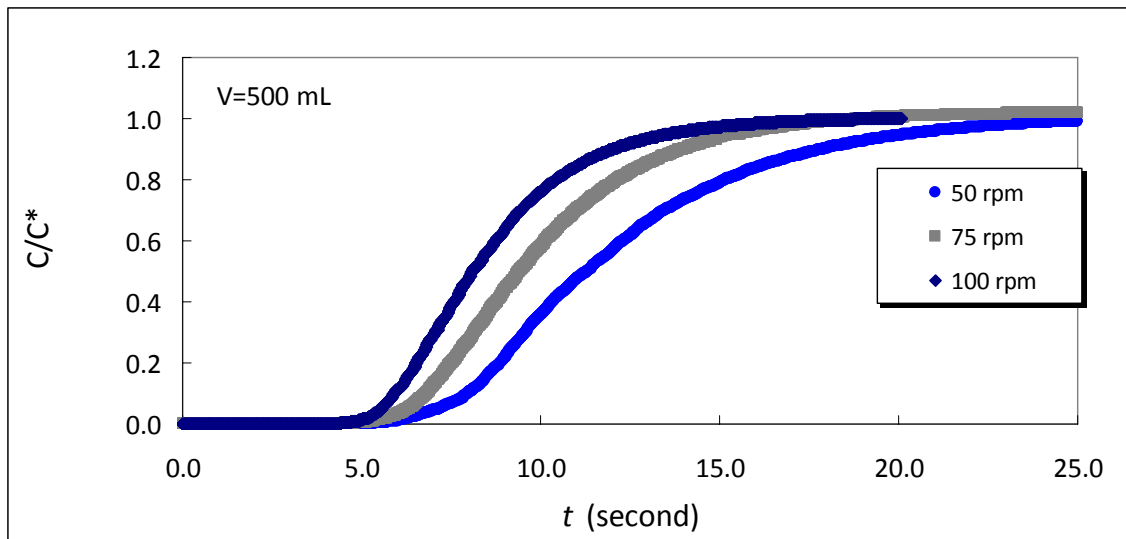
Simulated mixing time in modified Apparatus 2 decreases by 6.4% at 50 rpm compared to Apparatus 2, and by 3.7% and 2.9%, respectively, at 75 and 100 rpm. The experimental mixing time in modified Apparatus 2 decreased by 9.1%, 7.7% and 12.9% compared to Apparatus 2 at 50, 75 and 100 rpm (Table 6.3).

Table 6.3 Percentage of Mixing Time Decreased in Modified Apparatus 2 Compared with Standard Apparatus 2 at Different Agitation Speeds

	Percentage of mixing time decrease (%)		
	50 rpm	75 rpm	100 rpm
Experimental	9.1	7.7	12.9
CFD	6.4	3.7	2.9

The experimental results validate the CFD simulation approach used here for the USP Apparatus 2. The order of magnitude of mixing time is much smaller than the time of typical dissolution testing, indicating that once the dissolved active pharmaceutical ingredient (API) leaves the boundary around the drug tablet and enters the bulk solution, it distributes itself throughout the USP apparatus 2 very quickly [17].

It is clear that in Apparatus 2 and modified Apparatus 2, the faster the agitation speeds, the shorter the mixing time is. Mixing time in modified Apparatus 2 is improved to some extent. Although the Reynolds numbers are the same in Apparatus 2 and modified Apparatus 2, the flow pattern changes. When the shaft and impeller are moved to the side, the flow pattern in modified Apparatus 2 is no longer symmetric. Instead, an asymmetric flow field results, generating a sort of baffling effect, which can effectively

prevent the formation of vortex and decrease the mixing time. The simulated mixing times matched very well the experimental mixing times.

6.4.2 Dimensionless Mixing Time

In a baffled mixing vessel, the non-dimensional mixing time was found by Grenville and Nienow [81] (Equation 6.8).

$$t_{95}N = \frac{5.20}{Po^{1/3}}\left(\frac{T}{D}\right)^{1.5}\left(\frac{H}{D}\right)^{0.5} \tag{6.8}$$

where Po is the impeller power number; T is the vessel diameter; H is the liquid height and D is the impeller diameter. This equation was derived for baffled mixing vessel under turbulent regime, when $0.33<D/T<0.50$, $C/T=0.33$, $0.5<H/T<1.0$.

The dimensionless mixing time, $t_{95}N$ in Apparatus 2 and modified Apparatus 2 are listed in Tables 6.4 and 6.5. Mixing time, t_{95} has the dimension of second, and agitation rate has the dimension of 1/second, therefore, the product of t_{95} and N is dimensionless, which is the non-dimensional mixing time.

Table 6.4 Dimensionless Mixing Time in Standard Apparatus 2 at Agitation Speeds of 50, 75 and 100 rpm (500 mL Solution)

	Dimensionless mixing time		
	50 rpm	75 rpm	100 rpm
Experimental	17.4±0.4	19.4±0.6	23.2±1.3
CFD	18.2	20.3	23.3

Table 6.5 Dimensionless Mixing Time in Modified Apparatus 2 at Agitation Speeds of 50, 75 and 100 rpm (500 mL Solution)

	Dimensionless mixing time		
	50 rpm	75 rpm	100 rpm
Experimental	15.8±0.7	17.9±0.8	20.2±1.0
CFD	17.0	19.5	22.7

The non-dimensional mixing time obtained from Tables 6.4 and 6.5 are plotted in terms of agitation rates in Figures 6.7 and 6.8. The experimental non-dimensional mixing times in Apparatus 2 (Figure 6.7) are 17.4, 19.4 and 23.2 seconds at 50, 75 and 100 rpm, respectively. The predicted non-dimensional mixing times are 18.2, 20.3 and 23.3 seconds at 50, 75 and 100 rpm, respectively. In other terms, the predicted non-dimensional mixing times are 4.6%, 4.6% and 0.4% higher than the experimental results at three agitation rates. Apparently, the non-dimensional mixing time increases slightly with agitation rates. This is not unexpected since the standard Apparatus 2 is an unbaffled system, with D/T=0.74, C/T=0.25, 0.5<H/T<0.3.
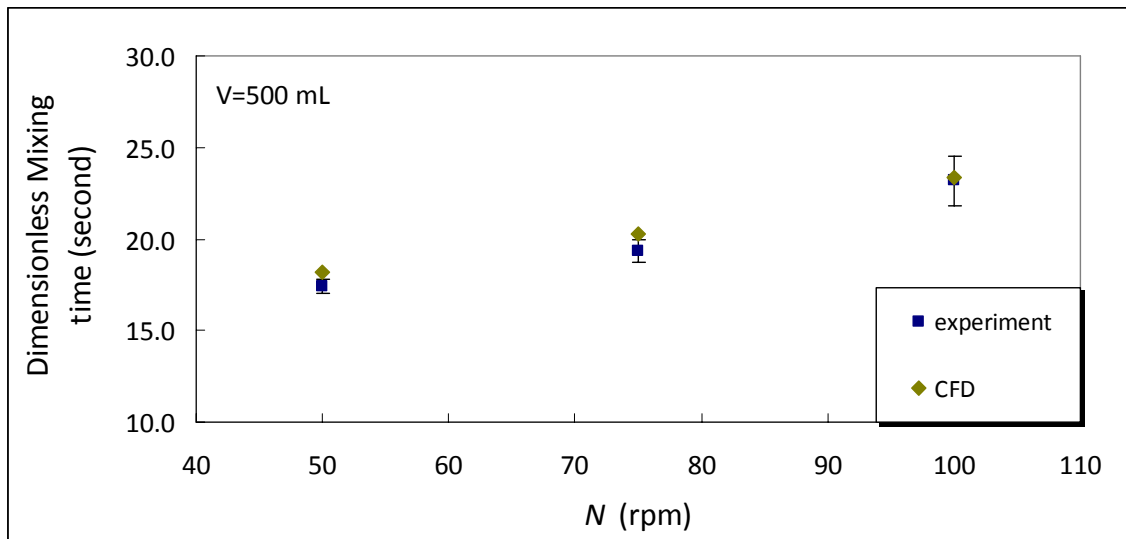
Figure 6.7 Dimensionless mixing time at agitation speeds of 50, 75 and 100 rpm in standard Apparatus 2 (500 mL solution).

In Figure 6.8, the experimental non-dimensional mixing times in the modified Apparatus 2 are shown to be 15.8, 17.9, 20.2 at 50, 75 and 100 rpm, respectively. The predicted non-dimensional mixing time are 17.0, 19.5, 22.7 seconds at 50, 75 and 100 rpm, respectively. In other terms, the predicted non-dimensional mixing times are 7.6 %, 8.9 % and 12.4 % higher than the experimental results at three agitation rates. Even in this case, the non-dimensional mixing time increases slightly with agitation rates. Although the impeller was moved off centered in the modified Apparatus 2, which resulted in an asymmetric flow pattern, the mixing performance in the modified Apparatus 2 was still not exactly the same as in a baffled mixing vessel where the non-dimensional mixing time is typically constant.
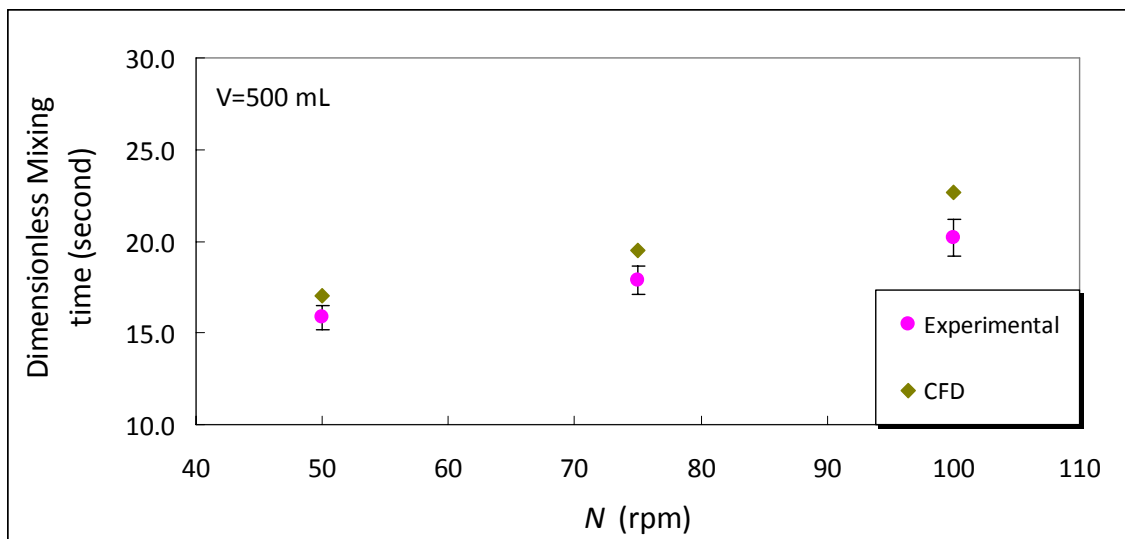
Figure 6.8 Dimensionless mixing time at agitation speeds of 50, 75 and 100 rpm in modified Apparatus 2 (500 mL solution).

6.5 Conclusions

Experiments have been undertaken in Apparatus 2 and modified Apparatus 2 to study the effect of the impeller position and agitation rates on mixing time. Discoloration method was successfully employed here to get the mixing time.

The position of impeller plays an important role on the mixing time. The mixing time in 500 mL modified Apparatus 2 is found to be much shorter than mixing time in 500 mL standard system at all agitation rates both from experiments and simulations. Compared to the results obtained from Chapter 5, increasing the power consumption is also found to reduce mixing time. The mixing time becomes shorter while increasing the agitation speed, which is expected.

The CFD models presented here correctly predicts mixing time considering the effects of impeller speed and impeller location. This shows that the transport species

method can be a valuable tools for studying the mixing time in Apparatus 2 and modified Apparatus 2.

In addition, the non-dimensional mixing time was obtained for Apparatus 2 and modified Apparatus 2 at different agitation rates. Unlike conventional baffled mixing vessel, non-dimensional mixing time increases slightly with agitation rates for both Apparatus 2 and modified Apparatus 2.

By examining mixing time, it is easier to understand that homogeneity in Apparatus 2 is achieved at a faster than in the standard USP Apparatus 2.

CHAPTER 7

CONCLUSIONS

In this study, computation and experimental work was conducted to (a) quantify the roles of some key hydrodynamic variables of importance for the standard Apparatus 2 system and determine their impact on the dissolution profiles of solid dosage forms, and (b) design and test a modified Apparatus 2 that can overcome the major limitations of the standard system, and especially those related to the sensitivity of the current apparatus to tablet location.

From the hydrodynamic point of view, the standard USP Apparatus 2 and modified Apparatus 2 have been characterized in terms of velocity distribution by Laser Doppler Velocimetry (LDV) and Particle Image Velocimetry (PIV). Two common fill levels were investigated, corresponding to volumes equal to 500 mL and 900 mL. The agitation intensities that were investigated were 50, 75 and 100 rpm, which are the prescribed agitation speed commonly encountered in the industrial practice according to USP [1].

It was found here, that in the standard system, the velocity distributions from LDV and PIV were very similar and only little affected by the liquid volume. Similar flow patterns were observed at 50, 75 and 100 rpm. The tangential velocity plays a predominant role in the whole vessel. The axial and radial velocities are significantly lower compared to the tangential velocity. However, the non-dimensional velocity profiles and the flow patterns at different impeller agitations speed were generally very similar to each other in Apparatus 2. The fluid flow in the bottom region of Apparatus 2

is highly non-uniform. Even when agitation rate is increased, the flow remains highly non-uniform, especially near the tank bottom.

Two regions were observed in the bottom zone of the vessel, i.e., a central, low-velocity inner core region, and an outer recirculation loop below the impeller, rotating around the central inner core region. This core region typically persisted, irrespective of the impeller agitation speed. Computation Fluid Dynamics (CFD) was additionally used to predict velocity profiles. Typically, the CFD predictions matched well the experimental results.

The results of this work and of previous work with the standard USP Apparatus 2 confirm that this apparatus is very sensitive to the location of the tablet, which is typically not controlled in a typical test since the tablet is dropped into the vessel at the beginning of the test and it may rest at random locations on the vessel bottom.

Therefore, in this work a modified USP Dissolution Testing Apparatus 2, in which the impeller was placed 8-mm off-center in the vessel, was designed and tested. This design eliminates the poorly mixed inner core region below the impeller observed in the standard Apparatus 2 vessel. Dissolution tests were conducted with the Modified Apparatus for different tablet locations using both disintegrating calibrator tablets (Prednisone) and non-disintegrating calibrator tablets (Salicylic Acid) tablets. The experimental data clearly showed that all dissolution profiles in the Modified Apparatus were not affected by the tablet location at the bottom of the vessel. This design can effectively eliminate artifacts generated by having the tablet settle randomly at different locations on the vessel bottom after dropping it at the beginning of a dissolution testing experiment.

The fluid velocity profiles inside modified the Apparatus 2 were obtained via LDV at three impeller agitations speeds as well, namely 50 rpm, 75rpm and 100 rpm. Experimental measurements in the modified Apparatus 2 showed that the velocity profiles and flow pattern are significantly altered by the presence of the impeller in an offset position. Tangential velocities are still the stronger components of the velocity at any location even in modified Apparatus 2. However, axial and radial velocities are significantly higher than in the standard Apparatus 2. In addition, the velocity profiles near the bottom of the vessel were found to be significantly more uniform than in the standard Apparatus 2, because of the elimination of the poorly mixed zone below the impeller.

The fluid velocity profiles were also computationally obtained via Computational Fluid Dynamics (CFD) at three impeller agitations speeds in both systems. The predictions obtained with CFD where the k-ε model was used to account for turbulence effects were validated with the experimental results. In general, good agreement was found between the experimental velocity measurements and CFD predictions.

The power dissipated by the impeller in the standard Apparatus 2 and the modified Apparatus 2 was experimentally measured using a frictionless system coupled with torque measurement. CFD was additionally used to predict the power consumption, using two different approaches, one based on the integration of the local value of the energy dissipation rate, and the other based on the prediction of the pressure distribution on the impeller blade, from which the torque and the power required to rotate the impeller were predicted. The agreement between the experimental data and both types of numerical predictions was found to be quite satisfactory in most cases. The results were

expressed in terms of the non-dimensional Power number, Po, which was typically found to be on the order of ~0.3. The power number was observed to decrease very gradually with increasing agitation speeds.   In general, the power dissipated in the modified Apparatus 2 was higher than in the standard system, as expected.

Finally, the mixing time in the modified system, as experimentally measured by using a decolorization method and computationally predicted through CFD simulation, was found to be shorter in the modified Apparatus 2 by 7.7 %-12.9 % as compared to Apparatus 2. The CFD model correctly predicted mixing time considering the effects of impeller speed and impeller location. This shows that the transport species method used to generate mixing time results can be a valuable tool for studying the mixing time in Apparatus 2 and modified Apparatus 2. From the determination of the mixing time, it is easier to understand that achieving liquid homogeneity in Apparatus 2 is a much faster process than tablet dissolution. In addition, non-dimensional mixing time was obtained in Apparatus 2 and in modified Apparatus 2 at different agitation rates and was found to be relatively constant.

It can be concluded that the modified Apparatus 2 is a more robust testing apparatus, which is capable of producing dissolution profiles that are less sensitive to small geometric factors that play a major role in the standard USP Apparatus 2.

APPENDIX A

VELOCITY DISTRIBUTIONS BY PARTICLE IMAGE VELOCIMETRY

Figures A.1 to A.3 show the tangential, axial and radial velocity distributions in standard Apparatus 2 (900 mL water) from PIV, respectively. Figures A.4 to A.6 show the tangential, axial and radial velocity distributions in standard Apparatus 2 (500 mL water) from PIV, respectively.
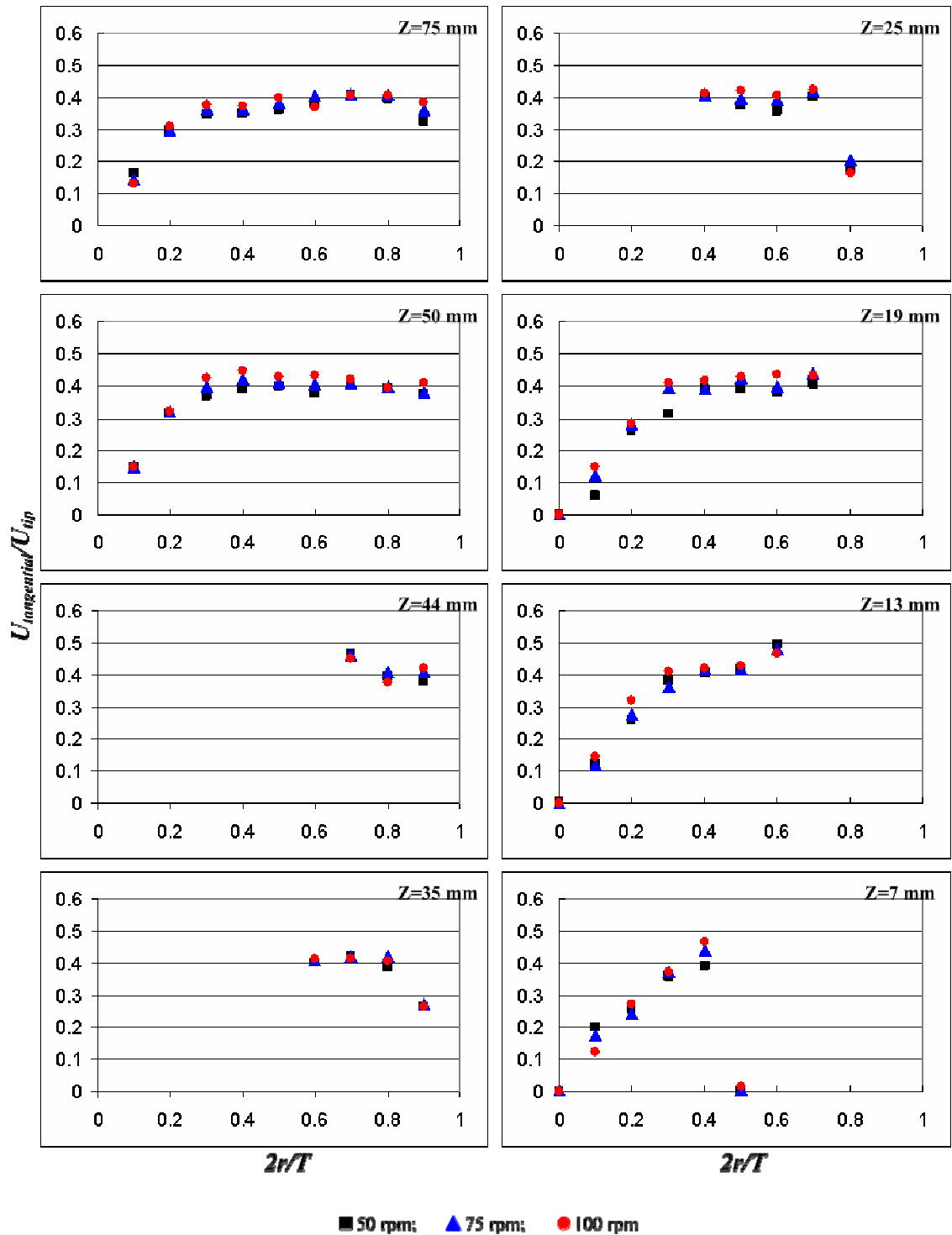
Figure A.1 PIV measurements for tangential velocities on eight iso-surfaces at different agitation speeds in standard Apparatus 2 (900 mL water).
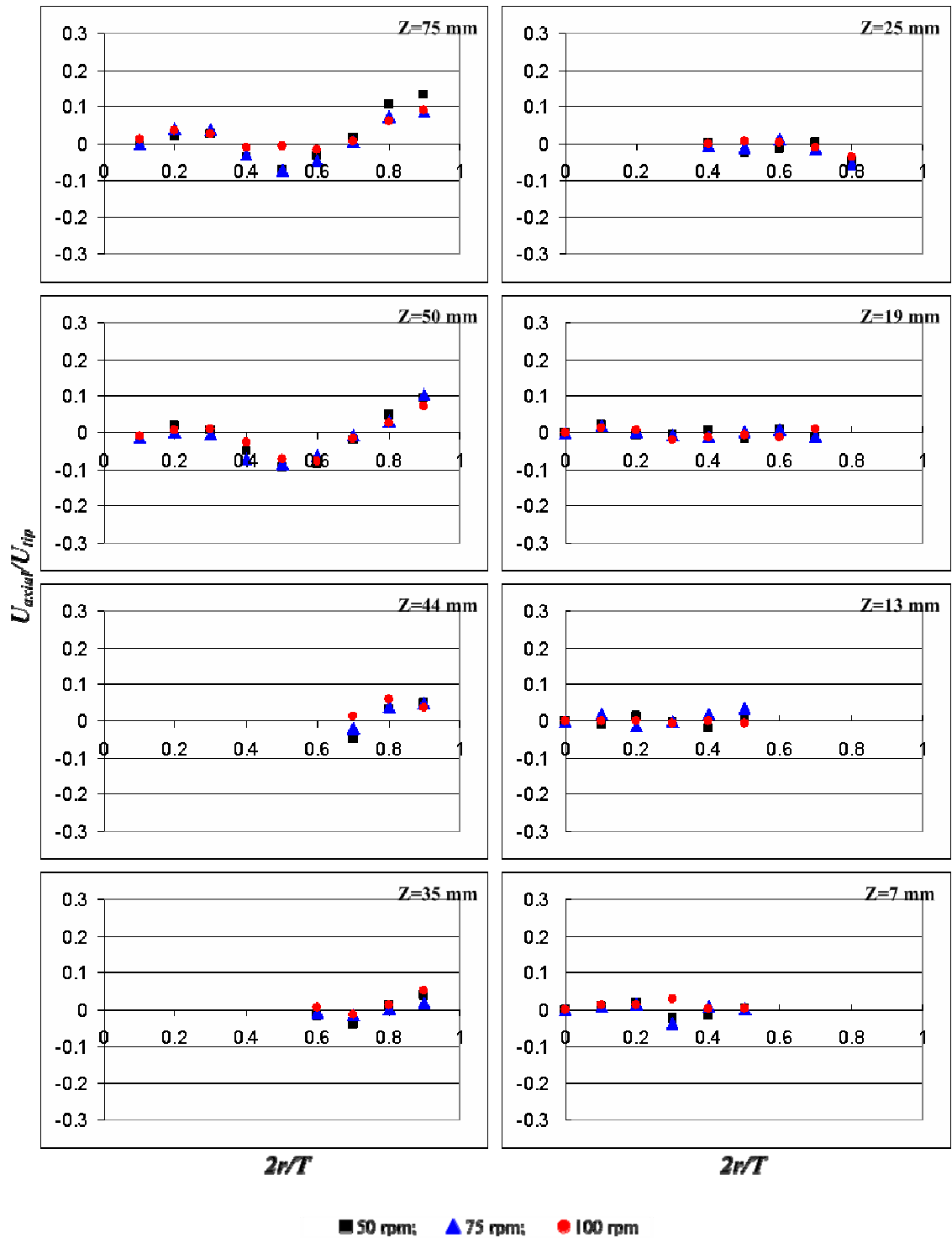
Figure A.2 PIV measurements for axial velocities on eight iso-surfaces at different agitation speeds in standard Apparatus 2 (900 mL water).
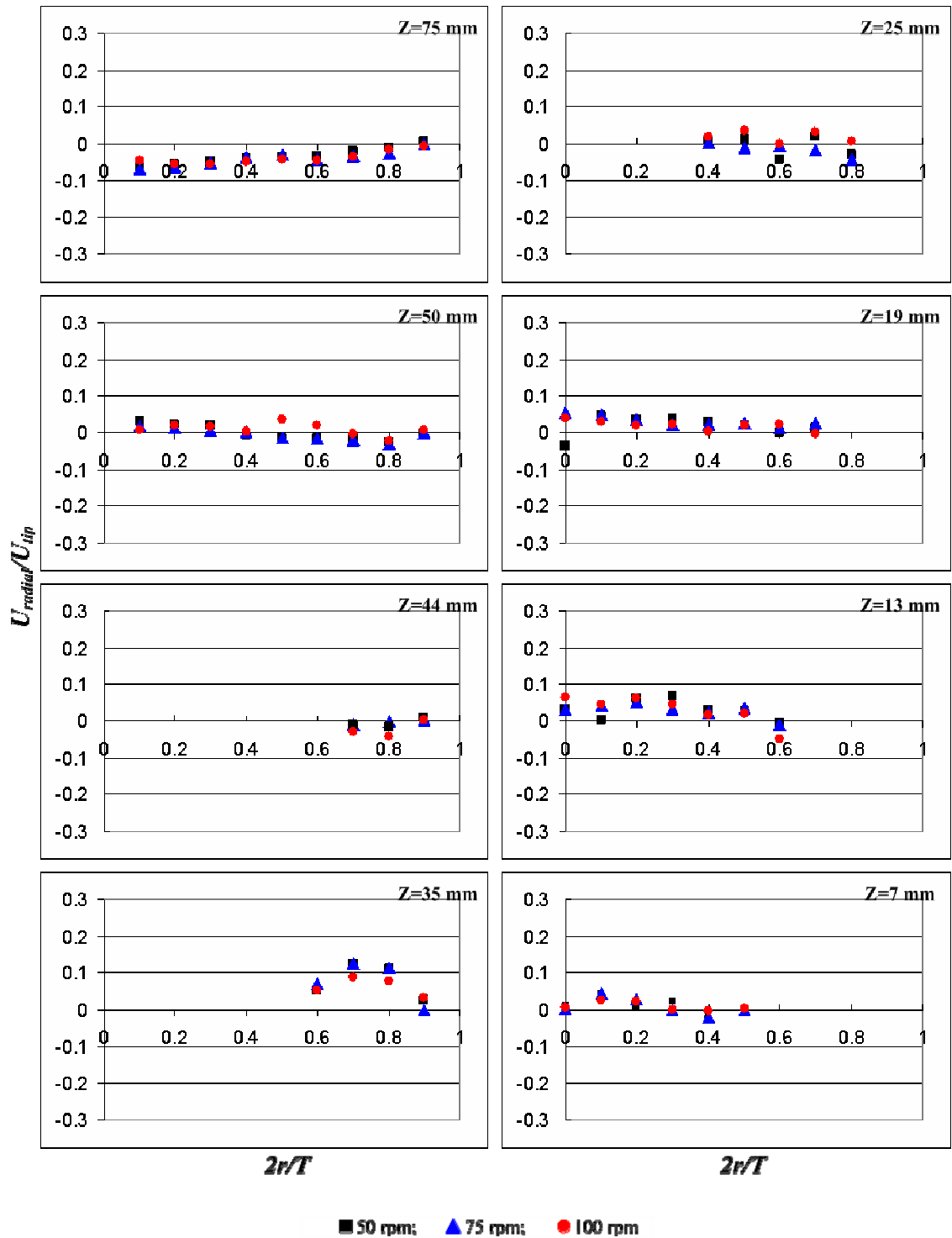
Figure A.3 PIV measurements for radial velocities on eight iso-surfaces at different agitation speeds in standard Apparatus 2 (900 mL water).

Figure A.4 PIV measurements for tangential velocities on eight iso-surfaces at different agitation speeds in standard Apparatus 2 (500 mL water).
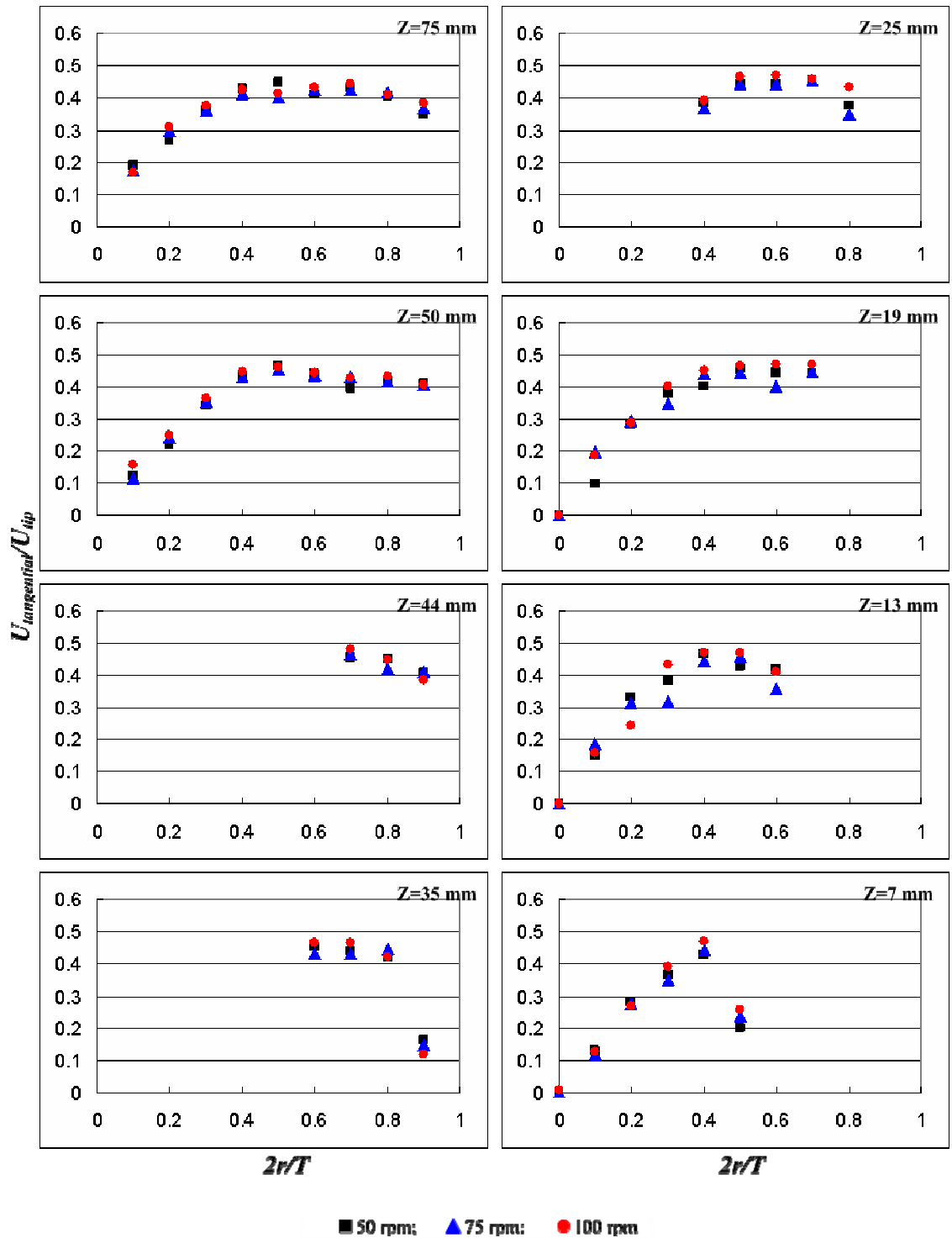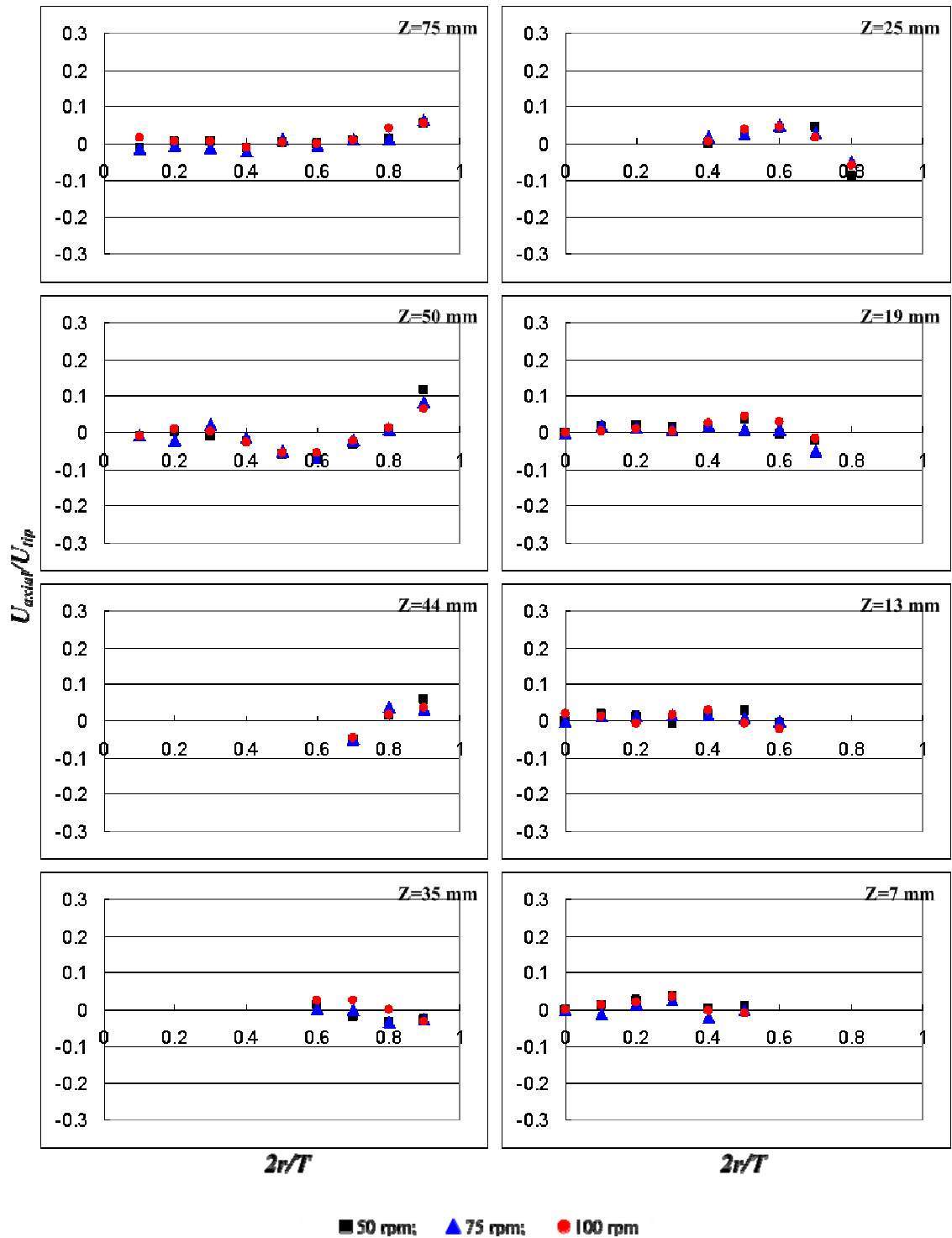
Figure A.5 PIV measurements for axial velocities on eight iso-surfaces at different agitation speeds in standard Apparatus 2 (500 mL water).
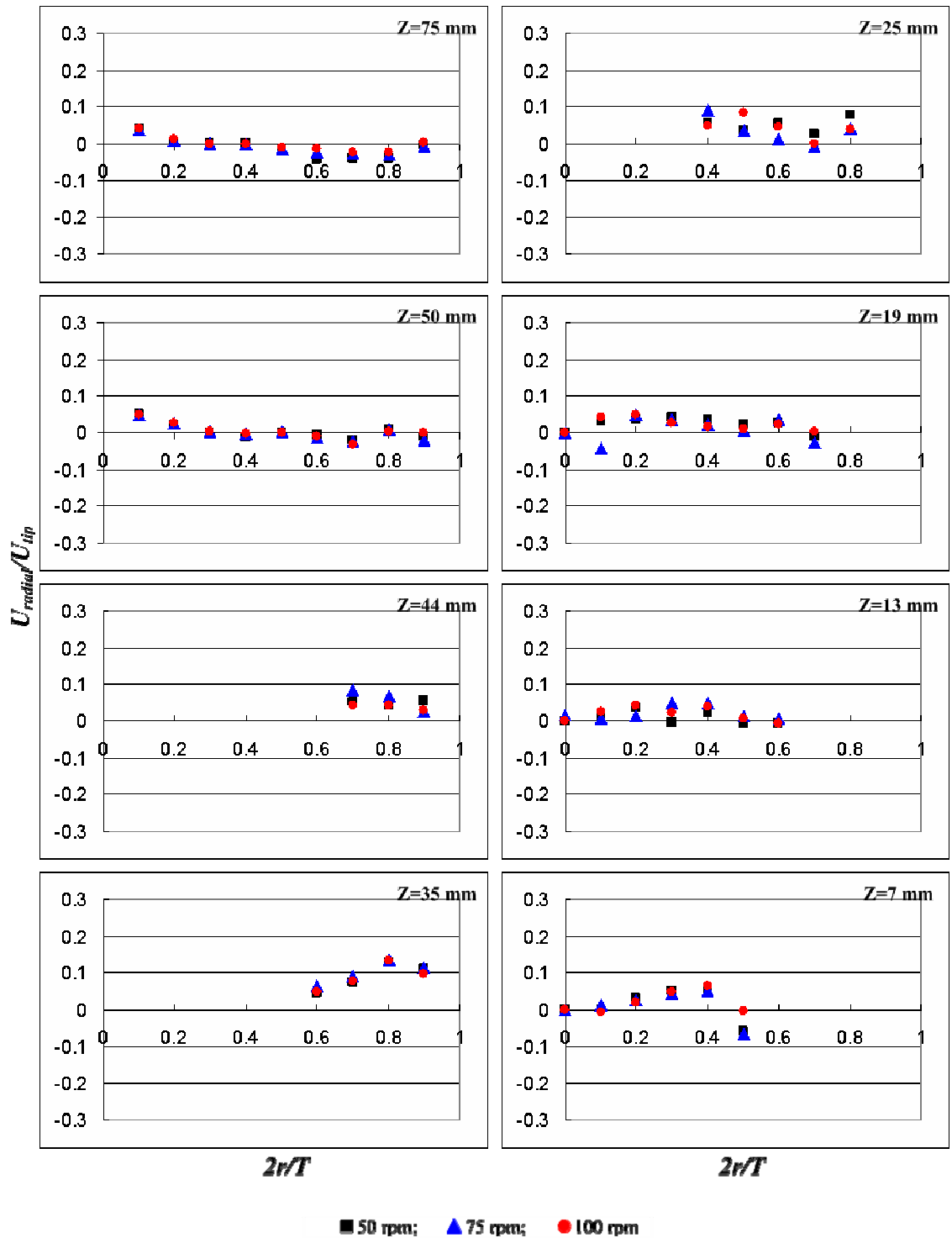
Figure A.6 PIV measurements for radial velocities on eight iso-surfaces at different agitation speeds in standard Apparatus 2 (500 mL water).

Figures B.1 and B.2 show the solid suspension diagrams in standard Apparatus 2 and modified Apparatus 2 at an agitation speed of 50 rpm (900 mL water), respectively.
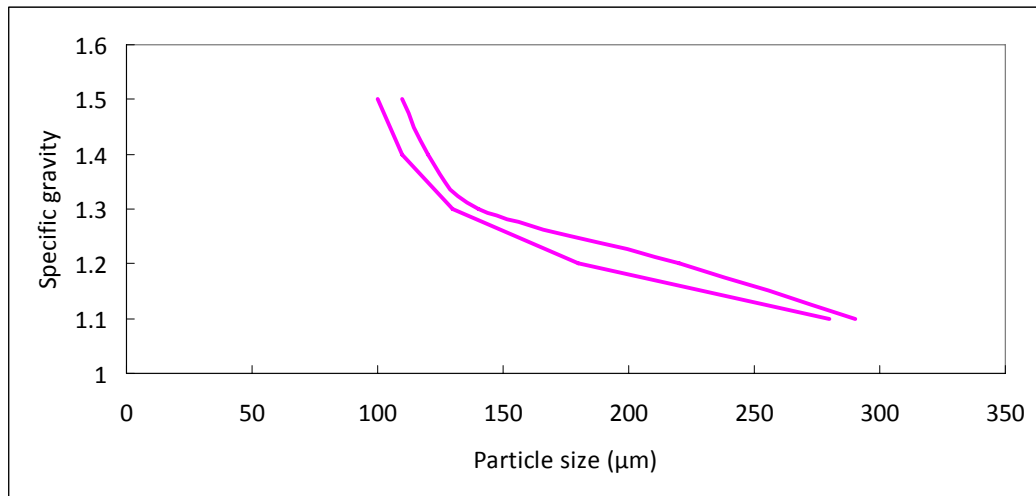
Figure B.1 Solid suspension diagram in standard Apparatus 2 at an agitation speed of 50 rpm (900 mL water).
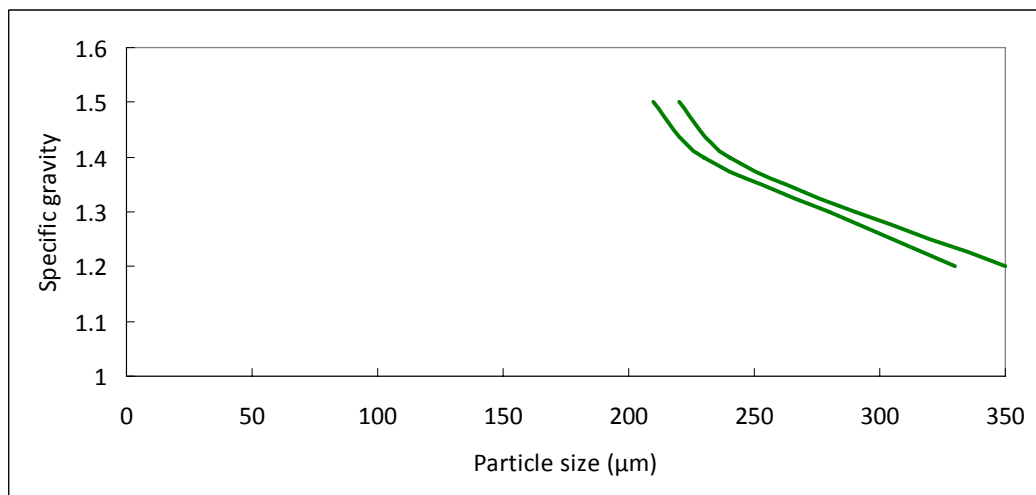
Figure B.2 Solid suspension diagram in modified Apparatus 2 at an agitation speed of 50 rpm (900 mL water).

REFERENCES

[1] United States Pharmacopeia & National Formulary. The official compendia of standards, USP 31/NF 26, (2008). Pharmacopeia Convention, Inc.

[2] FDA, (1997). Guidance for Industry: Dissolution testing of immediate release solid oral dosage forms.

[3] Gray, V., Kelly, G., Xia, M., Butler, C., Thomas, S., Mayock, S. (2009). The science of USP 1 and 2 dissolution: Present challenges and future relevance. *Pharmaceutical Research*, 26(6):1289-1302.

[4] Bai, G., Armenante, P. M. (2008). Velocity distribution and shear rate variability resulting from changes in the impeller location in the USP dissolution testing apparatus II. *Pharmaceutical Research*, 25(2): 320-336.

[5] Bai, G., Armenante, P. M. (2009). Hydrodynamic, mass transfer and dissolution effects induced by tablet location during dissolution testing. *Journal of Pharmaceutical Sciences*, 98(4): 1511-1531.

[6] Gao, Z., Moore, T. W., Doub, W. H., Westenberger, B. J., Bushe, L. F., (2006). Effect of deaeration methods on dissolution test in aqueous media: a study using a total dissolved gas pressure meter. *Journal of Pharmaceutical Sciences*. 95(7): 1606-1613.

[7] Gao, Z., Moore, T. W., Doub, W. H., (2008). Vibration effects on dissolution test with USP apparatus 1 and 2. *Journal of Pharmaceutical Sciences*, 97(8): 3335-3343.

[8] Cox, D. C., Furman, W. B. (1982). Systematic error associated with apparatus 2 of the USP dissolution test I: Effects of physical alignment of the dissolution apparatus. *Journal of pharmacutical Sciences*, 71(4): 451-452.

[9] Moore T. W., Hamilton, J. F., Kerner, C. M. (1995). Dissolution testing: Limitations of the USP prednisone and salicylic acid calibrator tablets. *Pharmacopeial Forum*, 21(5): 1387-1396.

[10] Qureshi, S.A., Shabnam, J. (2001). Cause of high variability in drug dissolution testing and its impact on setting tolerances. *European Journal of Pharmaceutical Science*, 12(3): 271-276.

[11] Mauger, J., Ballard, J., Brockson, R., De, S., Gray, V., Robinson, D. (2003). Intrinsic dissolution performance of USP dissolution apparatus 2 (rotating paddle) using modified salicylic acid calibrator tablets: Proof of principle. *Dissolution Technologies*, 10: 6-15.

[12] Qureshi, S. A., McGilveray, I. J. (1999). Typical variability in drug dissolution testing: Study with USP and FDA calibrator tablets and a marketed drug

(glibenclamide) product. *European Journal of Pharmaceutical Sciences*, 7(3): 249-258.

[13] Costa, P., Lobo, J. M. S. (2001). Influence of dissolution medium agitation on release profiles of sustained-release tablets. *Drug Development and Industrial Pharmacy*, 27(8): 811-817.

[14] Bocanegra, L. M., Morris, G. J., Jurewicz, J. T., Mauger, J. W. (1990). Fluid and particle laser doppler velocity measurements and mass transfer predictions for the USP paddle method dissolution apparatus. *Drug Development and Industrial Pharmacy*, 16(9): 1441-1464.

[15] Cox, D. C., Furman, W. B., Thornton, L. K., Moore, T. W., Jefferson, E. H. (1983). Systematic error associated with apparatus 2 of the USP dissolution test III: Limitation of calibrators and the USP suitability test. *Journal of Pharmaceutical Sciences*, 72(8): 910-913.

[16] Gray V. (2006). Challenges to the dissolution test, including equipment calibration. *Dissolution Technologies*, 16(4):6-9.

[17] Bai, G., Armenante, P. M., Plank, R. V. (2007). Experimental and computational determination of blend time in USP dissolution testing apparatus II, *Journal of Pharmaceutical Sciences*, 96(11): 3072-3086.

[18] Bai, G., Armenante, P. M., Plank, R. V., Gentzler, M., Ford, K., Harmon, P. (2007). Hydrodynamic investigation of USP dissolution test apparatus II. *Journal of Pharmaceutical Sciences*, 96(9): 2327-2349.

[19] FDC Reports, (2001). Recalls prompted by FDA on the increase. *The gold sheet*. 35, 1.

[20] FDC Reports, (2002). Counterfeits pose special recall challenge. *The gold sheet*. 36, 1.

[21] FDC Reports, (2003). Spike in potency-related problems contributes to overall rise in 2002 recalls. *The gold sheet*. 37, 1.

[22] FDA Enforcement Reports, (2009). Food and Drug Administration, Department of Health and Human Services.

[23] Cohen, J. L., Hubert, B. B., Leeson, L. J., Rhodes, C. T., Robinson, J. R., Roseman, T. J., Shefter, E. (1990). The development of USP dissolution and drug release standards. *Pharmaceutical Research*, 7(10): 983-987.

[24] Kukura, J., Arratia, P. E., Szalai, E. S., Muzzio, F. J., (2003). Engineering tools for understanding hydrodynamics of dissolution tests. *Drug Development and Industrial Pharmacy*, 29(2): 231-239.

[25] Baxter, J. L., Kukura, J., Muzzio, F. J., (2005). Hydrodynamics-induced variability

in the USP apparatus 2 dissolution test. *International Journal of Pharmaceutics*, 292(1-2): 17-28.

[26] McCarthy, L. G., Kosiol, C., Healy, A. M., Bradley, G., Sexton, J. V., Corrigan, O. I., (2003). Simulating the hydrodynamic conditions in the United States Pharmacopeia paddle dissolution apparatus. *AAPS Pharmscitech*, 4(2): 83-98.

[27] Kukura, J., Baxter, J. L., Muzzio, F. J., (2004). Shear sistribution and variability in the USP apparatus 2 under turbulent conditions. *International Journal of Pharmaceutics*, 279(1-2): 9–17.

[28] McCarthy, L. G., Bradley, G., Sexton, J. C., Corrigan, O. I., Healy, A. M. (2004). Computational fluid dynamics modeling of the paddle dissolution apparatus: Agitation rate mixing patterns, and fluid velocities. *AAPS Pharmscitech*, 5(2): 50-59.

[29] Ross, M.S.F., Rasis, M. (1998). Mega paddle: A recommendation to modify apparatus 2 used in the USP general test for dissolution (711). *Pharmacopeial Forum*, 24(3): 6351–6353.

[30] Qureshi, S. A., Shabnam, J. (2003). Applications of a new device (spindle) for improved characterization of drug release (dissolution) of pharmaceutical products. *European Journal of Pharmaceutical Sciences*, 19(4): 291-297.

[31] Shah, V. P., Gurbarg, M., Noory, A., Dighe, S., Skelly, J. P. (1992). Influence of higher rates of agitation on release patterns of immediate-release drug products. *Journal of Pharmaceutical Sciences*, 81(6): 500-503.

[32] Gibaldi, M., Feldman, S. (1967). Establishment of sink conditions in dissolution rate determinations. Theoretical considerations and application to nondisintegrating dosage forms. *Journal of Pharmaceutical Sciences*, 56(10): 1238–1242.

[33] Kamba, M., Seta, Y., Takeda, N., Hamaura, T., Kusai, A., Nakane, H., Nishimura, K. (2003). Measurement of agitation force in dissolution test and mechanical destructive force in disintegration test. *International Journal of Pharmaceutics*, 250(1): 99-109.

[34] Particle Image Velocimetry software version 3.3 instruction manual, (2000). TSI Inc.

[35] Qureshi, S., (2009). Drug dissolution testing: Selecting a dissolution medium for solid oral products. *American Pharmaceutical Review*. 12(1): 18, 20, 22-23.

[36] Hamlin, W. E., Nelson, E., Ballard, B. E., Wagner, J. G., (1962). Loss of sensitivity in distinguishing real differences in dissolution rates due to increasing agitation intensity. *Journal of Pharmaceutical Sciences*, 51(5): 432-435.

[37] Qureshi, S. A., (2004). Choice of rotation speed (rpm) for bio-relevant drug dissolution testing using a crescent-shaped spindle. *European Journal of*

Pharmaceutical Sciences, 23(3): 271-275.

[38] Baxter, J. L., Kukura, J. Muzzio, F. J., (2006). Shear-induced variability in the USP apparatus 2: modifications to the existing system. *AAPS Journal*, 7(4): 857-864.

[39] Peeters, K., Maesschalck, R. D., Bohets, H., Vanhoutte, K., Nagels, L., (2008). In situ dissolution testing using potentiometric sensors. *European Journal of Pharmaceutical Sciences*, 34(4-5): 243-249.

[40] Moore, J. W., Flanner, H. H. (1996). Mathematical comparison of dissolution profiles. *Pharmaceutical Technology*, 20(6): 64-74.

[41]GAMIT 2.4.6 Users' Guide, (2006). FLUENT, Inc., New Hampshire.

[42]FLUENT6.3.26 Users' Guide, (2006). FLUENT, Inc., New Hampshire.

[43] Armenante, P. M., Chang, G. M., (1998). Power consumption in agitated vessels provided with multiple-disk turbines. *Ind. Eng. Chem. Res*. 37, 284-291.

[44] Armenante, P. M., Mazzarotta, B., Chang, G. M., (1999). Power consumption in stirred tanks provided with multiple pitched-blade turbines. *Ind. Eng. Chem. Res*. 38, 2809-2816.

[45] Rushton, J. H., Costich, E. W., Everett, H. J. (1950). Power characteristics of mixing impellers. *Chemical Engineering Progress*. (Part I) 46: 395-402; (Part II) 46: 467-476.

[46] Bates, R. L., Fondy, P. L., Corpstein, R. R. (1963). Examination of some geometric parameters of impeller power. *Industrial and Engineering Chemistry Process Design and Development*. 2(4): 310-314.

[47] Chudacek, M. W. (1985). Impeller power numbers and impeller flow numbers in profiled bottom tanks. *Industrial and Engineering Chemistry Process Design and Development.* 24(3): 858-867.

[48] Gray, D. J., Treybal, R. E., Barnett, S. M. (1982). Mixing of single and two phase systems: Power consumption of impellers. *AIChE Journal*, 28(2): 195-199.

[49] Shiue, S. J. and Wong, C. W. (1984). Studies on homogenization efficiency of various agitators in liquid blending. The *Canadian Journal of Chemical Engineering*, 62(5): 602-609.

[50] Papastefanos, N., Stamatoudis, M. (1989). Effect of impeller and vessel size on impeller power number in closed vessels for Reynolds numbers between 40 and 65000. *Chemical Engineering Communications*, 80, 69-79.

[51] Rewatkar, V. B., Raghava Rao, K. S. M. S., Joshi, J. B. (1990). Power consumption in mechanically agitated contactors using pitched bladed turbine impeller. *Chemical Engineering Communications*, 88, 69-90.

[52] White, A. M., Brenner, E., Phillips, G. A., Morrison, M. S. (1934). Studies in

agitation. IV: Power measurements. *AIChE.*, New York meeting. 15.

[53] Bates, R. L., Fondy, P. L., Fenic, J. C. (1966). Impeller characteristics and power. *Academic Press: New York*. Vol. I: 111-178.

[54] White, A. M., Brenner, E. (1934). Studies in agitation. V: The correlation of power data. *AIChE.*, New York meeting. 12.

[55] O'Connell, F. P., Mack, D. E. Simple turbines in fully baffled tanks. (1950). *Chemical Engineering Progress*, 46, 358-362.

[56] Armenante, P. M., Chou, C. (1996). Velocity profiles in a baffled vessel with single or double pitched-blade turbines. *AIChE Journal*, 42(1): 42-54.

[57] Kresta, S. M., Wood, P. E. (1991). Prediction of the three-dimensional turbulent flow in stirred tanks. *AIChE Journal*, 37(3), 448-460.

[58] Kresta, S. M., Wood, P. E. (1993). The flow field produced by a pitched blade turbine: Characterization of the turbulence and estimation of the dissipation rate. *Chemical Engineering Science*, 48(10): 1761-1774.

[59] Ranade, V. V., Joshi, J. B. (1990). Flow generated by a disc turbine. Part II: Mathematical modeling and comparison with experimental data. *Chemical Engineering Research and Design*, 68: 34-50.

[60] Armenante, P. M., Chou, C. (1994). Experimental LDV measurement and numerical CFD determination of the fluid velocity distribution in an unbaffled mixing vessel. *AIChE Symposium Series*, 299: 33-40.

[61] Ciofalo, M., Brucato, A., Grisafi, F., Torraca, N. (1996). Turbulent flow in closed and free-surface unbaffled tanks stirred by radial impellers. *Chemical Engineering Science*, 51(14), 3557-3573.

[62] Markopoulos, J., Kontogeorgaki, E. (1995). Vortex depth in unbaffled single and multiple impeller agitated vessels. *Chemical Engineering and Technology*, 18(1): 68-74.

[63] Hixon, A. W., Crowell, J. H., (1931). Dependence of reaction velocity upon surface and agitation. Part III. Experimental procedure in study of agitation. *Ind. Eng. Chem.* 23, 1160-1169.

[64] Mack, D. J., Marriner, R. A., (1949). A method of correlating agitator performance. *Chem. Eng. Prog.* 45, 545-552.

[65] Armenante, P. M., Kirwan, D. J., (1989). Mass transfer to microparticles in agitated systems. *Chemical Engineering Science.* 44(12): 2781-2796.

[66] Bai, G., Wang, Y., Armenante, P. M., (2010). Velocity distribution and shear rate variability resulting from changes in the agitation speed in the USP apparatus II. *International Journal of Pharmaceutical Science*, 403 (1-2): 1-14.

[67] Madhu, G. M., Girish, A. J., Ganesh, P. R., Agarwal, S. S., Kacker, R., Akshaya S., K., (2009). Energy efficiency and mixing time calculations in mechanically agitated liquid liquid contactors. *Asian J. Exp. Sci.*, 23 (1): 157-164.

[68] Cabaret, F., Bonnot, S., Fradette, L., Tanguy, P., (2007). Mixing time analysis using colorimetric methods and image processing. *Ind. Eng. Chem. Res.*, 46: 5032-5042.

[69] Delaplace, G., Bouvier, L., Moreau, A., Guerin, R., Leuliet, J-C, (2004). Determination of mixing time by colourimetric diagnosis—application to a new mixing system. *Experiments in Fluids*, 36 (3): 437-443.

[70] Reilly, C. D., Britter, R. E., (1985). Mixing times for passive tracers in stirred tanks. *5th European Conference on Mixing*, 10-12, Wurzburg, West Germany.

[71] Ruszkowski, S. M., Muskett, M. J., (1985). Comparative mixing times for stirred tank agitators. *5th European Conference on Mixing*, Wurzburg, 10–12, BHRA: 89–104.

[72] Jaworski, Z., Bujalski, W., Otomo, N., Nienow, A. W., (2000). CFD study of homogenization with dual Rushton turbines—comparison with experimental results. Part I: Initial studies. *Chemical Engineering Research and Design* 78: 327–333.

[73] Guillard, F., Tragardh, C., (2003). Mixing in industrial Rushton turbine-agitated reactors under aerated conditions. *Chemical Engineering and Processing.* 42(5): 373-386.

[74] Kramers, H., Baars, G. M., Knoll, W. H., (1953). A comparative study on the rate of mixing in stirred tanks. *Chem. Eng. Sci.*, 2(1):35-42.

[75] Dickey, D. S., (2009). Minimize Blending Time. (http://www.chemicalprocessing.com/articles/2009/120.html)

[76] Gogate, P. R., Pandit, A. B., (1999). Mixing of miscible liquids with density differences: effect of volume and density of the tracer fluid. *The Canadian Journal of Chemical Engineering*, 77(5): 988-996.

[77] Osman, J. J., Varley, J., (1999). The use of computational Fluid Dynamics (CFD) to estimate mixing times in a stirred tank. *IChemE Symposium Series*. 146, 15–22.

[78] Bujalski, W., Jaworski, Z., Nienow, A. W., (2002). CFD study of homogenization with dual Rushton turbines—comparison with experimental results. *Chemical Engineering Research and Design.* 80, 97–104.

[79] Shekhar, A. M., Jayanti, S., (2002). CFD study of power and mixing time for paddle mixing in unbaffled vessels. *Chemical Engineering Research and Design*. 80, 482–498.

[80] Jaworski, Z., Dudczak, J., (1998). CFD modelling of turbulent macromixing in

stirred tanks. *Computers and Chemical Engineering*. 22, 293–298.

[81] Grenville, R. K., Nienow, A. W., (2004). Blending of miscible liquids. In: Paul, P. L., Atiemo-Obeng, V. A., Kresta, S. M.. *Handbook of Industrial Mixing*. Wiley, NJ, 513.